AN INVESTIGATION OF THE ROLE OF THERMAL CONDITIONS, HYDROLOGIC PROCESSES, AND COUNTRY-ROCK PERMEABILITY IN MAAR ERUPTIONS

By Emily S. Anderson

A Thesis

Submitted in Partial Fulfillment

of the Requirements for the Degree of

Master of Science

in Geology

Northern Arizona University

December 2017

Approved:

Michael Ort, Ph.D., Chair

Curtis M. Oldenburg, Ph.D.

Nancy Riggs, Ph.D.

ABSTRACT

AN INVESTIGATION OF THE ROLE OF THERMAL CONDITIONS, HYDROLOGIC PROCESSES, AND COUNTRY-ROCK PERMEABILITY IN MAAR ERUPTIONS

EMILY S. ANDERSON

The interaction of magma and groundwater often results in explosive eruptions due to processes of molten fuel-coolant interaction (MFCI). Explosivity of these eruptions is largely controlled by the extent of mixing between water (coolant) and magma (fuel) and the location in the conduit where interaction occurs. Recently published experiments and calculations show that most phreatomagmatic tuff-ring deposits are probably produced by explosions occurring above ~200 m depth, while those below this depth are rarely energetic enough to displace material at the ground surface. It is thus uncertain how phreatomagmatic eruptions occur where depth to the water table is far below this critical depth of 200 m, as it is in some semi-arid and arid environments. Even in locations where groundwater is above this depth, explosions using up available water can result in progressive drawdown of the water table, producing a cone of groundwater depression within the diatreme. In these cases, the question arises as to how explosions continue if the water source "dries up." The idea of explosive transport, or water being thrown upward from explosions beneath the water table, has been described as one possible mechanism for providing shallow water for continued explosions; however, this process would not likely move the large quantities of water needed to sustain long-term phreatomagmatism. Few studies have focused on questions regarding the details of thermohydrologic processes that control these eruptions. To address this problem, I have investigated two maars, Colton Crater and Rattlesnake Crater, in the San Francisco Volcanic Field of northern Arizona. Hydrologic, structural, and stratigraphic data of the subsurface

beneath each volcano have been used to construct conceptual models of groundwater flow and heat transfer within each eruptive system, and relevant thermophysical flow processes have been modeled using the TOUGH2 simulator.

Colton Crater was formed by a prolonged, dry cinder-cone-building eruption with only a brief late period of intense phreatomagmatic activity, while Rattlesnake Crater's deposits display characteristics of sustained magma-water interaction and an eventual drying-out. The continued phreatomagmatic explosions at Rattlesnake Crater may have resulted from large-scale vapor transport, driven by magmatic heat, through permeable country rock and vertical fractures prior to and during eruption. Water (from condensed vapor) held at a shallow depth could then interact with quickly ascending magma, producing explosions. These processes do not appear to have occurred to the same extent at Colton Crater, as the eruption only experienced a brief period of phreatomagmatism. Models indicate that some vapor transport and condensation could have occurred outside the conduit during the eruption, producing a small amount of available water for MFCI, but explosions could have also been driven by a limited volume of perched water present in the shallow limestone unit prior to eruption. Results of this study aim to provide an example of a modeling approach for quantitative analysis of complex non-isothermal two-phase systems undergoing vaporization and condensation driven by magma intrusion, which can potentially be used for hazard assessment and monitoring for future eruptions in active volcanic regions.

ACKNOWLEDGEMENTS

I would first like to thank my advisor Dr. Michael Ort of the School of Earth Sciences and Environmental Sustainability (SESES) at Northern Arizona University for his unending help and support in completing this research. Michael has always provided me with encouragement and guidance when I needed it, and his enthusiasm for this project and my success has been a great motivation. I will forever be grateful for his assistance in my completion of this thesis.

I would also like to thank my committee members, Dr. Curtis Oldenburg of Lawrence Berkeley National Laboratory and Dr. Nancy Riggs of SESES at NAU. Curt's assistance and patience as I worked to learn TOUGH2 was invaluable. He fielded many emails full of questions throughout this past year, and I can't imagine where I'd be without his help. Nancy's constructive comments and perspective in this project have been so appreciated. Her wisdom and endless encouragement has kept me positive many times throughout my time at NAU, and for that I am forever grateful.

Finally, I would like to express my sincere gratitude to my parents for always supporting my academic goals and encouraging me every step of the way, even when it takes me across the country. I also want to thank my fiancé, Jason, for his amazing support and for always trying to keep me positive through many weeks of stress. Without these people, this achievement would not have been possible. Thank you so much.

Emily Anderson

TABLE OF CONTENTS

LIST OF TABLES
(In text)

LIST OF FIGURES

CHAPTER 1: INTRODUCTION

1.1. Background

Phreatomagmatic eruptions occur when magma interacts directly with liquid groundwater or surface water, resulting in rapid conversion of thermal energy to mechanical energy in processes often referred to as molten fuel-coolant interaction (MFCI). The efficiency of MFCI processes is affected by properties of the magma and water, as well as by external factors including contact surface geometry and system conditions (pressure, temperature, etc.). Magma-water interaction can therefore result in a range of activity, from passive thermal granulation to violent thermohydraulic explosions. Current understanding of these processes is largely based on numerous experimental studies that have been carried out since the 1970s, and observation of phreatomagmatic eruptions and their deposits (White, 1996; Zimanowski et al., 2015). Insight is also provided via theoretical studies, such as White's (1996) discussion of the impact of an "impure" coolant, or sediment-laden water, on MFCI efficiency.

Maar-diatreme eruptions are characterized by repetitive phreatomagmatic explosions that may vary in magnitude and severity. Maars are typically monogenetic, but their eruptions pose significant volcanic hazards, as they have the potential to be highly explosive and destructive to human life and civilizations (White and Ross, 2011; Blaikie et al., 2014). Maar-diatremes can form suddenly and in a wide range of subsurface environments, from soft-sediment substrate (e.g., Tecuitlapa, Mexico, Ort and Carrasco-Núñez (2009); Hopi Buttes, AZ, Hooten and Ort (2002)) to hard, fractured country rock (e.g., West Eifel volcanic field, Germany and Massif Central, France, Lorenz (2003)). These volcanoes are increasingly well-studied in terms of

structure and deposits, but questions remain regarding thermohydrologic processes that control their eruptive behavior.

The explosive magma-water interactions that form maars may excavate country rock to produce diatremes extending as deep as ~2.0-2.5 km (Valentine and White, 2012; Blaikie et al., 2014). The maar is seen at the surface as a broad crater lying below the pre-eruptive surface that is generally enclosed by a tephra ring < 30 m in height (de Silva and Lindsay, 2015), while diatremes are the volcanic-debris-filled conduits beneath maars, formed as explosions brecciate wall rock and recycle material throughout the eruption (Fig. 1). Diatremes are typically filled with a poorly sorted mixture of lithic and juvenile material, often overlain by bedded tuff and lapilli deposits that have slumped into the upper diatreme. This slumping of material around the crater rim contributes to the production of a roughly cone-shaped diatreme. Lower pressure at shallow depths also results in more efficient MFCI and decreased rock strength, which allows shallow explosions to break up larger areas of surrounding country rock than deeper explosions (White and Ross, 2011; Valentine and White, 2012).

Maars display repetitive dilute pyroclastic density current and fall deposits, which suggests their eruptions are driven by recurring explosions (Ort and Carrasco-Núñez, 2009; Valentine and White, 2012). The repetitive occurrence of these explosions and their variable intensity may be affected by several factors, including diatreme collapse, a fluctuating water supply, and vent migration. Unstable walls or debris piles often collapse into the vent, which can trigger explosions or cut off the water supply (Lorenz, 1986; Morrissey et al., 2000). The amount of water interacting with magma may also fluctuate throughout an eruption due to gradual drawdown of the water table or movement of the explosion locus through different layers of country rock (Lorenz, 1986). Maar deposits often show a progressive “drying-out” sequence,

suggesting the water source becomes exhausted, while in other cases, magma may interact with increasing amounts of water if the vent or explosion locus moves into a confined aquifer or saturated unit (Ort and Carrasco-Núñez, 2009; Valentine and White, 2012).

Country-rock structure, material, and permeability can also strongly influence eruptive behavior, as these factors determine hydraulic flow rate, "impurity" or amount of sediment in the water, and pressure conditions. Structural features in the subsurface such as faults and joints may serve to increase or possibly hinder groundwater movement. In general, fractures produced by tensional stress have larger apertures and promote groundwater flow, while compressional fractures are typically closed and unlikely to increase flow by much, if at all. Heavy sediment infilling of fractures can potentially decrease hydraulic conductivity, while other fractures may grow wider and more open with dissolution of country rock (Bills et al., 2000). This dissolution or sedimentation in fractures can be largely dependent on country-rock composition, which also controls matrix permeability and porosity of the formation itself. Susceptibility of country rock to mechanical weathering can also be important in determining eruptive behavior: in explosive magma-water interaction, sediment content or "impurity" of the coolant is believed to affect MFCI as particles absorb heat that would otherwise transfer to the water (White, 1996; Wohletz, 1986). In environments with a "soft" substrate, volcanic tremor can lead to liquefaction of saturated sediment, producing a slurry that may then interact with magma in unique ways (Auer, et al., 2006; White, 1996). It is therefore crucial to understand structure and composition of bedrock to understand how water may move through and interact with magma in the subsurface in the event of an intrusion.

The development of diatremes is typically modeled based on location of both the water table and MFCI explosions as the eruption progresses (Lorenz, 1986; Valentine and White,

2012). In the current conceptual model (Fig. 2; Valentine and White, 2012), explosions may occur at any depth below the critical pressure of water (P = 22.5 MPa) throughout eruption. Deeper explosions brecciate country rock and contribute to the recycling of water and lithic and juvenile material. Higher lithostatic pressure and, in turn, country-rock strength prevent deep explosions from being as efficient, or as destructive, as those that occur closer to the ground surface. Shallow explosions occurring under decreased pressure and surrounded by weaker country rock are generally capable of excavating a larger area surrounding the explosion sites, ejecting material onto the surface and producing a crater. As explosions progressively disrupt the shallow subsurface, broken-up material slumps into the vent, further widening the diatreme near the ground surface (Valentine and White, 2012).

The conceptual model described above assumes a static, and presumably shallow, water table, with MFCI occurring throughout the water-saturated diatreme. In some cases, the water table may depress and result in overall progressively deepening explosions, as country-rock permeability may limit rapid groundwater recharge toward the diatreme (Sweeney and Valentine, 2015; Valentine and White, 2012). An understanding of rock properties and hydrogeologic setting is therefore necessary to identify where efficient MFCI may occur.

Valentine et al. (2014) calculated explosion energies in typical phreatomagmatic eruptions based on theoretical and limited experimental data. Total driving energy is calculated using heat capacity, density, volume, and total temperature change of the magma, and assuming that the fraction of energy converted to kinetic energy during MFCI (i.e., MFCI efficiency) is 1-10%. Optimal and maximum depths of explosions to produce ejecta dispersal are determined based on these results: most ejecta-producing phreatomagmatic explosions probably occur above ~200 m depth, while explosions down to a maximum of ~500 m depth may rarely be powerful

enough to contribute material to surficial deposits. Throughout an eruption, explosions can occur at a wide range of depths, brecciating country rock and moving material up and down within the subsurface, but generally only those occurring above ~200 m, and mostly above ~100 m, are powerful enough to throw material out of the crater (Valentine et al., 2014). These depth estimates work well for eruptions that occur in locations with a surface water supply or a moderate-to-shallow water table. However, this is not always the case; maars occasionally form in locations where the water table is significantly deeper than 200 m, as it is in some arid and semi-arid environments (e.g., the San Francisco Volcanic Field, Arizona, USA, Bills et al. (2000)).

Continuous water supply in maar eruptions has been discussed in terms of upward recycling and debris jets within diatremes (White and McClintock, 2001; Ross and White, 2006). Upward recycling occurs as explosions that are too deep to eject material at the surface repeatedly disrupt and mix diatreme fill and associated groundwater (White and McClintock, 2001). Debris jets involve the same general concept, but are more focused. These jets, or streams, of material are sourced from phreatomagmatic explosions and consist of debris, steam, and liquid water that shoot upward through overfill (Fig. 2) (McClintock and White, 2006). The amount of liquid water (i.e., pore water) that can be resupplied in this way remains uncertain, as these subsurface processes cannot be witnessed in real time and research has been limited to observation of eroded diatremes. The amount of resupplied water is limited to the non-interactive water in an explosion, i.e., the pore water that was not directly involved in MFCI or otherwise erupted, e.g., as vapor, along with water that may have vaporized but then re-condensed.

Though these jets and recycling processes can move some liquid water upward, it is probably a limited amount. A sustained phreatomagmatic eruption requires abundant shallow

liquid water to interact with rising magma. If the water table at equilibrium is too deep to support efficient MFCI and ejecta-producing explosions, or if the water table depresses throughout an eruption as explosions use up available water, there must be some mechanism for moving substantial amounts of water up in the subsurface to produce shallow explosions prior to or early in an eruption. An example of this can be seen in descriptions of eruptive activity during the first weeks of the 1759-1774 eruption of El Jorullo in central Mexico. The eruption began with phreatic and phreatomagmatic activity, as well as what eye-witness accounts described as "pulses" of mud, steam, and water emerging from vents and springs, flooding the landscape (Gadow, 1930). It is evident in this case that groundwater was being superheated by shallow magma and driven out of the ground. Similar processes could be possible in areas with very deep water tables, and if so, the efficiency of these processes is likely affected by different variables such as country rock and aquifer properties.

In the eastern San Francisco Volcanic Field (SFVF) of northern Arizona, the water table is currently estimated to be well below the optimal depth for ejecta-producing phreatomagmatic explosions reported by Valentine et al. (2014). Regional cross-sections (Bills et al., 2000) and a water table elevation map (SGC, 2015) show water table depths ranging from ~275 to >600 m below the surface across much of the central and eastern parts of the volcanic field, while depths quickly shallow to the north as surface elevation drops off. However, the SFVF has been host to a small number of monogenetic maar eruptions. Colton Crater and Rattlesnake Crater both exhibit evidence of phreatomagmatism, but at different stages in their eruptions and of contrasting intensity and duration. Based on the current depth to water table beneath each of these maars and their respective behaviors, two questions remain unanswered:

1. How was the necessary quantity of water supplied to each eruption to drive efficient phreatomagmatic activity?
2. What caused these two eruptions to behave differently from one another, as well as from most of the eruptions in the SFVF?

To address these questions, I have constructed a series of models, using the TOUGH2 numerical simulator (Pruess et al., 2011), of possible pre-eruptive and syneruptive processes that occurred in the subsurface of each volcano. The TOUGH2 software was developed at Lawrence Berkeley National Laboratory for modeling geothermal reservoir systems and has grown to include capabilities for numerous geologic applications. The use of TOUGH2 to address questions related to shallow volcanic eruption processes is less common, but the software provides a unique method to explore dynamic thermohydrologic processes. The models presented in this work are designed specifically to highlight magma-water interactions based on hydrologic conditions in the subsurface and thermal properties of both the country rock and magma. They do not model the MFCI, but they show how water (as vapor and liquid) can move as driven by magmatic heat, setting up the conditions for explosive interaction through upward vapor-phase transport and condensation at shallower depths.

1.2. Geologic Setting

Colton Crater and Rattlesnake Crater are located in the San Francisco Volcanic Field (SFVF) of northern Arizona (Fig. 3). The SFVF is located on the southwestern margin of the Colorado Plateau and spans an area of approximately 4,700 km^2, consisting of over 600 eruptive centers. Volcanism in the SFVF began in the late Miocene epoch and continues to the present, primarily producing monogenetic basaltic volcanoes (Tanaka et al., 1986). Late Cretaceous to early Tertiary uplift and crustal compression of the Colorado Plateau produced extensive faulting

and folding throughout the region, followed by further faulting and jointing associated with Basin and Range extension (Bills et al., 2000).

Colton Crater, also referred to as Crater 160 (Colton, 1936 and Cummings, 1972) and Vent 5715 (Ulrich and Bailey, 1987), is located in the northern portion of the SFVF, approximately 3 km south of SP Crater and 20 km north of San Francisco Mountain (Fig. 3). The cone has a diameter of 2 km at its base and 1.2 km at the summit, and the crater floor is approximately 60 m below the surrounding surface elevation. A small cinder cone sits in the crater floor. The large cinder cone is primarily composed of welded or loose olivine basalt cinder beds overlain by a 15-m-thick palagonite tuff that contains mafic inclusions (mantle or lower crustal xenoliths) and lithic fragments from the underlying Permian Kaibab Limestone and Coconino Sandstone (Cummings, 1972). Lithic fragments from the Supai Formation may also be present in this deposit. On the northern rim of the crater, just below a low-relief saddle, the phreatomagmatic tuff deposits are sparsely exposed in an approximately 40-m-thick section. The deposits thin around the northwestern rim, and are not identified elsewhere in the crater (Fig. 4).

Water-magma interaction in the eruption of Colton Crater was probably largely controlled by water flow through the highly fractured limestone and sandstone units identified in lithic fragments. The eruption is interpreted as having initially formed a large scoria cone, with little to no MFCI, but an apparent change in the eruption produced explosive magma-water interaction that blew much of the cone off and produced a large crater (Van Kooten and Buseck, 1978). This behavioral change has been hypothesized to be the result of vent migration from the southern portion of the crater to the north, causing the conduit dike to intersect water-filled fractures (Leudemann et al., 2013). However, whether the migrating dike intersected water in fractures or the water reached the conduit in another way remains uncertain. The eruption

returned to dry, magmatic behavior, producing the small cinder cone in the center of the crater in the final eruptive stage.

Rattlesnake Crater is located approximately 20 km east of Flagstaff and 43.5 km southeast of Colton Crater (Fig. 3). The timing of the Rattlesnake Crater eruption is placed in the Younger Pleistocene/ Older Brunhes period, ~0.4-0.74 Ma (Moore and Wolfe, 1987). Rattlesnake Crater consists of a wide, semi-circular maar rim located north-northwest of a small scoria cone, which presumably overlies what was once the southern maar rim (Fig. 5). The exposed northern rim of the crater is composed of thick bedded phreatomagmatic tuff deposits with clasts of the underlying Kaibab Formation, and lesser amounts of Coconino Sandstone and red beds (likely Supai Formation). Fragments of the latter two increase in abundance in the upper tuff deposits, and red-bed lithic clasts are slightly more abundant at the base of the exposure (Valentine, 2012). A section of basaltic cinder deposits underlies the tuffs, suggesting an initial Strombolian eruption prior to phreatomagmatic activity (Schwoerer, 2014). The eruption appears to have then sustained consistent, pulsing phreatomagmatic explosions through most of its lifespan, followed by another brief period of Strombolian activity that produced the small scoria cone.

At present, two primary regional aquifers lie beneath the study area: the C (Coconino) Aquifer and the Redwall-Muav Aquifer. The C-Aquifer consists of the Kaibab Formation, Toroweap Formation, Coconino Sandstone, Schnebly Hill Formation, and Supai Group. The Redwall-Muav Aquifer is located below the C-Aquifer and is contained within the units extending from the Redwall Limestone down to the Tapeats Sandstone on the Coconino Plateau (Fig. 6A) (Bills et al., 2016). The shallower C-Aquifer is considered to have been the primary water source for phreatomagmatic activity at both Colton and Rattlesnake Craters (Fig. 6B).

Based on depth and pressure constraints for production of efficient phreatomagmatic explosions and the apparent lack of xenoliths at either maar from units deeper than the Supai, the Redwall-Muav Aquifer is not considered to have been host to tephra-ring-producing phreatomagmatic explosions at the study locations and is not discussed further in this work.

CHAPTER 2: METHODS

2.1. Depositional Analysis

Field work was conducted during the summer and fall of 2016. Phreatomagmatic tuffs were analyzed at each crater to identify and estimate the relative abundance of different sedimentary clast types. The studied portion of Rattlesnake Crater tuffs is located on the northwest rim and is ~15 meters thick. Two samples were collected from near the bottom and near the top of the exposure. Three samples (lower, middle, and upper) were also collected from tuffs exposed in the northeastern rim of Colton Crater. Several samples of loose sedimentary lithic fragments were collected from each site as well.

Billets were cut from each of the five tuff samples collected. These were made into thin sections at National Petrographic Services. Thin sections were analyzed under a petrographic microscope and relative abundance of sand grains within the basaltic matrix was estimated. Interpretation of lithologic origin of individual sand grains was made based on analysis of thin sections from the Kaibab Formation, Upper and Lower Coconino Sandstone, and Upper Supai Formation. Annotated thin-section images are presented in Appendix B.

2.2. Fracture Analysis

The uppermost sedimentary units beneath both Rattlesnake and Colton Crater were studied to characterize and describe their fracturing patterns. Exposures of the Kaibab Limestone, Coconino Sandstone, and Supai Formation are not present within either Rattlesnake or Colton Crater, so nearby exposures of the Kaibab and Coconino Formations were selected for analysis. No Supai Formation is exposed in the region. The nearest exposure of Kaibab Limestone to Rattlesnake Crater is in San Francisco Wash, approximately 2 km north of the

crater rim (Fig. 3). An exposed section in the wash totaling ~20 m in thickness was studied during several trips over the course of approximately three weeks in July and August of 2016.

The nearest accessible exposure of Coconino Sandstone is located in Walnut Canyon (Fig. 3). A research permit was acquired, and a study site ~14 km southwest of Rattlesnake Crater was chosen. This site is located just east of Santa Fe Dam, and the exposed section of Coconino Sandstone extends up to ~30 m in thickness. Fracture analysis was limited to the lower ~15 m due to accessibility. The Coconino exposure quickly tapers out to the west of this study location.

Accessible sedimentary outcrops are scarce near Colton Crater, as the region is generally capped with lava flows from nearby cinder cones. The nearest exposures of Kaibab Limestone are located 5.6 km north of Colton Crater, within and around a large N-S-trending graben (Fig. 3). The western graben wall is ~40 m high and entirely Kaibab Limestone, but colluvium covers much of the slope. The studied sections of continuous Kaibab exposure were ~1-2 m thick. The nearest exposures of Coconino Sandstone are located within Wupatki National Monument, ~20 km to the east. Because of their distance and consequent lack of contiguity with Colton Crater, these outcrops were not studied.

A square meter was constructed of 0.75” × 1.5” pieces of poplar framing wood (Fig. 7) for fracture analysis. The square was placed against selected outcrops to maintain a set area for fracture measurement. Length and aperture of each fracture within the square was measured by hand with a measuring tape and ruler, and orientation was determined using a Brunton compass. All fractures with some measurable aperture were recorded, including those open at the surface and those partially filled by secondary mineralization or vegetation. Only minimal distinction between open, water-transmittable fractures and surficial weathering features was possible.

Effort was made to determine propagation of fractures deeper into the units, but limited exposure prevented significant investigation. For simplicity, all fractures included in permeability calculations are assumed to be continuous.

The described method allowed for complete measurement of all fractures in a set unit area. Permeability of each fracture has been calculated using the parallel plate law $k = a^2/12$, where a is fracture aperture (Lupi et al., 2011). A minimum, maximum, and average permeability for each was calculated based on individual fracture aperture range. Permeability ranges were then applied to system models.

2.3. Modeling

Potential eruption scenarios for each maar were simulated using the simulator TOUGH2 (Pruess et al., 2011) as it is invoked from the iTOUGH2 code, which provides enhanced control of TOUGH2 runs, among many other advanced features (Finsterle, 2007). TOUGH2 is a numerical simulator for non-isothermal, multiphase fluid flow in fractured and porous media. The simulator solves mass and energy balance equations for fluid and heat flow in space- and time-discretized systems, with the assumption of local thermodynamic equilibrium of all phases. Capabilities of the software extend to numerous geological and hydrogeological applications through various equation-of-state (EOS) modules. Modules are representative of specific fluid mixtures, or components, for which the modules provide the necessary thermophysical properties for mass and energy balance equations. The EOS3 module represents water and air, both of which are necessary for modeling shallow volcanic systems, and was therefore chosen for the scope and purposes of this work. In this module, water properties are calculated using the steam table equations from the International Formulation Committee, and air is approximated as an ideal gas (Pruess et al., 2011). Note that TOUGH2/EOS3 does not include the capability to

represent supercritical water (P > 22 MPa, T > 374 ºC). The TOUGH2/EOS1sc module is designed to model supercritical conditions and would therefore be capable of modeling more accurate temperatures for a magmatic intrusion; however, this module cannot operate with ambient air as a component, and instead requires a fully liquid-saturated or high-T vapor-saturated system (Magnusdottir and Finsterle, 2015; Finsterle, 2007). The EOS1sc module was tested for the relevant models, but was ultimately determined to be an unreasonable representation of the real physical systems of concern for this study. Therefore, EOS3 was used to investigate the relevant hydrologic processes with the understanding that modeled temperatures are lower than would be realistically expected in typical volcanic eruptions, but that the processes of vaporization, upward vapor flow, condensation, and downward liquid water flow would be analogous at higher temperatures.

A second limitation to TOUGH2/EOS3 is the termination of simulations as grid blocks become fully dried out, e.g., with high heat injection. TOUGH2/EOS3 can simulate single-phase gas, two-phase, and liquid-saturated conditions, but modeling full dry-out (transition to single-phase gas) can cause convergence problems, driving down the time-step size to the extent that the simulation stops progressing significantly in time. At this point the simulator is designed to stop to avoid unproductive use of computer time. Although some simulations do not run out to long times, the calculations are correct up until the point where convergence is difficult, time steps are cut, and the simulator stops.

A computational mesh file representing the discretized physical system to be modeled is necessary for TOUGH2 simulation. A mesh consists of a specified number of grid blocks, which are each assigned primary thermodynamic variables (dependent on the chosen EOS module) and material properties including permeability, porosity, and specific heat capacity. A figure showing

input file format and a full list of associated variables are included in Appendix C. The primary variables for EOS3 in two-phase conditions are pressure (P), temperature (T), and gas saturation (S_g). The number of mass and energy balance equations to be solved for each grid block corresponds to the number of primary thermodynamic variables. With execution of the code, sets of coupled nonlinear equations for all grid blocks are solved simulateously using Newton-Raphson iteration (Pruess et al., 2011).

For the simulations carried out in this study, all mesh files are two-dimensional and 1-m thick in the y-direction. Numerous mesh files of varying sizes were created for model simulations, with the largest extending to 710 m depth and 1,200 m width. The primary mesh files used are a "zoomed in" view of the upper portion of the aquifer and up to the surface. For both craters, this mesh is 300 m wide and 425 m deep, extending approximately 80 m below an approximately 345-m-deep water table. Individual lithologic units are distinguished in the mesh creation process to assign set volumes to each grid block of that rock type, determined based on unit thicknesses (i.e., 75 m thick unit = 5 blocks × 15 m). The standard mesh contains a total of 1,260 individual grid blocks. A sample of a mesh file is provided in Appendix C.

Initial model runs were performed to establish gravity-capillary equilibrium in the subsurface prior to any heat input. Capillary pressure (P_{cap}) and relative permeability (k_{rel}) conditions were determined using the van Genuchten-Mualem method (Pruess et al., 2011), with relevant P_{cap} and k_{rel} input values selected for each rock unit (Appendix C). All blocks located at the estimated water table depth were given atmospheric pressure (1.0×10^5 Pa), 50% liquid saturation and assigned Dirichlet boundary conditions (i.e., very large volumes, $\sim 1.0 \times 10^{49}$ m^2) to prevent their thermodynamic conditions from changing. The output data from this simulation were then used as the initial conditions for a second run, with the water table set to normal grid

block volumes (active) and the bottom boundary of the mesh set to very large volumes. The output file from this simulation was then used as the starting run for further simulations with heat injection.

Subsequent equilibrium files were produced with a 20-m-wide "fracture zone," or a high-permeability, high-porosity feature in the center of the model. This zone is intended to represent the combined effects of numerous smaller fractures likely present in the subsurface units. Some fractures in the region are contained within individual units, but most faults propagate through the entire aquifer (Bills et al., 2000). Fracture-zone heights were varied for different models, but the base-case models were each run at least twice to include (1) a fracture zone that extends from the Kaibab-Coconino boundary (75 m depth) to 425 m depth, within the saturated Supai Formation, and (2) a zone fracture that extends from the surface to 425 m depth. In additional simulations, the fracture zone extends from the Kaibab-Coconino boundary to the top of the water table, or nearly the total extent of the Coconino Sandstone. The fracture zone was given the same capillary pressure (P_{cap}) and relative permeability (k_{rel}) parameters as the unit in which it is located. Several additional gravity-capillary equilibrium runs were also created from this point to represent various starting conditions, including those with the water table set shallower or deeper, and others with adjusted country-rock permeability, porosity, etc.

With equilibrium conditions set, numerous forward models were produced for each eruption to understand how specific rock and thermodynamic parameters affect model outcomes. Ascending magma is modeled as heat injection into specified grid blocks, described only by a heat rate (J/s). This rate was estimated using the equation:

$$q = -K(\Delta T/\Delta z)$$

where q= heat rate (J/s), K= thermal conductivity (W/m K), and $\Delta T/\Delta z = (T_{rock} - T_{magma})/ (z_{rock} - z_{magma})$. The parameter Δz or $(z_{rock} - z_{magma})$ is also called the thermal boundary layer, or S_{TBL}, calculated using the equation:

$$S_{TBL} = \sqrt{(\kappa\tau)}$$

where the thermal diffusivity (κ) is defined as $\kappa = K/(\rho C_p)$, and τ = time scale. Values for magma temperature and thermal conductivity were based on properties of a typical tholeiitic basalt melt (Morrissey et al., 2000), and heat capacity of wet sandstone (C_p) was estimated based on published values (Eppelbaum et al., 2014; Bralower and Bice). The complete calculation of heat flow rate is presented in Appendix C. A range of heat flow rates was tested in models as described in Results (Chapter 3).

Simulations were typically run sequentially, adjusting locations of heat injection, or magma movement, as well as opening up zones of high permeability to represent areas where MFCI explosions could occur. Values for several country-rock (sandstone, limestone) properties were based on published values, including density, porosity (Manger, 1963; Ai and Ahrens, 2003), permeability (Bear, 1988), specific heat capacity, and thermal conductivity (Eppelbaum et al., 2014). Coconino Sandstone permeability was calculated using hydraulic conductivity values from a well ~21 km to the east (Fig. 3) (Hoffman et al., 2006). A range of fracture permeabilities was tested based on the described calculations.

2.3.1. Model Data Processing

Total volume of liquid water moved above a depth of 205 m was calculated for some simulations. The TOUGH2 simulator produces a printout of primary variables (P, T, and S_g) for each grid block at the final time step of each simulation. These data were processed to view only

grid blocks above 205 m, and liquid saturation of these grid blocks was calculated by subtracting the gas saturation value from 1 ($S_g + S_l = 1$). Total pore space volume (V_{pores}) of each grid block was calculated by multiplying porosity (φ) by the total grid block volume (V_{total}) , then the total volume of pore space occupied by liquid water (V_{liq}) was calculated by multiplying S_l by V_{pores}. The sum of V_{pores} for all grid blocks above 205 m depth is the total volume of liquid water in the model above that depth at the final time step. This calculation was initially performed for the gravity-capillary equilibrium model to determine the total volume of residual water in pores above this depth prior to any heat injection. This initial total volume of residual liquid water was then subtracted from the new calculated V_{liq} after each simulation to determine the total volume of liquid water brought upward as a result of heat injection. These values, where reported, are only representative of the volume of liquid water moved above this depth in the modeled two-dimensional domain that is only 1 m thick and are not representative of the volume that would realistically be moved in an actual three-dimensional system.

CHAPTER 3: RESULTS

3.1. Stratigraphy Estimates

Depths and thicknesses of the stratigraphic units beneath each volcano were estimated based on a series of cross-sections by Bills et al. (2000). None of the transects crosses directly through either location, so estimates are based on weighted averages of transects that passed nearest to each. All estimates are shown in Table 1 and Fig. 6B.

Estimated Stratigraphy				
Volcano	Unit	Top depth (m)	Base depth (m)	Thickness (m)
Rattlesnake Crater	Kaibab LS	0	75	75
	Coconino SS	75	350	275
	Supai Group	350	835	485
Colton Crater	Kaibab LS	0	75	75
	Coconino SS	75	375	300
	Supai Group	375	855	480

Table 1: Approximate depths and thicknesses of uppermost stratigraphic units beneath Rattlesnake and Colton Craters. Based on data from Bills et al. (2000).

3.2. Water Table Estimates

Water table depth at each volcano was estimated using data from nearby wells (Figure 3), regional cross-sections, and potentiometric surface maps. Based on data from several wells near Rattlesnake Crater, primarily four located ~1.5 km SW, ~6.8 km WSW, ~20.8 km ESE, and ~6.5 km N, and estimates from two nearby cross-sections (Appendix A), the water table is estimated to be currently at a depth of ~315-350 m. This estimate places it in the lower Coconino Sandstone, or in the very upper part of the Esplanade Sandstone of the Supai Group (Hoffman et al., 2006; Bills et al., 2000; ADWR). Well data are limited near Colton Crater, and cross-

sectional interpretations are located too far from the study site to provide a useful estimate. The potentiometric surface estimate in this area is primarily based on a water-table elevation map that shows a steep gradient in this region (SGC, 2015). The water table beneath Colton Crater is estimated to be ~340-380 m depth, roughly in agreement with data from sparse nearby wells, placing it within the base of the Coconino Sandstone or top of the Upper Supai Formation (Bills et al., 2000; ADWR).

The water table was likely close to these estimated levels at the time of the eruptions. Regional topography and elevation of groundwater outflow into the Little Colorado River basin in the Pleistocene epoch are interpreted to have been similar to present day (Holm, 2001), which allows the inference that groundwater levels would have also been approximately the same as they are today.

3.3. Fracture Analysis

The Kaibab Limestone and Coconino Sandstone both contain significant fracturing. The studied Coconino Sandstone exposure is located in Walnut Canyon, SW of Rattlesnake Crater (Fig. 3). The sandstone unit is characterized by large fractures, each cutting through meters of the formation (Fig. 10). Fractures are most commonly subvertical to vertical, but a few subhorizontal fractures were recorded, and partially open bedding planes may also act as a means of fluid flow through the unit. Most fractures trend NW-SE to W-E, with the exception of one section of fractures primarily trending ENE-WSW. The mode of average fracture aperture in the Coconino outcrops is 2.5 mm, and average is 3.2 cm. Apertures generally range from closed, or less than 0.5 mm, up to ~28 cm. Excluded from this averaging is a large opening, ~6.1 m wide, that is filled in with sediment and trees. Vegetation cover prevented investigation of the continuity of this presumed fracture.

Fracture characteristics in the Kaibab Limestone vary widely even between vertical sections only meters or tens of meters apart. In general, the uppermost studied sections of Kaibab are highly weathered and contain abundant small fractures, dissolution channels, and voids (Fig. 8). In deeper sections, such as the base of the exposure in the San Francisco Wash, dissolution is notably absent and fracturing is dominated by larger-scale features (Fig. 9). Large-scale fractures typically are nearly vertical and trend NW-SE, while orientation of smaller fractures is highly variable. Some outcrops have fractures that nearly all trend NW-SE, while others are dominated by fractures trending NE-SW. The mode of the average fracture aperture in the Kaibab is ~0.5-1.0 mm, with values ranging from 0 mm to a few as wide as ~8 cm. The largest vertical fractures identified in the Kaibab exposures trend WNW-ESE to NW-SE (108˚-129˚) and are ~4.6 m long with ~3-5 cm apertures (Fig. 8C). All fracture data are in Appendix B.

3.4. Thin Sections

Five thin sections were analyzed from the two volcanoes: three from Colton Crater and two from Rattlesnake Crater. Samples were taken from the lower, middle, and upper parts of the exposed ~40-m-thick Colton Crater tuff section (CL, CM, and CU, respectively), and from the lower and upper ~25-m-thick tuff outcrop at Rattlesnake Crater (RL and RU, respectively. The purpose of this petrographic analysis was primarily to analyze quartz sand content within the tuff matrix, in an effort to quantify the relative proportions of Coconino and Supai sand that may be present at different times of the eruption. While some xenoliths of the underlying sedimentary units are preserved in deposits, much of the rock surrounding an explosion site could have been completely disaggregated, resulting in quartz grains becoming entrained in the matrix. These data can provide depth information for explosion sites.

The Colton Crater and Rattlesnake Crater tuff thin sections are described in the following sections (3.4.1. to 3.4.5.). Percentages of each component and mineral type are visually estimated. Thin sections of the Kaibab Formation, Upper and Lower Coconino Sandstone, and Supai Formation used for interpretation of quartz grain lithologic origin are briefly described in Section 3.4.6.

3.4.1. CL

Total sample: ~22% ash matrix, ~23% matrix minerals, ~55% scoria

Ash matrix: Gray glass, very fine, indistinguishable shards.

Matrix minerals: ~90% quartz (sedimentary), ~6% pyroxene, 2% k-feldspar, <1% sparse plagioclase feldspar, and minor (<1%) olivine.

Quartz: Rounded to subangular, varying in size from ~0.1 to 0.65 mm. Smaller quartz grains (~0.1-0.3 mm) are dominantly subrounded to rounded, while larger grains (up to 0.65 mm) are commonly subangular.

Feldspars, pyroxene, olivine: ≤ 3-mm partially resorbed k-feldspar crystals, <0.1-mm to 1.5-mm anhedral to subhedral pyroxene crystals, sparse <0.1-mm plagioclase laths and <0.2-mm olivine crystals.

Scoria: Cinders and juvenile basalt clasts ranging from ~3 mm to >1 cm. Clasts contain abundant 0.1- to 0.2-mm plagioclase laths and small 0.1-mm subhedral pyroxene crystals (<0.3 mm).

3.4.2. CM

Total sample: ~35% ash matrix, ~10% matrix minerals, ~54% scoria, <1% lithic fragments.

Ash matrix: Very fine dark gray to red-orange glass fragments. High degree of alteration/ oxidation throughout.

Matrix minerals: ~75% quartz (sedimentary), 20% pyroxene, ~3% k-spar, ~1% olivine, and ~1% plagioclase

Quartz: Crystals range in size from <0.1 mm to 0.8 mm (rare), primarily <0.25 mm. Finer quartz fragments typically subangular to angular. Subrounded to rounded crystals notably less abundant than in CL.

Feldspars, pyroxene, olivine: Partially resorbed anhedral to subhedral pyroxene and feldspar crystals generally ranging from <0.1 mm to ~0.5 mm. Very sparse plagioclase, typically <0.2 mm. Few large pyroxenes (~5% of total pyroxenes), ~1.0- to 2.0-mm in size, and one ~4-mm, partially resorbed, subhedral pyroxene present. Sparse olivine crystals up to ~1-mm. Largest crystals typically highly altered.

Scoria: Cinders and basalt clasts generally range from ~0.3 to 1.1 mm and rarely up to 9 mm in size, some containing abundant plagioclase laths and sparse euhedral pyroxenes (typically ~0.1 to 0.5 mm), possible including sparse olivine crystals. Largest plagioclase in a single scoria clast ~0.5 mm. Several large orange glassy clasts (up to ~3 mm), highly vesicular, containing sparse ≤0.1-mm pyroxene or olivine crystals.

Lithic fragments: Sparse ~1.5- to 2-mm clasts, possibly limestone (appear to be calcite).

3.4.3. CU

Total sample: ~16% ash matrix, ~20% matrix minerals, ~63% scoria, ~1% lithic fragments.

Ash matrix: Overall poorly welded matrix. Glass shards dominantly very fine, subangular, tinted brown in PPL. Glass less abundant than in CL and CM.

Matrix minerals: ~80% quartz (sedimentary), ~14% pyroxene, ~4% k-feldspar, ~1% plagioclase, <1% olivine

Quartz: Abundant 0.1-mm to 0.3-mm subrounded to rounded crystals (~85%). Additional ~15% finer (~0.02 to 0.1 mm), subangular crystals.

Feldspars, pyroxene, olivine: Subhedral pyroxene phenocrysts and sparse plagioclase range from 0.01 mm to 1 mm. Very sparse <0.01-mm plagioclase laths and large pyroxenes (up to ~3.5 mm), partially resorbed. Sparse olivine crystals, generally ~0.1-0.2 mm, partially resorbed.

Scoria: Ranges in size from ~0.1-8 mm, primarily containing <0.1- to 0.2-mm euhedral and subhedral pyroxenes and very minor olivine. Larger grains up to ~1.5 mm, anhedral. Largest scoria fragment found composed almost entirely of <0.2-mm plagioclase laths and pyroxenes;

Lithic fragments: One ~2-mm moderately cemented sandstone xenolith, containing subangular to subrounded, ~0.02-0.1-mm quartz grains. One ~1-mm sandstone lithic also present, containing <0.1-mm subangular to rounded quartz crystals.

3.4.4. RL

Total sample: ~22% ash matrix, ~28% matrix minerals, ~50% scoria.

Ash matrix: Gray, very fine glassy matrix. Sparse calcite precipitation.

Matrix minerals: ~80% quartz (sedimentary), ~13% pyroxene, ~5% k-feldspar, ~2% plagioclase

Quartz: Abundant rounded to subrounded quartz grains ranging in size from ~0.1-0.6 mm, ~90% of total quartz. Smaller (<0.1 mm) subangular grains ~10% of total quartz.

Feldspars & pyroxene: Subhedral pyroxene crystals, minor potassium feldspar (mainly orthoclase), and small plagioclase laths (all <0.3-mm). Few large (up to ~2 mm) pyroxene and orthoclase crystals. Little alteration on minerals.

Scoria: Clasts generally range from ~0.5- to 4 mm, generally consisting of ~50-60% plagioclase laths (~0.1- to 1.2 mm) and 40-50% euhedral pyroxenes (~0.1- 1.5 mm). Typically highly vesicular. Four large ~8 mm clasts present in sample, one of which contains ~70% plagioclase, 30% pyroxene.

3.4.5. RU

Total sample: ~19% ash matrix, ~25% matrix minerals, ~5% secondary calcite, ~50% scoria, <1% lithic fragments.

Ash matrix: Gray to black, very fine glassy matrix, voids infilled with significant secondary calcite.

Matrix minerals: ~88% quartz (sedimentary), ~8% pyroxene, 3% k-feldspar, 1% plagioclase

Quartz: Range in size from ~0.01 to 0.6 mm, generally rounded to subrounded, although smallest fragments may be subangular.

Feldspars & pyroxene: Sparse loose plagioclase (~0.2-mm) and subhedral to euhedral pyroxene crystals (typically ~0.1-0.3 mm). Sparse large (up to ~2 mm) pyroxene and highly altered, possible orthoclase crystals.

Scoria: Average ~0.1- to 1.0 mm and as large as 0.8 mm. Plagioclase in clasts typically ~0.2 to 0.5 mm, few up to ~1.0 mm. Subhedral to euhedral pyroxenes ~0.1 to 0.2 mm in size, often significantly altered. Significantly fewer juvenile clasts overall than RL.

Lithic fragments: Very sparse <2-mm lithic clasts, dominantly appear to be sandy limestone. Composed of rounded quartz grains (<0.1 mm) within calcite cement.

3.4.6. Paleozoic Sedimentary Units

Kaibab Formation: Calcite with sparse ~0.1 to 0.16-mm subangular to subrounded quartz grains.

Upper Coconino Sandstone: Bands of ~0.25 to 0.7-mm, primarily rounded to subrounded quartz (some subangular), and ~0.5 to 0.2-mm subrounded quartz grains.

Lower Coconino Sandstone: Rounded to subrounded quartz grains, ~0.1-0.2 mm.

Upper Supai Formation: Dominantly ~0.01 to 0.1-mm angular to subrounded quartz grains.

3.5. Modeling

3.5.1. Model Setup

Colton Crater's and Rattlesnake Crater's underlying stratigraphy are very similar and, for this reason, the same mesh setups were used to represent both volcanoes. Estimated thickness of the Coconino Sandstone varies by ~25 m, within a reasonable uncertainty range for the method of estimation. Water-table depth estimates are also varied, but both average between ~330-360 m. The same models were tested with a range of water table depths to account for this variation.

Rattlesnake Crater's depth to groundwater is likely closer to ~315 m based on the closest well; however, this well data was discovered late in the modeling and writing process. The base case depth of ~350 m is therefore considered an upper limit for the modeled processes at Rattlesnake Crater.

Based on estimated hydraulic conductivity values for each of these units from nearby wells, permeability of the Coconino Sandstone is estimated to be ~1.01×10^{-11} m^2 and permeability of the Upper Supai Formation is calculated to be ~1.13×10^{-12} m^2. All estimated country-rock properties and initial conditions are given in Tables 2 and 3.

Figures produced for each model show pressure (Pa), temperature (°C), and gas saturation (%) at the final time step of the simulation. Note that the figures do not show the outermost 10 m of the models as a result of the figure creation process, but this space is included in the simulations. Gas saturation plots are overlain with gas flow vectors, which are scaled according to relative magnitude.

3.5.2. Gravity-Capillary Equilibrium

To simulate the various cases of thermal perturbation and associated heating and water re-distribution (e.g., upward convection of vapor with or without condensation, and downward water flows) caused by magma intrusion at the base of the model domain, a static gravity-capillary equilibrium is needed as an initial condition. The gravity-capillary equilibrium is a state of a hydrologic system in which the downward gravity forces are balanced by the capillary forces of the porous medium such that the liquid (aqueous) and vapor (gaseous) phases of water and the air gas phase are all at a static equilibrium. In this condition, the gas phase (where present) attains a gas-static pressure gradient, and regions of the system that are fully liquid-saturated (no gas present) attain a hydrostatic pressure profile. Two-phase regions are at gravity-

capillary equilibrium. This is a necessary initial condition to avoid simulating a system in which both a gravity-capillary equilibration process may be going on at the same time as a thermal perturbation associated with magma intrusion. In short, to focus the simulations on the magmatic heating process, we utilize a plausible long-term static steady state as an initial condition.

The standard gravity-capillary equilibrium (Case 0) was first constructed for a steady-state, non-fractured, non-heated subsurface with standard rock properties (Table 2), initial temperatures from 10-20 ºC, and initial liquid saturations (Table 3), and hydrostatic pressure at the water table set to standard atmospheric pressure. The results of this simulation are shown in Fig. 11. This simulation produces a gas-static pressure from the surface to the water table at 345 m depth, which is held at standard atmospheric pressure, and a steadily increasing pressure gradient from the water table down to the base of the model. Although a temperature gradient may be expected from the surface to 425 m depth, we assume isothermal conditions in the entire model at ~20°C. This assumption is justified by the observation that this falls within the range of shallow spring waters (~13-17°C) and deeply derived spring waters (22-31°C) in the Grand Canyon (Crossey et al., 2006), and reported temperatures for nearby wells range from ~16-18.7°C (Hoffman et al., 2006; Bills and Flynn, 2002). Furthermore, the thermal perturbation associated with the magma is much larger than 20°C, making small variations around 20°C negligible. Gas saturation is initially set at 80% in the Kaibab Limestone and 70% in the Coconino Sandstone, making these units part of a deep unsaturated zone. An ~60-m-thick unsaturated zone of gradually decreasing gas saturation and increasing liquid saturation (as depth increases) forms above the 345-m-deep water table in the lower Coconino Sandstone, below which all blocks are fully liquid-saturated. The presence and location of the fracture zone does not make a noticeable impact on the equilibrium conditions of the model.

Table 2a

Standard Model Inputs							
Unit code	Description	Thickness (m)	Density (kg/m^3)	Porosity (%)	Permeability (m^2)	Conductivity (W/m°C)	Specific Heat (J/kg°C)
KLIME	Kaibab LS	75	2560	15	1.05E-12	2.70	910
CSAND	Coconino SS	275	2450	25	1.01E-11	2.51	920
WATBL	Water table (Coconino)	10	2450	25	1.01E-11	2.51	920
FRACK	Fracture in Kaibab	75	1300	70	1.00E-09	0.00	1000
FRACC	Fracture in Coconino/ Supai	345	1300	70	1.00E-09	0.00	1000
AQUIF	Aquifer (Supai Fm)	75	2500	25	1.13E-12	2.70	920
BOUND	Supai Fm	--	2500	25	1.00E-12	2.70	1.00E+05

Table 2b

Standard Large Model Inputs							
Unit code	Description	Thickness (m)	Density (kg/m^3)	Porosity (%)	Permeability (m^2)	Conductivity (W/m°C)	Specific Heat (J/kg°C)
KLIME	Kaibab LS	75	2560	15	1.05E-12	2.70	910
CSAND	Coconino SS	275	2450	25	1.01E-11	2.51	920
WATBL	Water table (Coconino)	10	2450	25	1.01E-11	2.51	920
UPSUP	Upper Supai Fm (saturated)	105	2500	25	1.13E-12	2.70	920
SUPAI	Middle Supai Fm (saturated)	255	2500	25	1.13E-12	2.70	920
FRACK	Fracture in Kaibab	75	1300	70	1.00E-09	0.00	1000
FRACC	Fracture in Coconino/ Supai	345	1300	70	1.00E-09	0.00	1000
BOUND	Supai Fm	--	2500	25	1.00E-12	2.70	1.00E+05

Table 2: Standard model inputs for the small models (**2a**) and large-scale models (**2b**).

Table 3a

Initial Conditions for Gravity-Capillary Equilibrium			
Unit code	Pressure (Pa)	Gas Saturation (%)	Temperature (°C)
KLIME		80	10
CSAND		70	20
WATBL	1.00E+05	50	20
AQUIF		1.00E-05	20
BOUND		1.00E-05	20

Table 3b

Initial Conditions for Large Model Gravity-Capillary Equilibrium			
Unit code	Pressure (Pa)	Gas Saturation (%)	Temperature (°C)
KLIME		80	10
CSAND		70	20
WATBL	1.00E+05	50	20
UPSUP		1.00E-05	20
SUPAI		1.00E-05	20
BOUND		1.00E-05	20

Table 3: Initial conditions for small models (**3a**) and large-scale models (**3b**).

3.5.3. Rapid Timed Heat Injection

Numerous models were run with timed heat injection moving upward from the bottom boundary of the model toward the surface, imitating the movement of magma. The timing of heat injection progressively upward was determined based on a magma rise rate that correlates with a volumetric injection rate of 0.5 m^3/s. This rate is considered an approximate minimum magma ascent rate based on estimates of effusion rates from several mostly basaltic eruptions (Walker, 1973). This heat injection schedule and location variation is a feature of TOUGH2 through the

input file (GENER block) and is modeled using both the smaller and larger meshes. A table of injection times with depth is presented in Appendix C. In the smaller models (425 m depth), rapid heat injection is shown both as reaching up to 100 m depth and up to the surface (Fig. 12). In models with varied parameters (permeability, porosity, etc.) and large models (710 m depth), the specified heat injection only extends upward to 95 m depth. Although this setup is intended to mimic an active eruption with magma reaching the surface, the models showing heat reaching the top boundary terminate after a very short time due to TOUGH2/EOS3 failing to converge when blocks become completely unsaturated, or "dry." For this reason, the models with heat injection only up to 95 m in depth represent a system early in its eruption process as magma is ascending, but over a longer period of time than would likely elapse in an actual eruptive event.

3.5.3.1. Small Models at Standard Conditions

Case 1.1 shows rapid timed heat injection into a mesh with a fracture zone extending from the ground surface to 425 m depth, within the saturated Supai Formation. Heat is injected up to 95 m depth over the course of 660 seconds, or eleven minutes. The setup for Case 1.2 is identical, but the fracture zone extends only up to the Kaibab-Coconino boundary from 425 m depth. Both models are run for ~3.1 days, and pressure, temperature, and gas saturation at the final time step for each model run are shown in Fig. 13. The highest pressure zones (up to 2.2×10^6 Pa) form around either side of the fracture-zone pathway within the liquid-saturated base of the models, while the fracture-zone pathway itself has a significantly lower pressure. The maximum temperatures occur within the middle to upper part of the fracture zone, reaching ~500˚C, but temperatures within the aquifer do not exceed ~220˚C. The gas saturation plot shows how the water has moved as a result of the injected heat. Around the heat injection in the saturated base and up into the fracture zone, the pore space reaches 90-100% heated vapor by

volume (i.e., grid block gas saturation equals 90-100%). In the center of the model, the original water table is now raised, with grid blocks with 90-100% liquid-saturation now reaching upward to a depth of ~300 m. Grid blocks containing up to ~60% liquid saturation are now present on either side of the fracture zone and into the base of the Kaibab Limestone. Vectors show strong upward vapor flow through the fracture zone, while smaller magnitude vapor flows are seen on either side of the fracture pointing outward.

3.5.3.2. Large Model at Standard Conditions

Heat is injected into the large model (Case 1A) at the same rate corresponding to 0.5 m^3/s of magma over 1,150 seconds (>19 minutes) up to 95 m below the surface. The bottom four rows, or 45 m, of the model are set to have constant heat injection in an area 600 m wide from the beginning of the run. Step-wise heat injection then begins at 665 m depth at 30 seconds. At the water table, the injection has tapered to a width of 60 m. This model continued for a maximum of 2.4 days, and final conditions are shown in Fig. 14.

Results of this setup show maximum pressure of $>3.5 \times 10^6$ Pa at the base of the aquifer, gradually decreasing upward in the zone of heat injection. Fracture-zone pressure within the aquifer ranges from $\sim 1.6 \times 10^6$ to 1.0×10^6 Pa, immediately surrounded by pressures up to $\sim 2.67 \times 10^6$ Pa in the lower permeability Supai Formation. The maximum temperature reached in this model is just above 200 ˚C in the upper aquifer, dropping to less than 130 ˚C high in the fracture zone. The plot of gas saturation shows that the blocks in the zone of high *T* at the top of the aquifer consist of increased vapor saturation; just above this, several blocks of increased liquid saturation (>~70%) are seen as high as 285 m depth. Zones of increased liquid saturation extend

up to 40 m laterally away from the fracture zone within the unsaturated Coconino Sandstone. Near the Kaibab-Coconino boundary, liquid saturation reaches ~50%.

3.5.3.3. Sensitivity Analysis

Sensitivity analysis involves studying changes to model outcome arising from variation of individual parameters, or testing to see how dependent the simulated model results are on each of the input parameters. Several parameter variations were applied to the rapid heat injection models. These variations include: high-permeability rock units (Case 1B), low-permeability rock units (Cases 1C and 1D), high-permeability and porosity fracture zone (Case 1E), anisotropic permeability rock units (Case 1F), high-porosity (Case 1G), low porosity (Case 1H), high heat rate (Case 1J), low heat rate (Case 1K), a high water table (Case 1L), a low water table (Case 1M), and doubled fracture zone width (Case 1N). Those with the highest degree of variability are described below and summarized in Table 4. Pressure, temperature, and gas saturation plots for all others are presented in Appendix C.

Permeability and Porosity

A range of high and low permeabilities was tested. Case 1A shows the base case with increased country-rock permeability. Coconino Sandstone permeability is increased to 8.97×10^{-11} m^2 (from 1.01×10^{-11} m^2), and the same permeability and density are given to the Supai Formation. Boundary blocks have also been given the same density as the Coconino Sandstone and aquifer of 2,450 kg/m^3 (decreased from 2,500 kg/m^3), and a porosity of 15% (decreased from 25%). All other parameters remain unchanged. Final conditions of this simulation at 2.1 days are shown in Fig. 15 alongside those for the base case (Case 1.1) at the

same time (2.1 days). The high-permeability model shows a wider area of impact around the heat injection. A pressure gradient is seen within the aquifer, and changes are widespread around the intersection of the fracture zone and water table. Total pressure is generally lower in the model of high permeability, reaching a maximum of ~8.55×10^5 Pa vs >1.8×10^6 Pa in the base case. Temperature is also generally kept lower, reaching a maximum of ~170˚C, and the plot of gas saturation shows vapor and associated condensation reaching outward 40 m laterally from the fracture zone up to nearly 100 m depth.

Permeability is decreased in Cases 1C and 1D. Case 1C has adjusted Coconino Sandstone and Supai Formation permeabilities calculated using low hydraulic conductivity values from nearby wells. Coconino permeability is decreased to 6.3×10^{-14} m^2 and Supai permeability is decreased to 1.8×10^{-14} m^2. This model runs for 1.4 days (Fig. 16). In general, heat and fluid flow effects are restricted to within the fracture zone and the two immediately adjacent grid block columns. A pressure increase seen in the Coconino Sandstone surrounding the fracture zone in the base-case model is nonexistent, but instead the pressure within the fracture zone is increased up to <100 m depth. Maximum T within the fracture zone reaches over 450˚C (more than double that of the base case), and vapor formation is nonexistent within the aquifer itself, but rather is confined to the fracture zone. Condensed water does, however, appear as high as ~60 m depth within the Kaibab. Case 1D utilizes an average permeability between the base case conditions and the 1C models. Conditions at 1.4 days are very similar to the base case, but the higher-pressure field within the Coconino sandstone is slightly larger and overall temperatures are slightly increased.

In Case 1E, fracture zone permeability has been increased by two orders of magnitude and porosity is increased 10% (absolute increase). With heat injection up to 95 m, this model

runs for a maximum of ~1.2 days. In general, results are very similar to base case conditions at the same time step. The region of increased pressure and temperature in and around the fracture zone extends slightly farther into the Kaibab Limestone, temperatures are slightly higher, and gas saturation around the fracture zone is slightly increased. Results and figures are presented in Appendix C.

Anisotropic permeabilities in the Coconino Sandstone and Supai Formation are modeled in Case 1F, shown in Fig. 17 at ~2.7 days. Permeability for both units has been increased by an order of magnitude in the x-direction. The zone of vapor transport and condensation is broader than in the base-case model, extending 80 m laterally from the fracture zone above the water table, but only a small amount of vapor reaches the Kaibab Limestone. The water table is raised by ~20-30 m. Maximum pressures are lower and general temperatures are similar, but T_{max} reaches ~500ºC.

Increased and decreased country-rock porosity are modeled in Cases 1G and 1H, respectively. An absolute 10% increase of porosity has little visible impact on pressure and temperature, but decreases vapor formation within the aquifer and condensation around the fracture zone. By contrast, decreasing porosity 10% produces higher pressures, temperatures, and gas saturation throughout (Appendix C).

Heat Rate

Heat rate is increased and decreased by 4.5×10^5 J/s to 1.0×10^6 J/s and 1.0×10^5 J/s in Cases 1J and 1K, respectively. Increasing heat rate (Case 1J) accelerates the evolution of the system and very similar conditions in 1.8 days are produced in the base case at 3.1 days. Compared to the base case at the same time step, increased heat rate causes significantly higher

P and *T*, and a much greater quantity of vapor and liquid water are moved upward (Fig. 18). Compared to the base case at 3.1 days, however, the only notable difference of the increased heat-rate run at 1.8 days is a slightly higher P_{max}, reaching $>3.0 \times 10^6$ Pa. Decreasing heat rate (Case 1K) shows sharp contrast to the base case and runs for 13 days (Fig. 19). Maximum pressure around the fracture zone within the aquifer reaches only $\sim 11.5 \times 10^5$ Pa, temperature in the fracture zone does not exceed ~220˚C, and S_g reaches 100% only within the fracture zone. Cooler temperature allows liquid saturation to remain within the aquifer, even in the zone of direct heat injection.

Rapid Heat Injection Model Variation Tests						
Case #	File Name	Description	Changed Variable	New Value	Base-Case Value	Observed Changes
1B	rcm1aug17a3	High *k*- rock units	CSAND, WATBL *k* (m^2)	8.97E-11	1.01E-11	Larger area of vaporization and condensation within country rock and surrounding fracture zone
			AQUIF *k* (m^2)	8.97E-11	1.13E-12	
1C	rcm4sept17f-mk	Low *k*- rock units	CSAND, WATBL *k* (m^2)	6.30E-14	1.01E-11	Heat and fluid flow largely restricted to fracture zone and adjacent blocks; No vapor formation in aquifer outside the fracture zone; Condensed water up to ~60 m
			AQUIF *k* (m^2)	1.80E-14	1.13E-12	
			BOUND *k* (m^2)	1.80E-14	1.00E-12	
1D	rcm4sept17f-ak	Moderately low *k* rock units	CSAND, WATBL *k* (m^2)	5.10E-12	1.01E-11	Very similar to standard model, but the high-*P* zone in the Coconino is slightly larger and temperatures are slightly increased
			AQUIF *k* (m^2)	5.70E-13	1.13E-12	
			BOUND *k* (m^2)	5.70E-13	1.00E-12	
1E	rcm4sept17f-hf	High *k* & porosity fracture zone	FRACK, FRACC *k* (m^2)	1.00E-07	1.00E-09	Slightly higher *T* and *Sg* around fracture zone, heat reaches slighly higher into Kaibab
			FRACK, FRACC porosity	0.7	0.8	
1F	rcm4sept17f-x	Anisotropic *k*	CSAND, WATBL *k* (m^2)	1.01E-10 (x-dir)	1.01E-11	Wider, shorter vapor transport zone. Water table raised.
			AQUIF *k* (m^2)	1.13E-11 (x-dir)	1.13E-12	
1G	rcm4sept17f-hp	High porosity of rock units	KLIME porosity	25%	15%	Decreased vapor formation within aquifer and condensation around fracture zone.
			CSAND, WATBL porosity	35%	25%	
			AQUIF, BOUND porosity	35%	25%	
1H	rcm4sept17f-lp	Low porosity of rock units	KLIME porosity	5%	15%	Higher *P*, *T*, and *Sg* throughout
			CSAND, WATBL porosity	15%	25%	
			AQUIF, BOUND porosity	15%	25%	
1J	rcm4sept17f2	Increased heat rate	Heat rate (J/s)	1.00E+06	5.50E+05	Similar result to base case setup in ~40% less time
1K	rcm4sept17f3	Decreased heat rate	Heat rate (J/s)	1.00E+05	5.50E+05	Lower *T* and *Sg* than base case even after 4x the amt of time
1L	rcm4sept17f-315	Higher water table	WATBL depth (m)	315	345	Increase in *P* & *T*, decrease in *Sg*; higher water table rise in center
1M	rcm4sept17f-lw	Lower water table	WATBL depth (m)	375	345	Decreases in *P* & *T*; smaller water table rise in center
1N	rcm4sept17f-df	Doubled fracture zone width	FRACK, FRACC width (m)	40	20	More vapor/ condensed water moved up more rapidly

Table 4: File names and descriptions for rapid heat injection simulations with parameter modifications. Figures in text or in Appendix C.

Water Table Depth

Adjusting water table depth shows similar results in the total amount of transported vapor and condensing water around the fracture zone. Relative to the base case at ~2.6 days, raising the water table by 30 m (Case 1L) produces minor increases in pressure and temperature, and very slight decreases in gas saturation (or increases in liquid saturation) in grid blocks reaching the ground surface (Fig. 20). Lowering the water table by 30 m (Case 1M) has a similarly minor effect on the grid blocks immediately surrounding the fracture zone, but produces a smaller "rise" in the water table over the heat injection. With the 315-m-deep water table, grid blocks of ~70% liquid saturation are driven up as high as 265 m, while the simulation with a 375-m-deep water table shows this high liquid saturation only reaching ~345 m depth.

Double Fracture Zone

Fracture zone width is doubled to 40 m in Case 1N, producing a simulation that runs for 2.1 days (Fig. 21). Increasing fracture-zone width produces a region of ~40-60% vapor, or ~60-40% liquid water, in the grid blocks located 20-40 m away from the fracture zone. In the base case, the fracture-zone-adjacent grid blocks generally maintain a vapor saturation of ~70% at this time step. Overall pressure is affected very little, while maximum temperature reaches over 400˚C within the fracture zone.

3.5.4. Slow Heat Injection

The slow heat injection models are set up with a dome-shaped heat source, or magma injection that reaches from the base of the model to the water table. In general, the heat injection for each model is 360 m wide at the bottom boundary and tapers to 60 m at the water table (Fig.

22). The heat source does not move and injection rate is continuous throughout the duration of each model.

3.5.4.1. Small Models at Standard Conditions

The small models with base-case initial conditions showing slow heat injection are named Case 2.1 and 2.2. These models are identical, with the exception of the center fracture-zone length: in Case 2.2, the fracture zone extends from the Kaibab-Coconino boundary to 425 m depth, and in Case 2.1, the fracture zone extends to this depth from the surface. Each model runs for ~4.4 days.

Pressure, temperature, and gas saturation (Fig. 23) show that fracture zone extent causes virtually no differences between the two setups. As in the rapid heat injection models, the highest pressure zones (>1.2×10^6 Pa) are focused around either side of the fracture zone within the aquifer. The center of the direct heat injection zone is primarily ~350-450˚C, with one block within the fracture zone at the depth of the original water table reaching ~500˚C. Gas saturation shows a zone of heated vapor in the center of the injection, with liquid water, some of which is barely heated above equilibrium temperature, being driven upward. On either side of the fracture zone at a depth of 290 m, grid blocks previously at residual saturation reach a liquid saturation of ~65%, and condensed water is present as far as 40 m away from the fracture zone. Vectors show strong vapor flow toward the surface through the fracture zone.

3.5.4.2. Large Model at Standard Conditions

The large model of slow heat injection at standard conditions (Case 2A) is set up with heat injection up to 530 m in a dome-like shape (Fig. 24), with the base of the injection set with a width of 600 m tapering upward to 200 m. Heat is injected at a constant rate in the entire dome

from the beginning to end of the simulation. The model runs to ~8.1 days before terminating due to convergence failure. The parameters at the final time step are plotted in Fig. 25. Pressure reaches a maximum of nearly 4.0×10^6 Pa within the central and lower heated regions, surrounded by a gradual pressure gradient up to the top of the saturated zone. Temperature within the injection region reaches nearly 500˚C. The gas saturation plot shows a result similar to that in the small model, but on a much larger scale. The water table, though initially 180 m above the injection zone, now has shifted upward. The peak in the center of the model corresponds to the location of the fracture zone. Grid blocks with as much as 50% liquid water are raised as high as 275 m depth, decreasing to <30% liquid by 245 m. At the farthest modeled extents of the 1200-m-wide system, blocks containing at least ~35% liquid are now located at 320 m depth. The heat injection region itself is entirely vapor at ~8.1 days, surrounded by a thin rim of two-phase liquid and vapor.

3.5.4.3. Sensitivity Analysis

The same parameter variations for sensitivity analyses applied to the rapid heat injection models were also applied to the stalled heat injection models. Models were run with high-permeability rock units (Case 2B), low-permeability rock units (Cases 2C and 2D), high-permeability and porosity fracture zone (Case 2E), anisotropic permeability rock units (Case 2F), high porosity (Case 2G), low porosity (Case 2H), high heat rate (Case 2J), low heat rate (Case 2K), a high water table (Case 2L), a low water table (Case 2M), doubled fracture-zone width (Case 2N), and no fracture zone (Case 2P). Models with significant variability from the base case are described below and summarized in Table 5. Pressure, temperature, and gas saturation plots for each of these models are presented in Appendix C.

Permeability and Porosity

As in the rapid heat injection models, permeability was increased for the Coconino Sandstone and saturated Supai Formation to 8.97×10^{-11} m^2. High permeability was tested using a model with a fracture zone that extends from the ground surface to a depth of 425 m (Case 2B), and conditions at 4.4 days and 5.6 days are shown in Fig. 26. At 4.4 days, a large tear-drop-shaped zone of vapor and associated condensed water is present within the Coconino Sandstone, affecting grid blocks as high as ~95 m depth. Just above the water table, the zone extends ~420-460 m wide. Most of the affected grid blocks contain less than ~75% vapor saturation, or greater than 25% liquid water saturation, and most of the model remains below 200˚C, with only a few blocks within the aquifer reaching temperatures >250˚C. At 5.6 days, the growing region of vapor and fluid extends into the base of the Kaibab Limestone, above 75 m depth, and extends ~400 m wide just above the water table. Most grid blocks remain around or below 200˚C, but the hottest blocks in the aquifer are heated to over 400˚C. A region of increased pressure grows corresponding with high T and S_g, though overall pressures remain relatively stable.

Lower permeabilities were tested in Cases 2C and 2D (Table 5). Permeabilities of the Coconino Sandstone and Supai Formation are lowest in Case 2C, calculated using the lower values of estimates of hydraulic conductivity of nearby wells. The simulation runs just under 4 days (Fig. 27). Similar to what is seen in the equivalent rapid heat injection simulation, heat and fluid flow are largely restricted to the fracture zone itself. However, vapor does form within the aquifer and a small area of rising saturation is seen around the fracture zone just above the water table. The temperature maximum exceeds 350˚C, and the highest pressures are more than an order of magnitude greater than under base case conditions. Water begins condensing around the fracture zone, but blocks do not exceed 50% liquid saturation above ~100 m depth.

Permeabilities for Coconino Sandstone and the Supai Formation in Case 2D are an average of the base case and 2C permeabilities. Results of this simulation at ~4 days vary little from the base case, but heat effects reach ~10 m higher within the fracture zone than in the base case (Fig. 27).

Fracture-zone permeability is increased to 1.0×10^7 m^2 and porosity to 80% in Case 2E. Compared to the base case model at ~2.3 days, introducing variability to fracture-zone properties shows very little impact on general aquifer conditions, but the fracture zone within the aquifer becomes almost entirely liquid-saturated. Heat and vapor now reach ~105 m depth in the fracture zone, compared to only ~235 m depth in the base case, and vapor extends into the fracture-zone-adjacent grid blocks up to ~115 m depth. All blocks above ~285 m maintain ~60% or more vapor saturation (Appendix C).

Anisotropic permeabilities for the Coconino Sandstone and Supai Formation were tested in Case 2F (Fig. 28). In this model, permeability for both units was increased by an order of magnitude in the x-direction. Compared to the base case at ~4.4 days, this simulation shows pronounced differences in fluid and vapor flow. With increased permeability in the x-direction, the zone of vapor formation and condensation is wider and shorter, only reaching a depth of ~125 m, increased permeability caused the entire water table to rise ~20 m. Heat effects within the aquifer are also extended laterally, and overall *P* and *T* are slightly lower.

Additional tests were run independently increasing and decreasing country-rock porosity (Cases 2G and 2H, respectively). An absolute 10% increase of porosity produces a similar result to the base case at 4.4 days with slight increases in all plotted parameters, while decreasing porosity has the opposite effect to a similar degree (Appendix C).

Slow Heat Injection Model Variation Tests						
Case	File Name	Description	Changed Variable	New Value	Base-Case Value	Observed Changes
2B	rcm8aug17b	High-*k* rock units	CSAND, WATBL *k* (m^2)	8.97E-11	1.01E-11	Much larger area of vaporization and condensation within country rock and surrounding fracture zone
			AQUIF *k* (m^2)	8.97E-11	1.13E-12	
2C	rcm4sept17h-mk	Low-*k* rock units	CSAND, WATBL *k* (m^2)	6.30E-14	1.01E-11	Heat and fluid flow largely restricted to fracture zone; Vapor forms in aquifer, and a small zone of rising saturation forms above the water table; Pressure up by nearly an order of magnitude
			AQUIF *k* (m^2)	1.80E-14	1.13E-12	
			BOUND *k* (m^2)	1.80E-14	1.00E-12	
2D	rcm4sept17h-ak	Moderately low *k* rock units	CSAND, WATBL *k* (m^2)	5.10E-12	1.01E-11	Very similar to base case, but heat effects higher by ~10 m in the fracture zone
			AQUIF *k* (m^2)	5.70E-13	1.13E-12	
			BOUND *k* (m^2)	5.70E-13	1.00E-12	
2E	rcm4sept17h-hf	High *k* & porosity fracture zone	FRACK, FRACC *k* (m^2)	1.00E-07	1.00E-09	Heat and vapor reach 120 m higher in the fracture zone than in the base case
			FRACK, FRACC porosity	0.7	0.8	
2F	rcm4sept17h-x	Anisotropic *k*	CSAND, WATBL *k* (m^2)	1.01E-10 (x-dir)	1.01E-11	Wider, shorter vapor transport zone. Water table raised in a broad area
			AQUIF *k* (m^2)	1.13E-11 (x-dir)	1.13E-12	
2G	rcm4sept17h-hp	High porosity of rock units	KLIME porosity	25%	15%	Slighly higher *P*, *T*, and *Sg*
			CSAND, WATBL porosity	35%	25%	
			AQUIF, BOUND porosity	35%	25%	
2H	rcm4sept17h-lp	Low porosity of rock units	KLIME porosity	5%	15%	Slightly lower *P*, *T*, and *Sg*
			CSAND, WATBL porosity	15%	25%	
			AQUIF, BOUND porosity	15%	25%	
2J	rcm4sept17h2	Increased heat rate	Heat rate (J/s)	1.00E+06	5.50E+05	Rapid vapor/fluid rise up to ~115 m in 2.3 days
2K	rcm4sept17h3	Decreased heat rate	Heat rate (J/s)	1.00E+05	5.50E+05	Lower *T* and *Sg* than base case, even after 4x the amt of time
2L	rcm4sept17h-315	Higher water table	WATBL depth (m)	315	345	Higher 2-phase plume, up to ~45 m
2M	rcm4sept17h-lw	Lower water table	WATBL depth (m)	375	345	Lower 2-phase plume, down to ~185 m
2N	rcm4sept17h-df	Doubled fracture-zone width	FRACK, FRACC width (m)	40	20	Large column of 2-phase fluid; condensation up to 75 m
2P	rcm4sept17i	No fracture zone	FRACK, FRACC width (m)	0	20	Water table bump up to ~265 m

Table 5: File names and descriptions for slow/ stalled heat injection simulations with parameter modifications. Figures in text or in Appendix C.

Heat Rate

Heat rate is increased in Case 2J to 1.0×10^6 J/s, and decreased in Case 2K to 1.0×10^5 J/s, as in the rapid heat injection models. Increasing heat rate produces a simulation that runs for ~2.3 days, and final parameters are shown alongside base case conditions at the same time step in Fig. 29. The region of grid blocks with increased pressure and temperature is much larger than in the base case model, but overall pressures are lower. Maximum temperatures are increased with a higher heat injection rate, with blocks of direct heat injection within the aquifer now exceeding 300˚C, and T_{max} up to 500˚C. The bump of saturated blocks above the initial water table depth in the center of the model occurs rapidly, with blocks of >80% liquid saturation up to 285 m depth. Grid blocks experiencing increased liquid saturation extend as high as 115 m depth.

The model using a decreased heat rate (Case 2K) creates virtually no change to the equilibrium conditions by ~4.4 days, with the exception of a very small zone of heated vapor forming within and around the fracture zone near the top of the aquifer. The model runs for a total of ~24 days, and by this time produces a large zone of vapor and fluid surrounding the fracture zone, reaching nearly 15 m from the surface (Fig. 30). Outside of this zone, the saturation bump above the water table is gradual, but extends to the edges of the model.

Water Table Depth

A higher and lower water table are modeled in Cases 2L and 2M, respectively. Conditions for the high, standard, and low water table models at ~4.0 days are shown in Fig. 31. In this sequence, depth to water shows a clear influence on the timing of vapor and liquid transport, as well as the volume that is moved upward in a short amount of time. With a higher

water table (315 m), the "plume" of vapor and liquid that is driven up reaches into the Kaibab Limestone to a depth of 45 m or less, and outside of this region, the bump of saturated blocks above the equilibrium water table reaches as high as 265 m. Base case water table depth (345 m) brings the plume down to a peak of ~95 m, and the bump down to ~285-295 m outside this region. Finally, the lowest tested water table (375 m) only brings the plume to ~185 m depth and the surrounding bump reaches only ~335 m. From the highest to lowest water table depths, P_{max} decreases by ~1.5-2.0 × 10^5 Pa with each model. Maximum T decreases with a deepening water table from ~500˚C to ~350˚C, but general temperatures throughout the setup appear to only decrease by ~25-40˚C between each model.

Double Fracture Zone

Fracture-zone width is doubled to 40 m in Case 2N, and parameters for this model at ~4.4 days are shown in Fig. 32. Doubling the size of the fracture zone has little effect on general pressure and temperature conditions, though T_{max} is dropped to below 400˚C. The largest impact of fracture-zone size is in volume and rate of vapor and liquid transport. In ~4.4 days, a column of two-phase fluid 120 m wide (including the fracture zone) reaches the Kaibab-Coconino boundary at 75 m, and a narrowing column continues into the Kaibab up to ~15 m depth. A total of 1,560 m^3 of liquid water is brought up above 205 m depth (in the two dimensional space). Allowing the simulation to continue to ~5.3 days shows a total of 1,780 m^3 of liquid water brought to this depth, or an additional 220 m^3 in less than a day.

No Fracture

Model Case 2P shows slow heat injection into a model with no fracture zone at all. After ~4.4 days, the injection has produced a pronounced bulge in the water table reaching at least 265 m depth. Groundwater in the region of the heat injection itself is completely vaporized, with a maximum temperature of ~375˚C and pressure exceeding 1.2×10^6 Pa. When the simulation is allowed to continue to ~5.3 days, little to no growth of the saturation dome is seen, but vapor continues to develop within the aquifer above the injection.

CHAPTER 4: DISCUSSION

4.1. Rapid vs Slow Heat Injection

The rapid-heat-injection scenarios are designed to show how water and vapor may move around a super-heated fracture zone, or conduit, during the earliest stages of an eruption. Magma rise is modeled using timed heat injection at high rates into the central high-permeability feature. If heat is injected all the way to the surface, the TOUGH2/EOS3 simulation terminates after a very short time as grid blocks dry out and the simulator has trouble converging. In order to overcome this convergence problem and make the simulator run further in time to show progressive phase changes and related fluid movement, the model was adjusted to only have heat injection up to 95 m depth. Note that TOUGH2 simulations are valid, coupled mass-conserved solutions for as long as the code converges to the specified convergence criterion. Although simulations for this study end with failures to converge at different end times, the outputs up to and at those end times are valid and useful for comparing behavior and understanding processes of water re-distribution relevant to magma intrusion.

The slow heat injection models are designed to demonstrate thermohydrologic processes that may occur with the presence of a hot magmatic body in an aquifer, particularly when the magma approaches and reaches the water table. The modeled water table in the SFVF is considered deep at ~345 m, but this is shallow in terms of total crustal depth. Most magma storage chambers are located between ~3-15 km depth, with some identified as shallow as ~2 km (Browne and Szramek, 2015). It is unlikely that a magma body at a shallow depth of <0.5 km under low lithostatic pressure would simply stall for a few days without cooling or erupting. It is therefore necessary when analyzing these non-erupting models to consider that the magma itself could be stalled much deeper than the maximum depth of this model domain, and that the rate of

heat injected into the modeled blocks could reflect heat from the magma reaching the shallow aquifer even if magma is much deeper. These models may also be informative about thermohydrologic processes at the water table and above during an eruption as magma itself travels to the surface. None of the associated geomechanical processes are modeled in these simulations; these processes would produce another set of changes in properties of the country rock-magma-hydrologic system and should be modeled in future studies.

Rapid-heat-injection models show that liquid water, driven upward as heated vapor, can quickly condense around the outside of a permeable fracture zone or potential magma conduit during an eruption. Using the base-case setup for Rattlesnake and Colton Craters, a zone of condensation reaches 40 to 60 m outside of the 20-m-wide conduit after only ~3 days, and a region of increased saturation surrounding the fracture zone reaches ~300 m depth, or 50 m above the equilibrium water table. As eruptions often last days to weeks, or even months, it is likely that these processes would continue at a similar rate to drive even greater quantities of water above 200 m depth. The models do not progress further in time due to drying out of grid blocks and related convergence limitations of the simulator used. Note that these grid blocks would be filled with magma in the actual system and therefore would not be subject to the "dry out" condition in an eruption as they are in the modeled system, but would, of course, be the subject of other dynamic thermo-hydro-mechanical processes.

Slow-moving or stalled magma simulations show similarities to the rapid heat injection models and are generally able to continue slightly further in time as fracture zone grid blocks are not dried out as quickly. After only 4-5 days, models with standard initial conditions show that significant quantities of vapor may be heated and driven upward, with or without the presence of a fracture zone, to shallower and cooler areas where the vapor is then able to condense. In the

equivalent large-scale models, a larger heat-injection area at greater depth in the subsurface produces a visible rise in the level of saturation above the equilibrium water table in just over 8 days, and increased liquid saturation is seen in blocks higher than ~250 m depth. As magma moves closer to the top of the aquifer in this model, saturation would presumably reach even higher.

These models are interpreted as providing one possible mechanism for large-scale fluid transport through the subsurface in areas with a deep water table. Given enough time, magma rising through the aquifer may drive significant quantities of water to shallow depths in the vapor phase, where it then condenses and can be temporarily held by capillary forces or within fractures and voids. When magma then rises quickly toward the surface and erupts, a potentially large quantity of liquid water may be available at shallow enough depth to produce a sustained, explosive phreatomagmatic eruption.

The two primary model setups showing rapid heat injection vs slow heat injection are not necessarily separate processes, and are likely both occurring in a single eruption. The slow injection setup may occur prior to the first magma reaching the surface, as described, or it could be an ongoing process that occurs simultaneously with magmatic eruption, with sill and dike intrusion in the shallow subsurface. While a narrow dike travels through a fracture or conduit to the surface, the larger rising or stalled magma body at depth can continue to transfer heat to the surrounding country rock and groundwater. The presented models show that, in many settings, this can lead to small- to large-scale vapor transport through the subsurface, where water may condense at cooler temperatures. At any time in an eruption, dikes may branch from the main conduit through pre-existing or newly opened fractures, where magma may then come into contact with this transported groundwater and induce MFCI.

The described thermohydrologic processes are not limited to the specific setup representing the SFVF. Models show these processes can occur in a range of settings and subsurface conditions, largely dependent on permeability, fracturing, and time. In general, it appears that the magmatic heat source must be present near the water table for at least a time of ~3 days to drive significant quantities of water toward the surface. In the rapid heat injection/ongoing eruption cases, this process is shown as occurring during the eruption and therefore a "pre-heating" of the subsurface, corresponding to a stalled magma body, is not considered a necessity. However, the large-scale stalled heat injection model shows that, given enough time (~8 days in fractured sandstone), a larger and deeper stalled magma body can drive a much greater quantity of water upward than is seen in the small models. Variations to the model setups are discussed in detail in the following section.

4.2. Model Variations

Several parameters, including country rock and fracture-zone permeability and porosity, water table depth, heat rate, and fracture-zone width, were adjusted in the models. Results of these sensitivity analyses provide insight into how different environments and subsurface conditions may affect these processes.

4.2.1. Country-rock permeability & porosity

Country-rock parameters for the base case models were chosen based on best estimates or calculations for the specific units beneath Colton and Rattlesnake Craters. Higher porosity allows heat and vapor to travel farther up toward the surface in the model, while decreasing porosity results in overall higher pressure and temperature, containing vapor and heat flow within a smaller area around the heat injection.

The calculated Coconino Sandstone permeability is notably high when compared to other published sandstone permeabilities (Bear, 1988), likely because of its significant fracturing in the study area. Permeability and porosity values were varied within the base-case model setups to determine how these parameters influence the observed thermal and hydrologic processes. The tested "low" permeability values for the Coconino Sandstone and Supai Formation (Cases 1C and 2C) were calculated using the lower values of hydraulic conductivity reported from nearby wells. The moderately low permeabilities for these units (Cases 1D and 2D) are the average between the standard and Cases 1C and 2C permeabilities. These low-end values are most comparable to moderately fractured or non-fractured sandstone. The tested higher-permeability values (Cases 1B and 2B) are most similar to a very fine, unconsolidated sand (Bear, 1988).

Country-rock permeability appears to be one of the most important factors in determining efficiency of the vaporization and water redistribution processes. Increasing permeability by less than an order of magnitude showed a noticeable effect on the area over which vapor is transported, producing a much larger "plume" of vapor and condensed liquid than base-case conditions (Figs. 15 and 26). Decreasing permeability does not produce a substantial vapor plume at all, but instead results in fluid flow dominantly becoming focused within the fracture zone, presumably resulting in significantly less liquid water being effectively redistributed to the shallow subsurface (Figs. 16 and 27).

For a slow-heating scenario, these models suggest that significant water vapor water can be driven toward the surface prior to or during eruption through a range of highly to moderately permeable and porous country rocks. The extent of the ascending vapor "plume" decreases with permeability and porosity, while the amount of time it takes for the plume to be driven upward is inversely related to these parameters. In highly permeable material like oil reservoir rocks or

unconsolidated sand and gravel, vapor-flow processes may be greatly increased throughout the matrix itself. In relatively low-permeability rocks such as fresh (unweathered) sandstone, limestone, or crystalline rocks, the matrix is likely a poor fluid transmitter. In regions of low-permeability country rock, the presence of a fracture zone or an otherwise high-permeability feature appears necessary to allow vapor and water to be driven toward the surface.

In all cases, the presence of fractures can be a major determining factor for volume and efficiency of fluid flow. In the rapid heat injection models, vapor appears to move through and condense around the fracture zone itself and within the higher-permeability and porosity country rocks. In these settings, these processes are assumed to continue within the country rock as the eruption progresses. Note that the "fracture zone" in these models is conceived as being the conduit for an eruption that is just beginning or that is ongoing; be it a pre-existing feature or an opening created by the dike injection itself, it is present in an eruption. Results show that, even in some regions with low-permeability and porosity country rock, heated vapor may still be driven upward (at least in the very early stages of an eruption) to possibly condense in cooler regions outside of the conduit.

The models do not account for the possibility of phase changes or formation of glassy "chilled margins" along the conduit walls, which could result in a nearly impermeable barrier between the magma and country rock (Tarff and Day, 2013). While these chilled margins would likely hinder continued condensation outside the conduit during the eruption, they could be an effective means for allowing liquid water to exist near the conduit. If the glassy margins are cooled quickly or if magma recedes, they can then fracture and allow any stored liquid water to reach the vent.

With onset of the very first explosions, permeability and porosity conditions in the subsurface will change significantly. Explosions occurring at any depth brecciate surrounding country rock, increasing its permeability and porosity. Processes of vapor and fluid transport would likely also increase in rate and extent as explosions continue.

4.2.2. Fracturing

Fracture-zone permeability was varied based on calculations from field fracture measurements. Calculated average permeabilities for measured fractures ranged from 10^{-5}- 10^{-7} m^2, using the parallel plate law as previously described. This calculation assumes surficial fracture aperture is representative for the entirety of its length, and that the fracture is completely open (no asperities) and free of sediment infilling. Field observation of these fractures showed that this is very rarely, if ever, the case. For this reason, a maximum permeability of 10^{-7} m^2 was tested for the fracture zone, though this is still considered to be unrealistically permeable. Porosity was increased to 80% to reflect this increased permeability and/or decreased fracture fill. When fracture permeability and porosity are increased, the rapid heat simulation only reaches ~1.2 days before some grid blocks are completely dried out, but results are not remarkably different from the base case at the same time step.

For simplicity, only a single, central fracture zone was defined in these models. In the base case, the fracture zone is 20 m wide in the x-direction and the model is 2D; however, the y-direction is still formally 1 m wide. The fracture zone is generally set up to extend from the top of the Kaibab Limestone to 425 m depth, within the Supai Formation. As described, fracture analysis of the Coconino Sandstone and Kaibab Limestone showed significant fracturing in both units, with larger, vertical fracture apertures typically on the cm-scale. The lateral extent of these

fractures was impossible to determine or even estimate, but regional mapping of faults and fractures in the area shows some large-scale features exceeding 20 m (Appendix A); regardless, the fracture zone in these models is intended to be representative of multiple smaller fractures. Determining vertical extent of fractures across the contacts between different units was also problematic, as exposures of Kaibab Limestone and Coconino Sandstone were viewed separately.

Various fracture-zone heights through and into the different units were tested with several models, but these did not show significant differences and were therefore not included for comparisons (e.g., Fig. 13). Fracture zone width was increased to 40 m in simulations for both heat-injection setups, producing notable results. The slow-heat-injection model with a 40-m-wide fracture zone shows more than 3× the amount of water brought above 205 m than in the base case, with vapor reaching as high as 15 m from the surface. These models highlight the significant effect of having fractures or some high-permeability feature(s) in the subsurface to increase vapor and fluid flow.

The fracture zone was also excluded altogether in a slow-heat-injection setup, showing an equally interesting result. Heat injection continued to produce vapor within the aquifer, driving up the surrounding liquid water and vapor to nearly 250 m depth by ~4.4 days. At the end of the simulation at ~5.3 days, the vapor-filled region had begun to grow upward, reducing liquid saturation in the overlying blocks. Though this model did show vapor and fluid movement toward the surface, continuation of the model likely would have produced a largely vapor-filled region in the overlying Coconino Sandstone.

4.2.3. Heat rate

Heat rate (J/s) has been calculated using a number of estimated or averaged variables, and therefore includes significant uncertainty. Heat rate from magma to country rock is also presumed to vary during eruption and between different rock types. The calculated "base-case" heat rate used herein is assumed to be relatively reasonable for these simplified models, but considering that magma injection is only described by this rate, this parameter is open to variation.

Increasing and decreasing heat rate by nearly half an order of magnitude produces similar results to the base case, but at much different rates. A lower heat rate, or what might be more representative of heat from depth, may take ~2 weeks or more to produce a result similar to what is seen in ~3-4 days at the base-case heat rate. Conversely, increasing the heat rate by the same magnitude brings about similar or nearly identical results to what is seen in the base-case models in ~1.5-2 fewer days. The models with a higher heat rate are probably most similar to actual direct heat from magma at very shallow depth immediately prior to eruption, while lower heat rates are likely most comparable to a magma body at depth.

4.2.4. Water-table depth

Depth to the water table was tested based on the ranges of estimated water-table depths for both Rattlesnake and Colton Craters (~315-375 m). Results of these simulations showed that the same vapor transport and condensation processes can still occur over a range of water-table depths, but over much different time scales. These processes are best observed in the slow heat injection models (Fig. 31). Raising the water table produces a larger plume of vapor and fluid transport in just 3.9 days than the base case model does in nearly 4.5 days, while vapor in the

lower water-table model only just starts to exceed 200 m depth after the same amount of time. Based on these results, areas with even deeper aquifers are likely to only experience sustained phreatomagmatic eruptions if a heat source is present for a long period of time, or if permeability and porosity are at least as high as the base case setup for modeling the SFVF. By contrast, these methods could provide another explanation for prolonged phreatomagmatic eruptions in areas with shallower aquifers.

4.3. Colton and Rattlesnake Craters: Eruptive Scenarios

4.3.1. Colton Crater

The eruption of Colton Crater was dominated by Strombolian activity, producing a large cinder cone. At some point late in the eruption, this dry eruptive activity was interrupted when magma encountered a source of liquid water, and the resulting large explosions blew away much of the existing cinder cone. The eruption then quickly dried out again following this activity, producing a small cinder cone inside the crater.

The source of the water and how it reached the magmatic vent remains uncertain. Evidence of northeastward vent migration is preserved in the deposits, suggesting that perhaps the vent intersected a water-filled fracture in the Kaibab or Coconino Formations. The phreatomagmatism was near the end of the eruption, so it is also possible that magma flux had begun to wane and allowed water in the country rock to flow toward the vent rather than driving it away as vapor during eruption. For either scenario, the water could have either been driven upward by the processes described in these models, or it could have been existing perched water in the Kaibab Limestone.

Thin-section analysis may provide clues to determining explosion depths, but interpretation is based on size and rounding of quartz grains and includes significant uncertainty. The sample from the lowest studied portion of the tuff deposit (CL) contains the highest percentage of quartz grains of the three samples, interpreted as primarily Coconino Sandstone. Thin section CM contains significantly less quartz in general, but grains are interpreted as primarily Coconino Sandstone with a minor amount of finer grains that may be from the Upper Supai Formation or the Kaibab Limestone. The uppermost section again appears to contain a high proportion of grains from the Coconino Sandstone and above, as well as a significant portion from the Supai Formation (including a single lithic fragment). These interpretations suggest that first explosions occurred in the Upper Coconino or higher and progressively deepened into the Supai Formation, but this interpreted increase in abundance of deeper grains in later deposits could also be a result of material recycling within the diatreme taking time to bring them up.

The rapid heat injection models are designed to be most representative of Colton Crater's eruption. In this model, heat is shown traveling through an existing conduit, imitating an ongoing eruption. Cutting off the heat injection at 95 m depth is not representative of realistic eruptive behavior, but was implemented to allow the simulation to continue further in time. The focus of the simulation is observing fluid motion and thermohydrologic processes beneath the surface; of less importance is the observation of magma reaching the surface without interaction with water. Therefore, we assume the "magma," or heat source, is continuing to the surface in these models.

Using standard parameters to represent the subsurface beneath Colton Crater, rapid heat injection models show water vaporizing and moving around the heat source in just over three days. Above the heat source, a bulge of liquid water is driven upward by vaporization,

mimicking the shape of the intrusion. Water also condenses around the conduit throughout "eruption." Heat within the aquifer vaporizes water, which then rises through the conduit or permeable country rock and condenses at some distance away from the heat source (in this case, only 10-20 m distant). Considering the abundance of fractures throughout the Coconino and Kaibab Formations, it stands to reason that even larger quantities of vapor and liquid water could be transported and stored at shallow depth than is seen in the idealized model scenarios.

If the models were continued further out in time with no changes to the setup, these processes would presumably continue to drive even greater quantities of water upward to shallow depths. The observed processes may therefore provide one possible mechanism for providing shallow liquid water for the Colton Crater eruption (Fig. 33). The limited volume of phreatomagmatic tephra present in the Colton Crater deposits suggests this period of activity likely did not involve a large quantity of liquid water, and it is also possible that pre-existing meteoric water was stored in fractures or voids within the Kaibab Limestone. If Colton Crater's phreatomagmatism happened coevally with vent migration, this could have led to magma intersecting with either source of water. If not concurrent with vent migration, phreatomagmatism may have occurred as a result of waning or stalled magma flux, or even descending magma, permitting water flow toward the vent. In either case, the interacting water could have been present in a perched aquifer prior to the eruption or it could have been driven up during the eruption. Rather than answering with any certainty the question of where the liquid water in the Colton Crater eruption came from, the models instead provide another possibility.

4.3.2. Rattlesnake Crater

The Rattlesnake Crater eruption appears to have started with a brief period of dry Strombolian activity, but little of the initial cinder cone remains. Most of the eruption involved repeated phreatomagmatic explosions over a period possibly lasting weeks to months, followed by another dry stage that built a small cinder cone on the southeastern crater rim. The crater and scoria cone sequence is elongated NW-SE, consistent with regional faulting.

The two analyzed sections from Rattlesnake Crater deposits are very similar. Both are interpreted as containing primarily quartz grains from the Coconino Sandstone and Kaibab Limestone, with smaller proportions of grains from the Upper Supai Formation. Calcite grains may be interpreted as Kaibab Limestone, but most of the calcite appears to be secondary precipitation. Of particular interest in each of these thin sections is the size of plagioclase and pyroxene crystals in juvenile clasts. In RL, these plagioclase and pyroxene phenocrysts are as large as 1.2 mm and 1.5 mm, respectively. These crystals could indicate a period of shallow magma residence prior to eruption.

Rattlesnake Crater's eruption might have begun similarly to either model scenario, or could have been more of a combination of the two. With the onset of a dry eruption, behavior was likely most similar to the rapid heat injection model with magma rising quickly to the surface and driving away water as steam, rather than interacting with it. The presence of magma below the water table for a prolonged period likely vaporized aquifer water, which moved toward the surface to condense at shallow depths around the conduit. When the eruption transitioned to phreatomagmatic activity after a short time, a significant quantity of water would have been emplaced in the shallow subsurface and available for sustained, efficient MFCI (Fig. 34).

It is impossible to know the sequence of these events, i.e., whether or not the water was being transported before or after first eruptive activity. It is plausible that the magma stalled at some depth before eruption and began the vapor-transport processes early on, but that magma found a fracture and a small volume quickly ascended without interacting with water to begin the dry eruption. A non-erupting crustal dike injection like this may not be unrealistic for the SFVF; analysis of a 2009 seismic swarm near Sunset Crater, for example, suggested possible mid- to lower crustal magma movement in this area (Brumbaugh et al., 2014). As magma continued heating the aquifer below during eruption, it could have driven greater and greater volumes of vapor and water upward to condense at shallower depths. Any branching dike or vent migration could have resulted in magma intruding into the now partially saturated Coconino Sandstone, producing MFCI and beginning the phreatomagmatic activity. Considering that the phreatomagmatic phase of the eruption continued for a long period of time, and thus required a large volume of shallow water, this seems to be the more likely sequence of events.

Data for the nearest well to Rattlesnake Crater was discovered late in the writing stage of this thesis. Based on these data, the water table beneath Rattlesnake is estimated to be ~315 m deep. The base-case groundwater depth of 345 m is therefore considered to be an upper limit for Rattlesnake Crater during its eruption, while the simulations using a “high” water table at 315 m (Cases 1L and 2L) are likely the most representative of actual conditions. As shown in these simulations, a higher water table produces more rapid and widespread vapor transport and condensation throughout the subsurface units. This could also help to explain how a seemingly larger amount of water was made available for this eruption as compared to Colton Crater.

As first explosions occurred, country rock would have been brecciated and mixed with juvenile material and condensed water. Repeated explosions created a diatreme and feeder dikes

probably deviated many times within the permeable diatreme fill, which led to repeated explosions from many locations within the diatreme. For a simplified demonstration of this process, the formation of the diatreme is modeled to a depth of 710 m, using a growing region of high permeability to demarcate the diatreme shape (Fig. 35). This is not considered representative of the entire diatreme beneath Rattlesnake Crater, as geophysical analysis indicates that it extends to at least 800 m and possibly as deep as ~3 km (Marshall et al., 2015).

The diatreme growth model does not progress very far in time, but shows that water and vapor can quickly move around the high-permeability diatreme structure. The first model (Case 3A) shows heat injection from the base of the large model up to 95 m depth within the fracture zone. The subsequent model includes a zone of high permeability in the center of the model up to the new saturation limit (Case 3B), representing a region of brecciated country rock where first explosions might have occurred, and the last step shows a large, high-permeability diatreme structure (Case 3C).

After just over 20 minutes in the final simulation, vapor and liquid water have begun to spread out to the walls of the diatreme and to the surface. With water quickly placed in many locations throughout the permeable diatreme fill, deviating dikes can continue to produce explosions and enlarge the structure. This model suggests that, once explosions begin, magmatic heat may then help perpetuate phreatomagmatic eruptions by driving large volumes of water vapor to shallow locations for strong explosions. Rather than explosions simply depleting the water source, they may help to increase the volume of available water by increasing rock permeability. This concept should be explored further; these models do not account for water physically moved around in explosions, nor do they model any geomechanical deformation or fracturing processes.

4.4. Application

The observed results of these modeled scenarios may help to explain different eruptive behaviors that have been recorded in eruptions around the world. As described, the process of vaporization and related upward transport and condensation could provide shallow water to phreatomagmatic eruptions in locations similar to the SFVF, where the water table is deep and well below the estimated ideal depth for tephra-producing explosions. Areas with moderately permeable and/or highly fractured country rock may be particularly susceptible to the development of phreatomagmatic activity where otherwise dry eruptions may be typical.

These processes are likely also at work in locations where the water table is not considered deep, and may be partly responsible for perpetuating eruptions that would otherwise "dry out" relatively quickly. Conceptual models of maar-diatreme formation often show a depleting water source or a cone of depression in the water table that forms within the diatreme as explosions continue to use up water (Lorenz, 1986). This scenario may occur in locations where country-rock permeability prevents rapid groundwater recharge to the diatreme. However, the TOUGH2 models show that movement of vapor and liquid water within and around the permeable diatreme, driven by the heat itself, could prevent rapid drying out by providing water to many locations throughout the subsurface (Fig. 36). If a "plume" of heated vapor is able to infiltrate the shallow subsurface, associated condensing water may become stored in pore spaces and fractures at shallow, cooler depths. As explosions occur and a high-permeability diatreme grows, vapor transport and condensation processes occur would much more rapidly and potentially throughout the entire permeable area. In this way, liquid water may then become stored in many locations within and surrounding the diatreme, where explosions can then occur with the rapid ascent and intrusion of intra-diatreme dikes. Upward movement of water within

the diatreme has often been attributed to debris jets and recycling of material with explosions, processes that certainly occur and likely provide some shallow water for explosions. The amount of water capable of being moved around via explosive transport is difficult to quantify and presumably somewhat small. The modeled processes appear to be capable of larger-scale liquid and vapor transport during and prior to eruption than would be expected by these methods, especially in situations where magma may reside at a shallow depth for days to weeks. In this way, phreatomagmatic explosions may be perpetuated for a longer period of time than would be possible if the water source simply dried out.

The models may also explain phenomena like what occurred in 1759 in the first few weeks of the El Jorullo eruption, where hot mud poured out of springs and hillsides as phreatic and phreatomagmatic explosions occurred at the vent (Gadow, 1930). In models with highly permeable subsurface material, the wide plume of vapor and water reaches shallow depths in just a few days even with a deep water table. If groundwater depth is ~100-200 m deep, this time could be reduced to less than a day—especially if water and vapor follow fractures and springs (Fig. 36). The mud flows at El Jorullo started at approximately the same time as explosions at the vent, suggesting that the presence of magma in the shallow subsurface even during eruption was enough to continue heating groundwater and driving it toward the surface; this behavior is essentially represented by a combination of the two primary model setups presented. Locations with a comparable subsurface to that below El Jorullo could likely experience similar hazards prior to or early on in an eruption. The occurrence of this type of phenomena could also provide clues about the size of the shallow magma source in an eruption

4.4.1. Limitations and further questions

The application of iTOUGH2/EOS3 (as a means of running the forward model TOUGH2/EOS3) in studying pre- and syn-eruptive processes of shallow volcanic systems is not common. The software is uniquely capable of providing detailed simulations of thermohydologic processes, but is not optimized to model the flow processes of heat and "dry" air; i.e., when grid blocks of the mesh are superheated to the point of losing all liquid and water vapor, the software often begins to converge poorly, resulting in very small time steps, and ultimately the simulation cannot continue further in time. This is a limiting factor in progressing eruption simulations far beyond the point of magma first reaching the surface or beyond the development of brecciated, high-permeability zones in the country rock as a result of MFCI explosions. Continuation of the models could be beneficial in understanding the situations at hand, but the models shown are considered to be informative in demonstrating possible scenarios for moving liquid water closer to the surface prior to eruption with the presence of a large heat source within the deep aquifer.

CHAPTER 5: CONCLUSIONS

A series of pre-eruptive and early eruption simulations created using TOUGH2/EOS3 shows two possible scenarios for producing phreatomagmatic activity at Colton Crater and Rattlesnake Crater in the SFVF of northern Arizona. Each volcano is underlain by fractured, permeable Permian sedimentary units, and the current water table at each is estimated to be ~315-380 m deep. This groundwater depth is far below the ideal depth of ≤100 m and the typical maximum depth of ~200 m for large, tephra-producing phreatomagmatic explosions. The water table is interpreted to have also been deep and close to the current level at the time of the eruptions.

Two-dimensional models produced using estimated country-rock parameters appropriate to the two study sites and a single 20-m-wide high-permeability fracture zone show that stalled or slow magma ascent prior to eruption can drive a significant quantity of water toward the ground surface as heated vapor, which then condenses to liquid water upon reaching cooler temperatures at shallower depths. In just over 4 days, an additional ~270 m^3 of liquid water is emplaced above a depth of 205 m in this two-dimensional scenario. This volume is specific to the 1-m-wide 2D system simulated here, and actual volumes of mobilized water in natural 3D systems could be 2-3 orders of magnitude larger. With liquid water placed in the shallow subsurface, rapidly ascending magma at the onset of eruption can initiate explosive MFCI to drive a phreatomagmatic eruption.

Rapid heat-injection models intended to imitate an initially dry eruption show that, immediately prior to and in the very early stages of an eruption, vapor can quickly be brought up and condense just outside the conduit. Any branching dike or vent migration could then initiate MFCI explosions. These model simulations terminate in ~3.3 days due to poor convergence of

the simulator, but these processes likely continue to occur and drive greater amounts of water toward the surface throughout an eruption.

In both modeled scenarios, increasing permeability, porosity, and/or fracture density can increase the rate at which these processes occur, as well as the total volume of transported fluid. A higher water table has the same effect, while a lower water table requires more time to produce similar results. Large-scale models with stalled heat injection in the bottom portion of the aquifer show that saturation can be driven up to ~250 m within only ~8 days; with subsequent magma ascent, this saturation would likely be driven even higher.

Rattlesnake Crater's eruptive activity may have been driven by a combination of the two model scenarios. Stalled magma at depth could have driven a large volume of liquid water into the shallow subsurface prior to eruption and/or simultaneously with the small-volume dry eruption. Slight vent migration or a branching dike could have then interacted with this shallow water, producing explosions. As repeated explosions continue to brecciate country rock and increase subsurface permeability, vapor and fluid transport processes likely continue to occur even more rapidly throughout the growing diatreme. Debris jets and recycling within the diatreme may also contribute to the continued supply of liquid water for MFCI. The eruption appears to have eventually dried out, possibly due to exhaustion of the water source or vent migration away from perched water.

The eruption of Colton Crater probably looked similar to the rapid heat injection scenarios. The eruption began with sustained Strombolian activity, interrupted by brief, late-stage phreatomagmatic explosions. Throughout the dry eruptive activity, vapor water could have been driven up nearer to the surface to condense outside of or away from the main conduit. Vent migration to the northeast may have resulted in MFCI if magma intersected this transported

liquid water, or explosions may have occurred as a result of decreased magma flux allowing water to flow toward the vent. The brief nature of this phreatomagmatic stage suggests that only a small amount of liquid water was available to interact with the magma in this location, and the eruption again dried out in its final stage.

The described models are not intended to conclusively describe the sequence of events for either the Rattlesnake or Colton Crater eruption, but to provide one possible mechanism for producing phreatomagmatic eruptions in areas with deep aquifers. Colton Crater's wet activity might have instead been driven by perched water already present in the shallow limestone, providing another set of possibilities for its eruption. Rattlesnake Crater's eruption could have also been partially driven by water from perched aquifers, or the water table could have been somewhat higher at the time of eruption than it is today (though a significant increase is not believed to be likely).

This study not only shows how maars may form in areas with initially deep water tables, but the same processes demonstrated in the models can also help explain how water is continually supplied to the upper diatreme in locations with relatively shallow groundwater, but where a cone of depression forms in the water table throughout an eruption. Rapid, large-scale vapor transport and condensation can also explain the voluminous outpouring of hot, muddy water that occurs with eruptions at some volcanoes. Future investigation of these processes in locations of interest could be bolstered by experiments, geophysical analysis of subsurface fracturing and structure, and/or detailed larger-scale modeling including geomechanical processes and potentially eruption processes.

REFERENCES

Ai, H. and Ahrens, T.J., 2004, Dynamic tensile strength of terrestrial rocks and application to impact cratering. Meteoritics and Planetary Science, Vol. 39, Issue 2, p. 233-246.

Arizona Department of Water Resources (ADWR), 1998-2017, GWSI-Groundwater Site Inventory. http://gisweb.azwater.gov/waterresourcedata/GWSI.aspx.

Auer, A., Martin, U., and Németh, K., 2007, The Fekete-hegy (Balaton Highland Hungary) "soft-substrate" and "hard-substrate" maar volcanoes in an aligned volcanic complex—Implications for vent geometry, subsurface stratigraphy and the palaeoenvironmental setting. Journal of Volcanology and Geothermal Research, Vol. 159, p. 225-245.

Bear, J., 1988, *Dynamics of Fluids in Porous Media*. New York: Dover, p. 136.

Bills, D. J. and Flynn, M. E., 2002, Hydrogeologic data for the Coconino Plateau and adjacent areas, Coconino and Yavapai Counties, Arizona. U.S. Geological Survey Open-File Report 02-265, 38 p.

Bills, D. J., Flynn, M. E., and Monroe, S. A., 2016, Hydrogeology of the Coconino Plateau and Adjacent Areas, Coconino and Yavapai Counties, Arizona. U.S. Geological Survey Scientific Investigations Report 2005-5222, Version 1.1, 103 p.

Bills, D. J., Truini, M., Flynn, M.E., Pierce, H. A., Catchings, R. D., and Rymer, M. J., 2000, Hydrogeology of the Regional Aquifer near Flagstaff, Arizona, 1994-97. U.S. Geological Survey Water Resources Investigations Report 00-4122, 142 p.

Blaikie, T. N., Ailleres, L., Betts, P. G., and Cas, R. A. F., 2014, A geophysical comparison of the diatremes of simple and complex maar volcanoes, Newer Volcanics Province, south-eastern Australia. Journal of Volcanology and Geothermal Research, Vol. 276, p. 64-81.

Bralower, T. and Bice, D., (n.d.), Heat Capacity and Energy Storage, Earth 103: Earth in the Future, College of Earth and Mineral Science, The Pennsylvania State University. https://www.e-education.psu.edu/earth103/node/1005.

Browne, B. and Szramek, L., 2015, Rates of magma ascent and storage in Sigurdsson, H., ed., *Encyclopedia of Volcanoes (2nd Edition),* Academic Press, p. 203-214.

Brumbaugh, D.S., Hodge, B.E., Linville, L., and Cohen, A., 2014, Analysis of the 2009 earthquake swarm near Sunset Crater volcano, Arizona. Journal of Volcanology and Geothermal Research, Vol. 285, p. 18-28.

Carey, R. J., Houghton, B. F., and Thordarson, T., 2009, Abrupt shifts between wet and dry phases of the 1875 eruption of Askja Volcano: Microscopic evidence for macroscopic dynamics. Journal of Volcanology and Geothermal Research, Vol. 184, p. 256-270.

Carrasco-Núñez, G., Ort, M. H., and Romero, C., 2007, Evolution and hydrological conditions of a maar volcano (Atexcac crater, Eastern Mexico). Journal of Volcanology and Geothermal Research, Vol. 159, p. 179-197.

Colton, H.S., 1936, 1967, The basaltic cinder cones and lava flows of the San Francisco Mountain Volcanic Field. Northern Arizona Society of Science & Art, Inc.; First Edition, Bulletin No. 10, 1936; Revised Edition, 1967, 58 p.

Crossey, L. J., Fischer, T. P., Patchett, P. J., Karlstrom, K. E., Hilton, D. R., Newell, D. L., Huntoon, P., Reynolds, A. C., and de Leeuw, G. A. M., 2006, Dissected hydrologic systems at the Grand Canyon: Interaction between deeply derived fluids and plateau aquifer waters in modern spirings and travertine. Geology, Vol. 34, No. 1, p. 25-28.

Cummings, D., 1972, Mafic and ultramafic inclusions, Crater 160, San Francisco Volcanic Field, Arizona. Geological Survey Research 1972, USGS Professional Paper 800-B, p. B95-B104.

De Silva, S. and Lindsay, J. M., 2015, Primary volcanic landforms in Sigurdsson, H., ed., *Encyclopedia of Volcanoes (2nd Edition),* Academic Press, p. 273-297.

Eppelbaum, L.V., Kutasov, I., and Pilchin, A.N., 2014, Thermal properties of rocks and density of fluids. in *Applied Geothermics*, Lecture Notes in Earth System Sciences. Springer-Verlag Berlin Heidelberg, p. 99-149.

Finsterle, S., 2007, iTOUGH2 User's Guide. Lawrence Berkeley National Laboratory Report LBNL-40040, Updated Reprint, 130 p.

Gadow, H., 1930, *Jorullo: The history of the volcano of Jorullo and the reclamation of the devastated district of animals and plants*. Cambridge University Press, 101 p.

Hoffman, J. P., Bills, D. J., Phillips, J. V., and Halford, K. J., 2006, Geologic, hydrologic, and chemical data from the C aquifer near Leupp, Arizona: U.S. Geological Survey Scientific Investigations Report 2005-5280, 42 p.

Holm, R. F., 2001, Cenozoic paleogeography of the central Mogollon Rim-southern Colorado Platea region, Arizona, revealed by Tertiary gravel deposits, Oligocene to Pleistocene lava flows, and incised streams. GSA Bulletin, Vol. 113, No. 11, p. 1467-1485.

Hooten, J. A. and Ort, M. H., 2002, Peperite as a record of early-state phreatomagmatic fragmentation processes: an example from the Hopi Buttes volcanic field, Navajo Nation, Arizona, USA. Journal of Volcanology and Geothermal Research, Vol. 114, p. 95-106.

Hurwitz, S., Kipp, K., Ingebritsen, S. E., and Reid, M. E., 2003, Groundwater flow, heat transport, and water table position within volcanic edifices: Implications for volcanic processes in the Cascade Range. Journal of Geophysical Research, Vol. 108, No. B12, 2557, p. 1-19.

Leudemann, L., Ort, M. H., and Witter, M., 2013, Transition from strombolian to phreatomagmatic activity due to scoria cone vent migration: Colton Crater, San Francisco Volcanic Field, northern Arizona. Abstracts with Programs - Geological Society of America, Vol. 45, Issue 7, pp.336.

Lorenz, V., 1986, On the growth of maars and diatremes and its relevance to the formation of tuff rings. Bulletin of Volcanology, Vol. 48, p. 265-274.

Lorenz, V., 2003, Maar-diatreme volcanoes, their formation, and their setting in hard-rock or soft-rock environments. GeoLines, Vol. 15, p. 72-83.

Luhr, J.F., Simkin, T., and Cuasay, M., 1993: Paricutin: The Volcano Born in a Mexican Cornfield. U.S. Geoscience Press, 427 p.

Lupi, M., Geiger, S., Carey, R. J., Thordarson, T., and Houghton, B. F., 2011, A model for syn-eruptive groundwater flow during the phreatoplinian phase of the 28-29 March 1875 Askja volcano eruption, Iceland. Journal of Volcanology and Geothermal Research, Vol. 203, p. 146-157.

Magnusdottir, L. and Finsterle, S., 2015, iTOUGH2-EOS1sc: Multiphase reservoir simulator for water under sub- and supercritical conditions user's guide. Lawrence Berkeley National Laboratory Report LBNL-7017E, 17 p.

Magnusdottir, L. and Finsterle, S., 2015, An iTOUGH2 equation-of-state module for modeling supercritical conditions in geothermal reservoirs. Geothermics, Vol. 57, p. 8-17.

Manger, E., 1963, Porosity and bulk density of sedimentary rocks. Contributions to Geochemistry, Geological Survey Bulletin 1144-E, 55 p.

Marshall, A., Connor, C., Kruse, S., Malservisi, R., Richardson, J., Courtland, L., Connor, L., Wilson, J., and Karegar, M. A., 2015, Subsurface structure of a maar-diatreme and associated tuff ring from a high-resolution geophysical survey, Rattlesnake Crater, Arizona. Journal of Volcanology and Geothermal Research, Vol. 304, p. 253-264.

Matthai, S. K. and Belayneh, M., 2004, Fluid flow partitioning between fractures and a permeable rock matrix. Geophysical Research Letters, Vol. 31, L07602, p. 1-5.

McClintock, M. and White, J. D. L., 2006, Large phreatomagmatic vent complex at Coombs Hills, Antarctica: Wet, explosive initiation of flood basalt volcanism in the Ferrar-Karoo LIP. Bulletin of Volcanology, Vol. 68, p. 215-239.

McGuinness, M. J., Blakeley, M., Pruess, K., and O'Sullivan, M. J., 1993, Geothermal heat pipe stability: Solution selection by upstreaming and boundary conditions. Transport in Porous Media 11, p. 71-100.

Moore, R. B. and White, E. W., 1987, Geologic map of the east part of the San Francisco Volcanic Field, north-central Arizona, Map MF-1960.

Morrissey, M., Zimanowski, B., Wohletz, K., and Büttner, R., 2000, Phreatomagmatic fragmentation in Sigurdsson, H., ed., *Encyclopedia of Volcanoes (1st Edition),* Academic Press, p. 431-445.

Ort, M. H. and Carrasco-Núñez, G., 2009: Lateral vent migration during phreatomagmatic and magmatic eruptions at Tecuitlapa Maar, east-central Mexico. Journal of Volcanology and Geothermal Research, Vol. 181, p. 67-77.

Pruess, K., Oldenburg, C. and Moridis, G., 2011. TOUGH2 User's Guide, Version 2.1, LBNL-43134 (revised). *Lawrence Berkeley National Laboratory, Berkeley, CA*.

Ross, P.-S., Delpit, S., Haller, M. J., Nemeth, K., and Corbella, H., 2010, Influence of the substrate on maar-diatreme volcanoes—An example of a mixed setting from the Pali Aike volcanic field, Argentina. Journal of Volcanology and Geothermal Research, Vol. 201, p. 253-271.

Ross, P.-S., White, J. D. L., Zimanowski, B., and Buttner, R., 2008, Multiphase flow above explosion sites in debris-filled volcanic vents: Insights from analogue experiments. Journal of Volcanology and Geothermal Research, Vol. 178, p. 104-112.

Scott, S., Driesner, T., and Weis, P., 2015, Geologic controls on supercritical geothermal resources above magmatic intrusions. Nature Communications, Vol. 6, p. 1-6.

Schwoerer, A. J., 2014, Eruptive history of Rattlesnake Crater, Arizona, San Francisco Volcanic Field REU. Abstracts with programs- Geological Society of America, Vol. 46 (6), p. 550.

Southwest Ground-water Consultants, Inc. (SGC), 2015, Red Gap Ranch-Leupp water resources environmental assessment groundwater flow model. Prepared for City of Flagstaff Utilities Division, 153 p.

Sweeney, M. R. and Valentine, G. A., 2015, Transport and mixing dynamics from explosions in debris-filled volcanic conduits: Numerical results and implications for maar-diatreme volcanoes. Earth and Planetary Science Letters, Vol. 425, p. 64-76.

Tanaka, K. L., Shoemaker, E. M., Ulrich, G. E., and Wolfe, E. W., 1986, Migration of volcanism in the San Francisco volcanic field, Arizona. Geological Society of America Bulletin, v. 97, p. 129-141.

Tarff, R. W. and Day, S.J., 2013, Chilled margin fragmentation as a trigger for transition from Strombolian to phreatomagmatic explosive activity at Cova de Paul Crater, Santo Antao, Cape Verde Islands. Bulletin of Volcanology, 75:735, 14 p.

Udell, K. S., 1985, Heat transfer in porous media considering phase change and capillarity—the heat pipe effect. International Journal of Heat and Mass Transfer, Vol. 28, p. 485-495.

Ulrich, G. E., and Bailey, N.G., 1987, Geologic map of the SP Mountain part of the San Francisco volcanic field, north-central Arizona, No. 1956.

Valentine, G. A., Graettinger, A. H., and Sonder, I., 2014, Explosion depths for phreatomagmatic eruptions. Geophysical Research Letters, Vol. 41, p. 3045-3051.

Valentine, G. and White, J. D. L., 2012, Revised conceptual model for maar-diatremes: Subsurface processes, energetics, and eruptive products. Geology, online, www.gsapubs.org, doi:10.1130/G33411.1.

Valentine, G. A., 2012, Shallow plumbing systems for small-volume basaltic volcanoes, 2: Evidence from crustal xenoliths at scoria cones and maars. Journal of Volcanology and Geothermal Research, Vol. 223-224, p. 47-63.

Van Kooten, G. K. and Buseck, P. R., 1978, Interpretation of olivine zoning: Study of a maar from the San Francisco volcanic field, Arizona. Geological Society of America Bulletin, Vol. 89, p. 744-754.

Watkins, H., Bond, C. E., Healy, D., and Butler, R. W. H., 2015, Appraisal of fracture sampling methods and a new workflow to characterise heterogeneous fracture networks at outcrop. Journal of Structural Geology, v. 72, p. 67-82.

White, J. D. L., 1996, Impure coolants and interaction dynamics of phreatomagmatic eruptions. Journal of Volcanology and Geothermal Research, Vol. 74, p. 155-170.

White, J. D. L. and McClintock, M. K., 2001, Immense vent complex marks flood-basalt eruption in a wet, failed rift: Coombs Hills, Antarctica. Geology, Vol. 29, No. 10, p. 935-938.

White, J. D. L. and Ross, P.–S., 2011, Maar-diatreme volcanoes: A review. Journal of Volcanology and Geothermal Research, Vol. 201, p. 1-29.

Wohletz, K. H., 1986, Explosive magma-water interactions: Thermodynamics, explosion mechanisms, and field studies. Bulletin of Volcanology, Vol. 48, p. 245-264.

Zimanowski, B., Büttner, R., Dellino, P., White, J. D. L., and Wohletz, K. H., 2015, Magma-water interaction and phreatomagmatic fragmentation. in Sigurdsson, H., ed., *Encyclopedia of Volcanoes (2nd Edition),* Academic Press, p. 473-484.

FIGURES

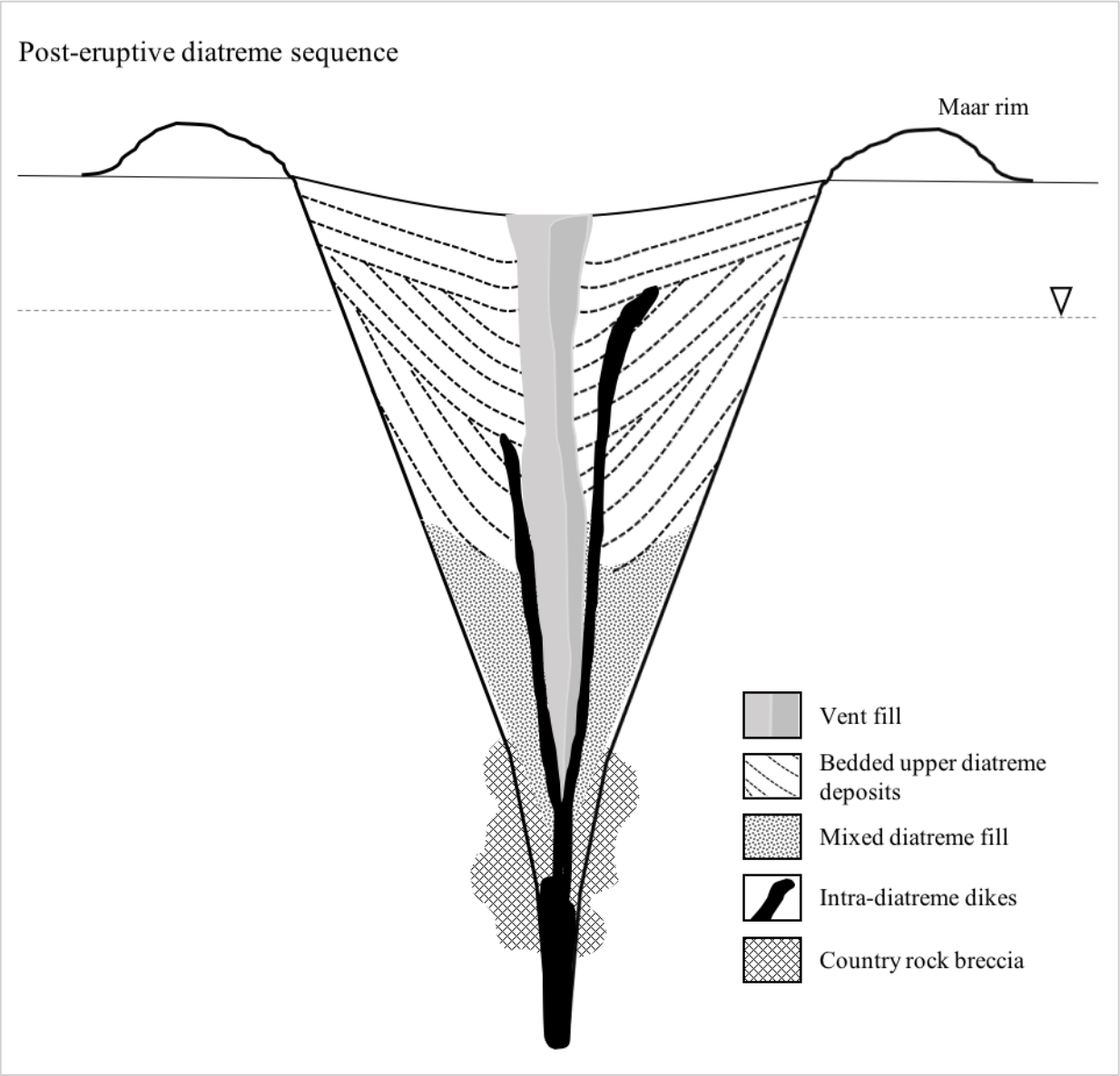

Figure 1: Schematic diagram of common post-eruptive diatreme sequence. Poorly-sorted diatreme fill consisting of country rock, pyroclastic deposits, and magma fills much of the diatreme, possibly overlain by bedded, slumped pyroclastic deposits in the upper diatreme. Deeper explosions brecciate country rock around the base of the diatreme.

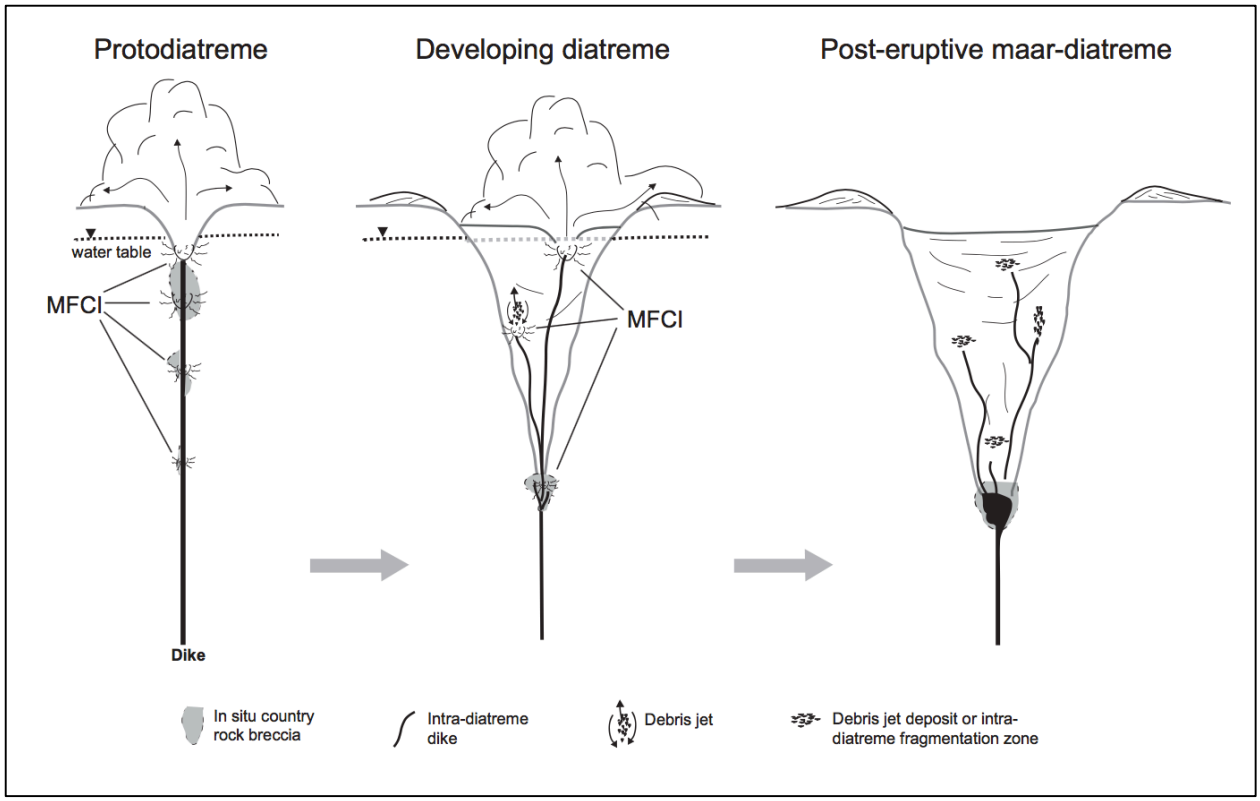

Figure 2: Modern conceptual model of maar-diatreme formation from Valentine and White (2012). Explosions may occur at any depth below the critical pressure of water, though shallower explosions are generally most efficient. The water table is probably maintained at a constant level throughout eruption, but debris jets and upward recycling within the diatreme may also assist in moving water through diatreme fill. MFCI = molten fuel-coolant interaction.

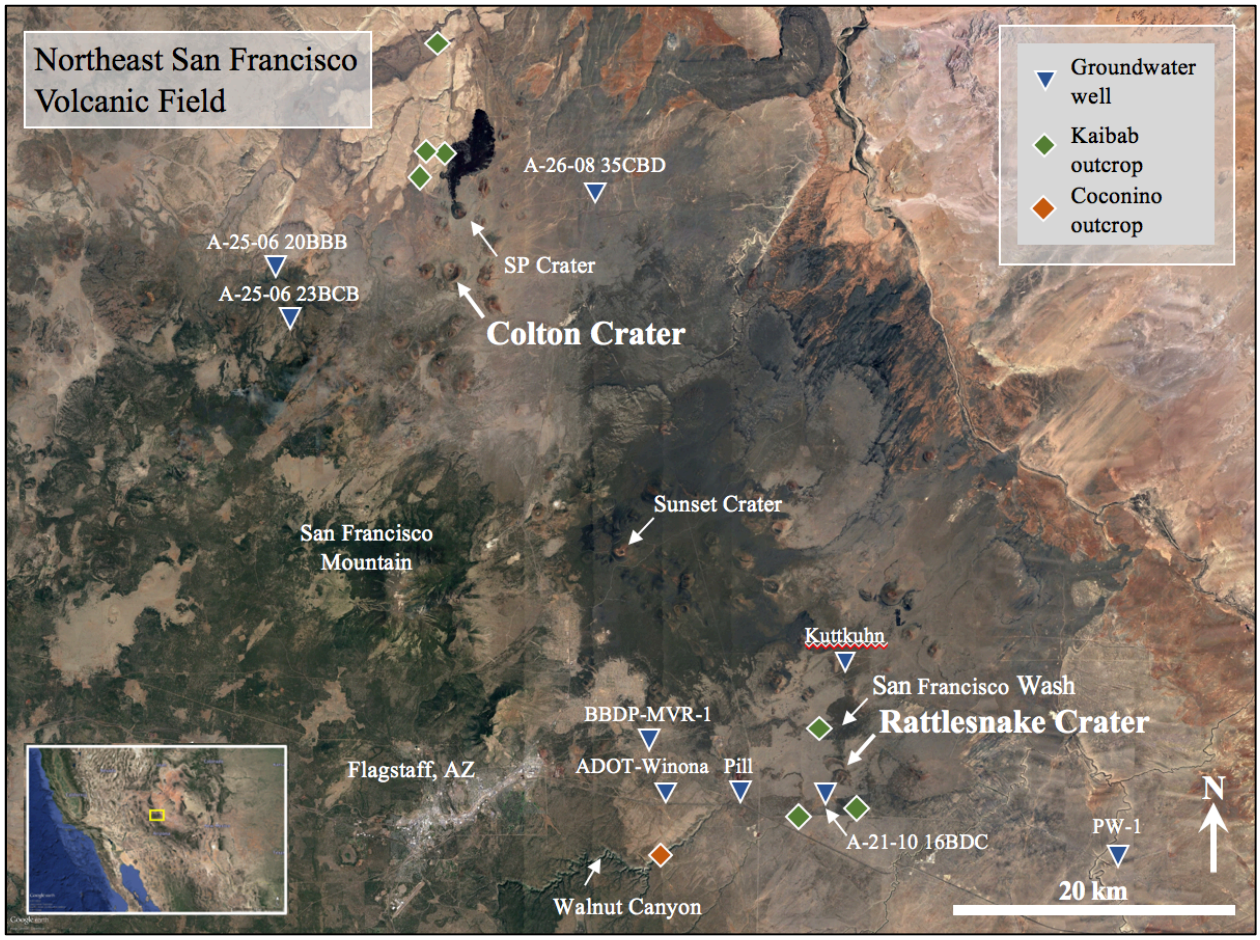

Figure 3: Study area map showing the locations of Colton Crater and Rattlesnake Crater within the northeastern San Francisco Volcanic Field, northern Arizona. Locations of Kaibab Limestone and Coconino Sandstone outcrops where fracture measurements were taken are also identified, as well as locations of nearby wells. Image: Google Earth.

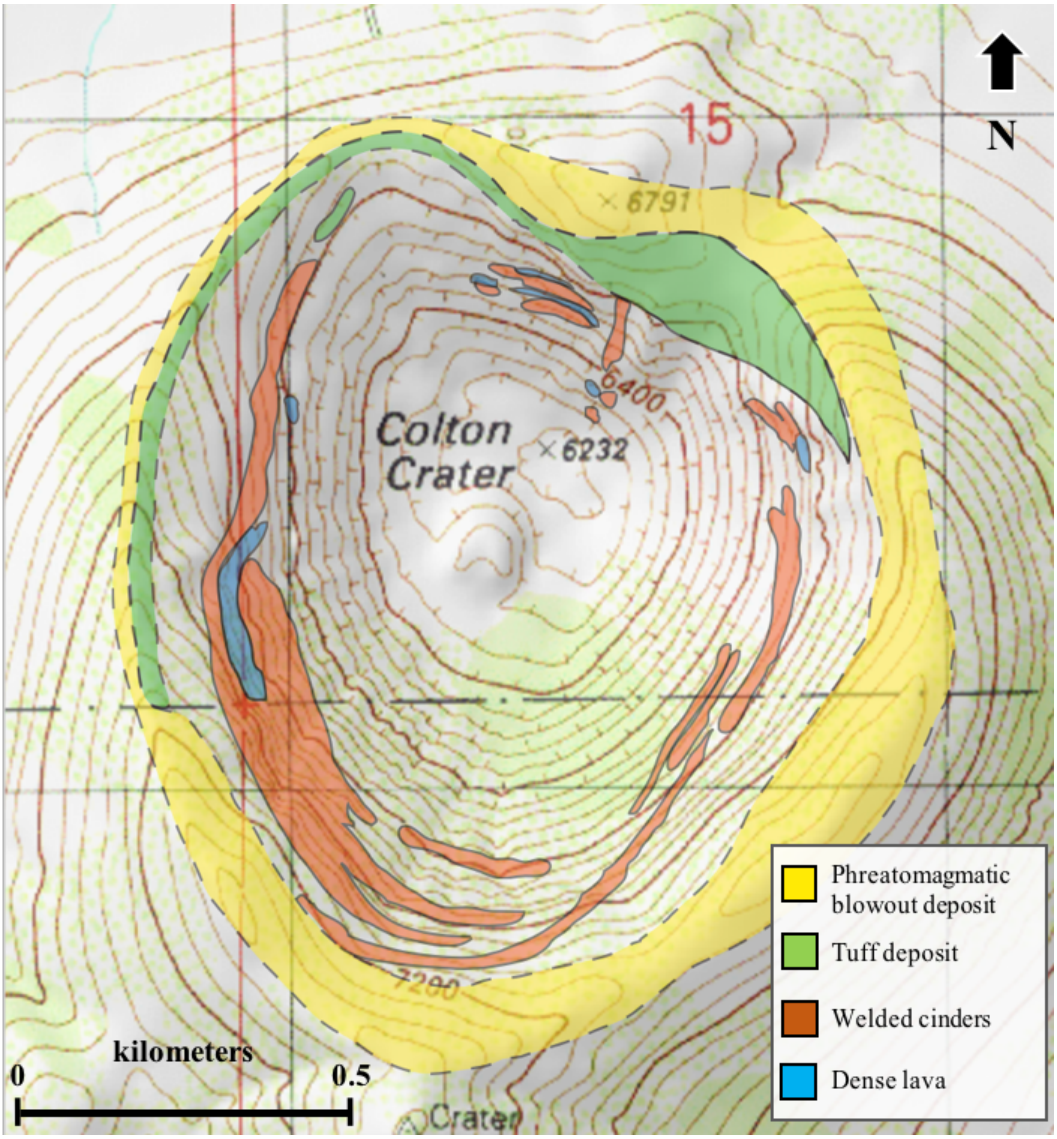

Figure 4: Partial geologic map of Colton Crater, modified from Leudemann et al. (2013).

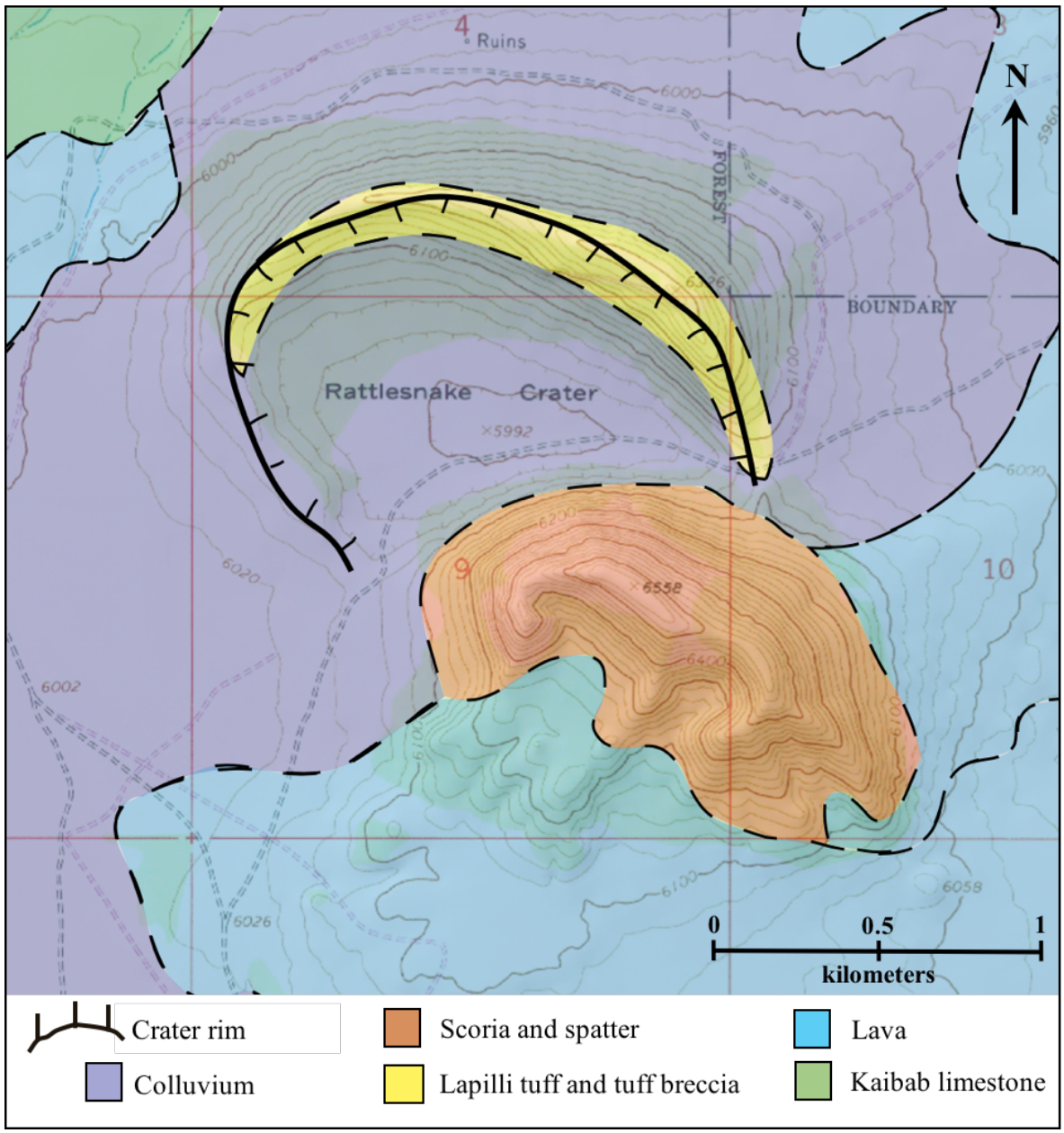

Figure 5: Partial geologic map of Rattlesnake Crater, modified from Valentine et al. (2012).

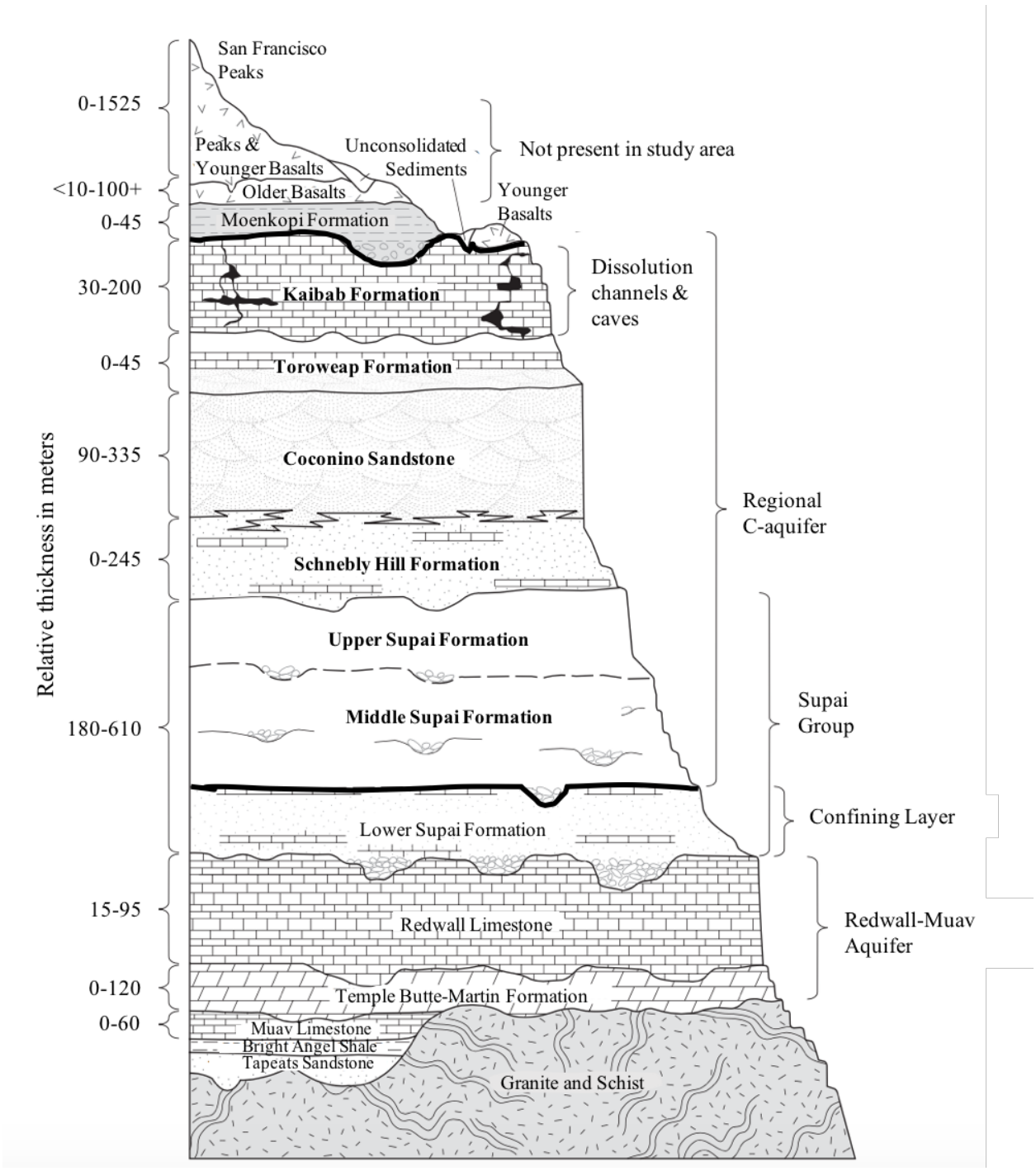

Figure 6A: Generalized stratigraphic section of the Flagstaff, AZ area. Bold lines mark the upper- and lowermost boundaries of the models of Rattlesnake and Colton Craters. Figure modified from Bills et al. (2000).

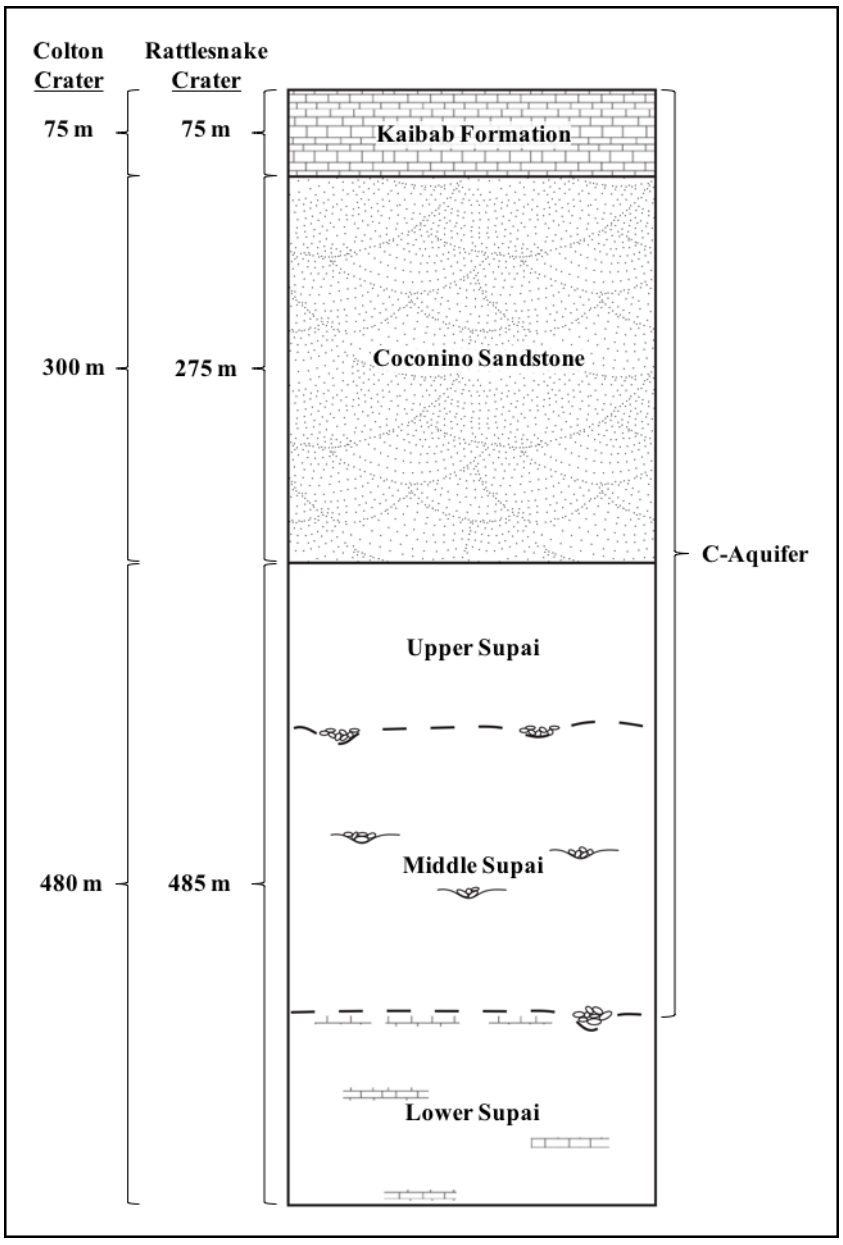

Figure 6B: Stratigraphic section showing estimated thicknesses of the units of the C-Aquifer beneath Colton and Rattlesnake Craters.

Figure 7: Wooden tool measuring 1 m^2 constructed for fracture analysis, pictured against an outcrop of Kaibab Limestone. All fractures within the square were measured.

Figure 8: Field sites for fracture measurements. (A) San Francisco Wash, north wall; (B) Farthest north study site, near Colton Crater; (C) San Francisco Wash, south wall; (D) Inner graben north of Colton Crater.

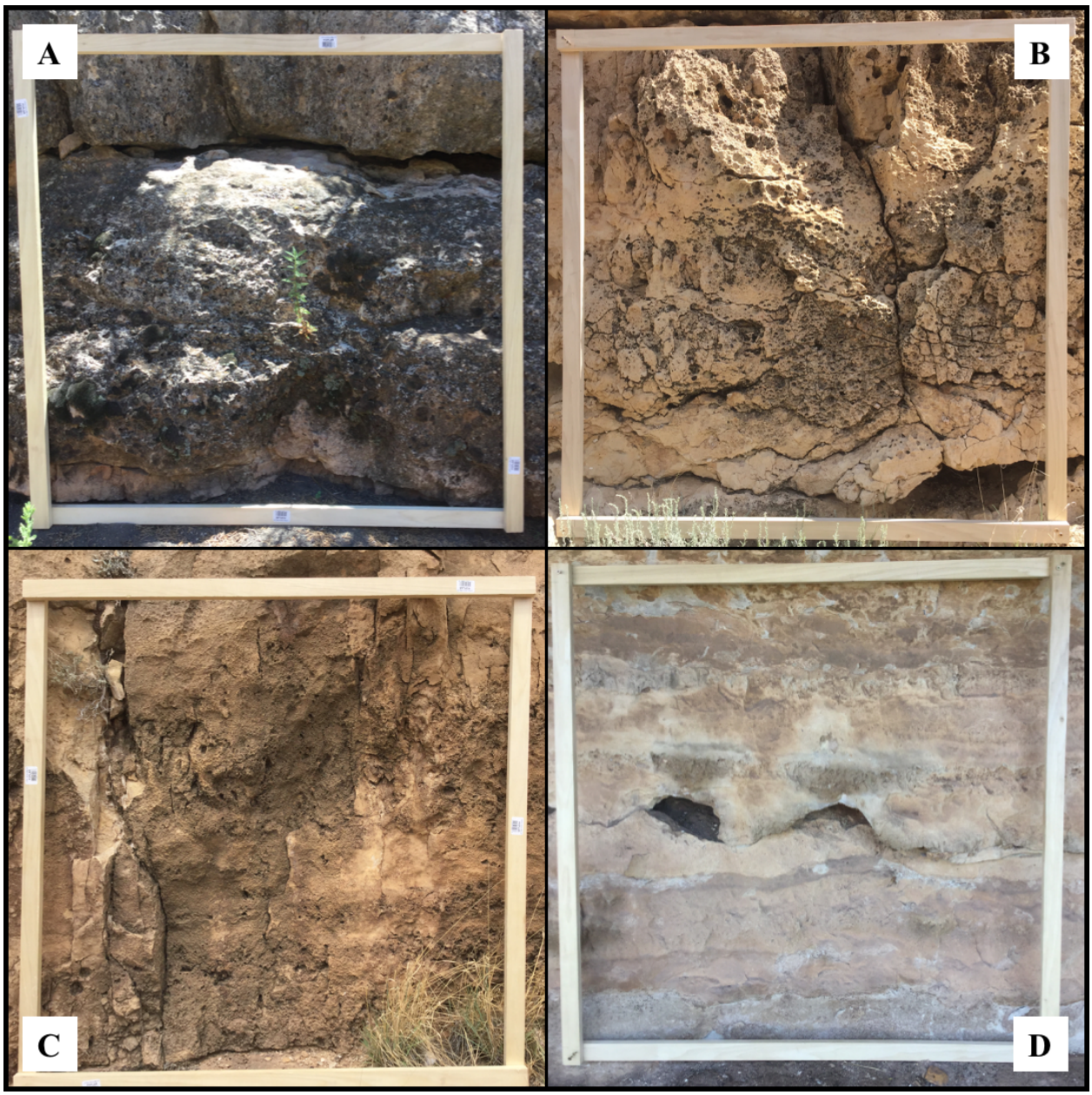

Figure 9: Selected fracture measurement outcrops showing variability within the Kaibab Formation. Some sites are dominated by small-scale fractures and dissolution features, while others primarily contain larger fractures and partially open bedding planes. (A) Site RK10 in a shallow wash SSE of Rattlesnake Crater; (B) Site RK1, the uppermost studied section on the south side of San Francisco Wash; (C) Site CK3 at the far north end of the graben north of Colton Crater; (D) Site RK8 on the south wall of San Francisco Wash. Voids are common within the formation.

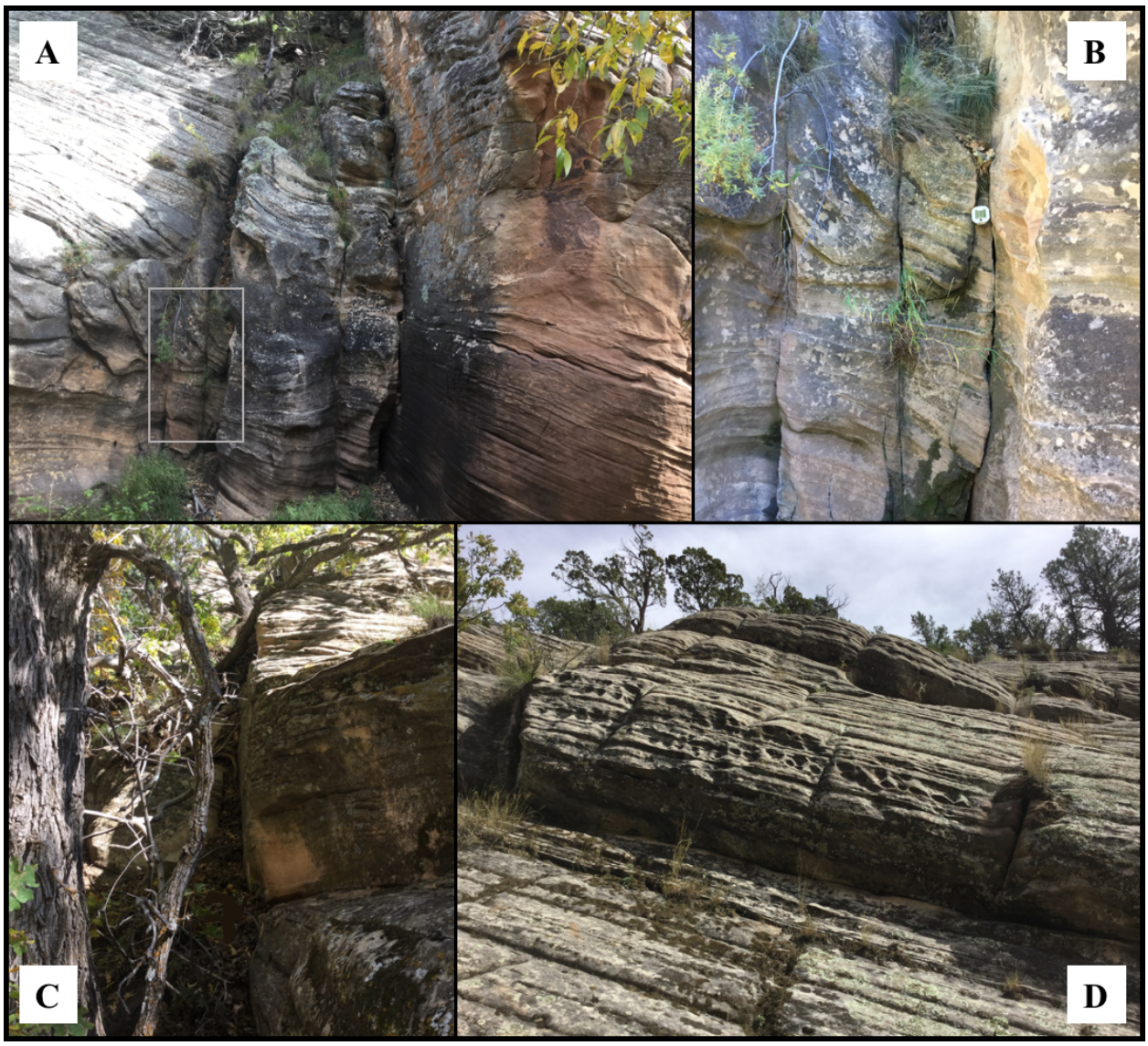

Figure 10: Field photographs of Coconino Sandstone in Walnut Canyon. (A) Section containing large-scale vertical fractures; (B) Closer view of the left-most vertical fractures in A (outlined), Brunton compass for scale; (C) View of a large-scale vertical fault; (D) Uppermost studied section of Coconino. Some subhorizontal bedding planes may be sufficiently open to serve as fluid conduits.

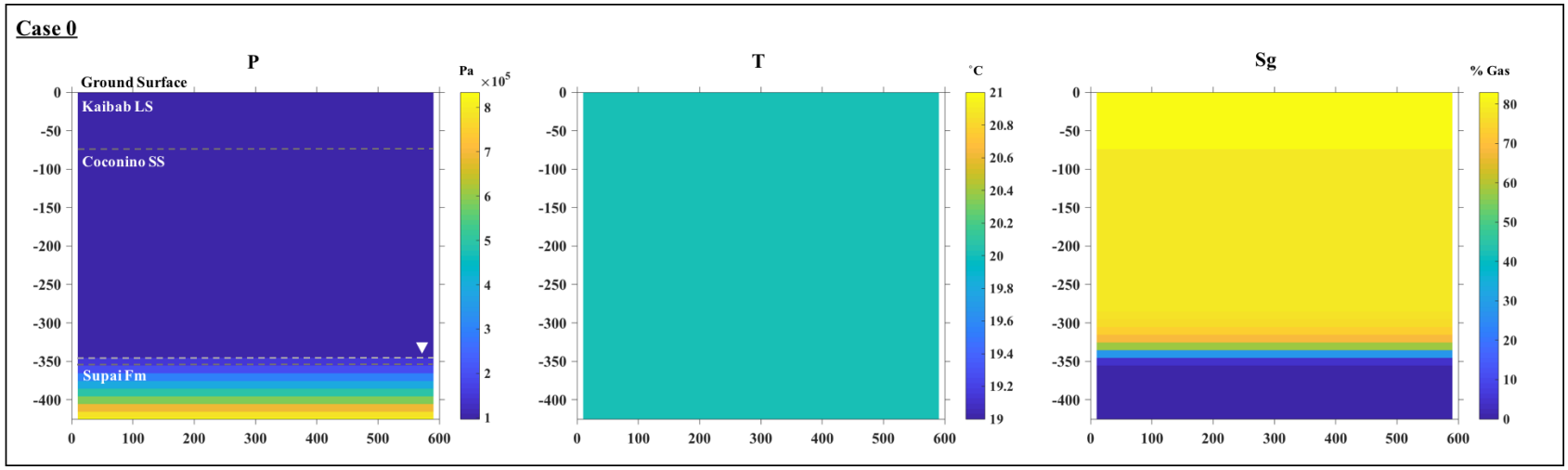

Figure 11: Equilibrium pressure, temperature, and gas saturation in the subsurface prior to any fracture input or heat injection (Case 0).

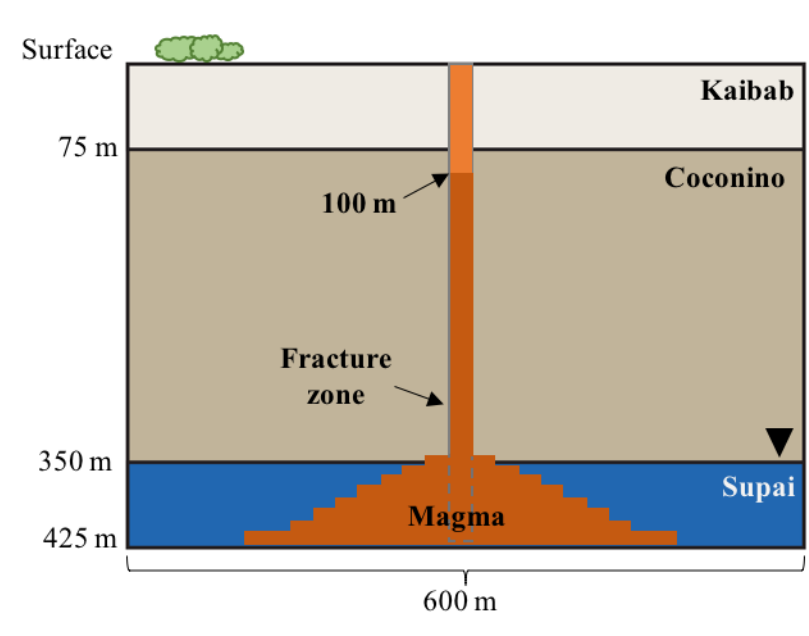

Figure 12: Schematic diagram showing the setup for rapid timed heat injection. The magma at the base is approximately 360 m wide, tapering up to 60 m wide at the water table, and 20 m wide within the fracture. In most models, heat injection is terminated at 100 m depth, though some extend to the surface (light orange).

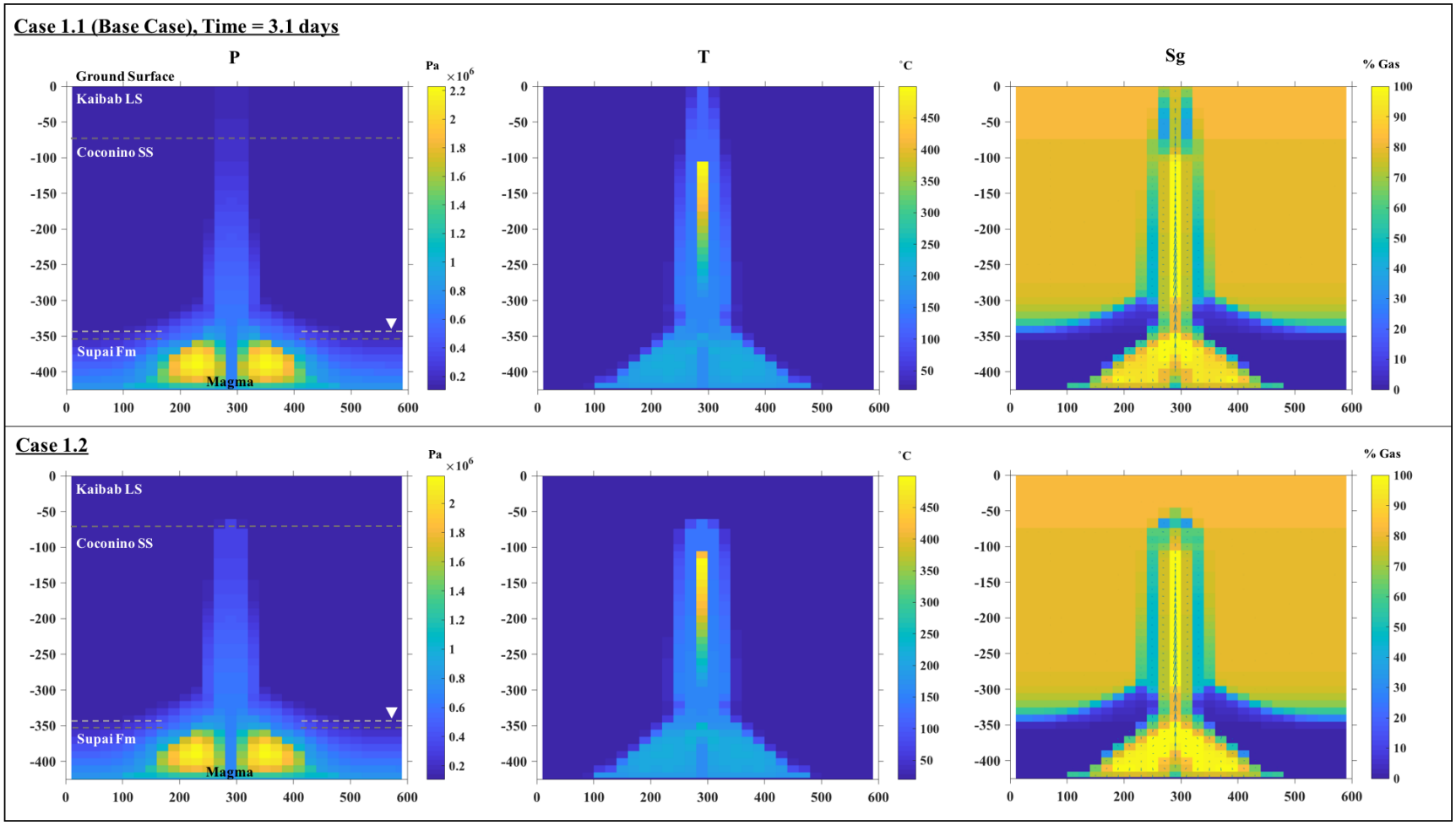

Figure 13: Pressure, temperature, and gas saturation at t ~ 3.1 days for simulations with rapid timed heat injection up to 100 m depth. Case 1.1 (top) includes a fracture zone that extends from the ground surface to 425 m depth, and Case 1.2 (bottom) includes a fracture zone that extends from the Kaibab-Coconino boundary to 425 m. Largest gas flow rate vector in fracture zones: $V_Z = 0.29$ kg/s, $V_X = 6.00 \times 10^{-6}$ kg/s (Case 1.1); $V_Z = 0.25$ kg/s, $V_X = -5.50 \times 10^{-6}$ kg/s (Case 1.2)

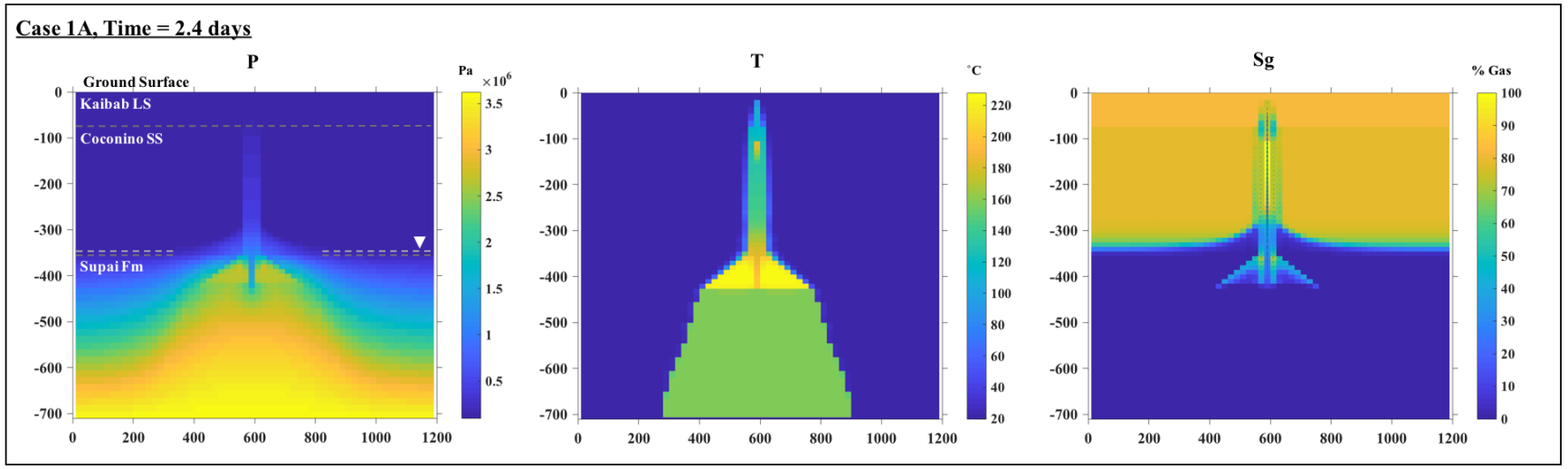

Figure 14: Pressure, temperature, and gas saturation at ~2.4 days for a large-scale simulation of rapid, timed heat injection up to 100 m depth (Case 1A). Maximum gas flow rate in fracture zone (V_Z = 0.22 kg/s)

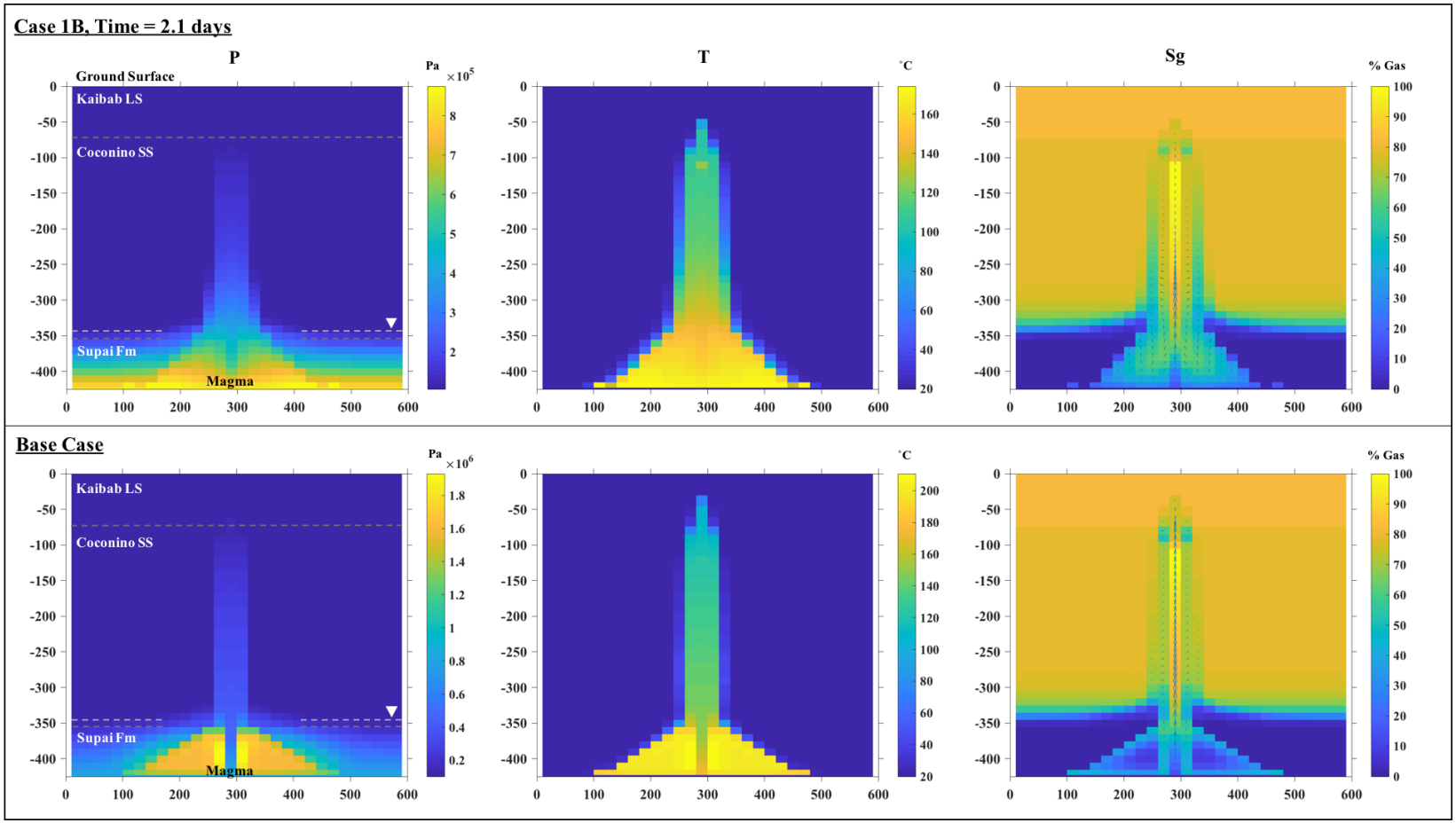

Figure 15: Pressure, temperature, and gas saturation at ~2.1 days for rapid heat injection simulations with increased country rock permeability (Case 1B, top) and base case conditions (bottom). Largest gas flow rate vector in fracture zone: $V_Z = 0.34$ kg/s, $V_X = -7.53 \times 10^{-6}$ kg/s (Case 1B).

Figure 16 (next page): Pressure, temperature, and gas saturation at ~1.4 days for rapid heat injection simulations with decreased country rock permeability. Lowest tested permeability (Case 1C), moderately low permeability (Case 1D), and base case permeability. Largest gas flow rate vector in fracture zones: $V_Z = 0.11$ kg/s (Case 1C); $V_Z = 9.03 \times 10^{-2}$, $V_X = 1.05 \times 10^{-6}$ kg/s (Case 1D).

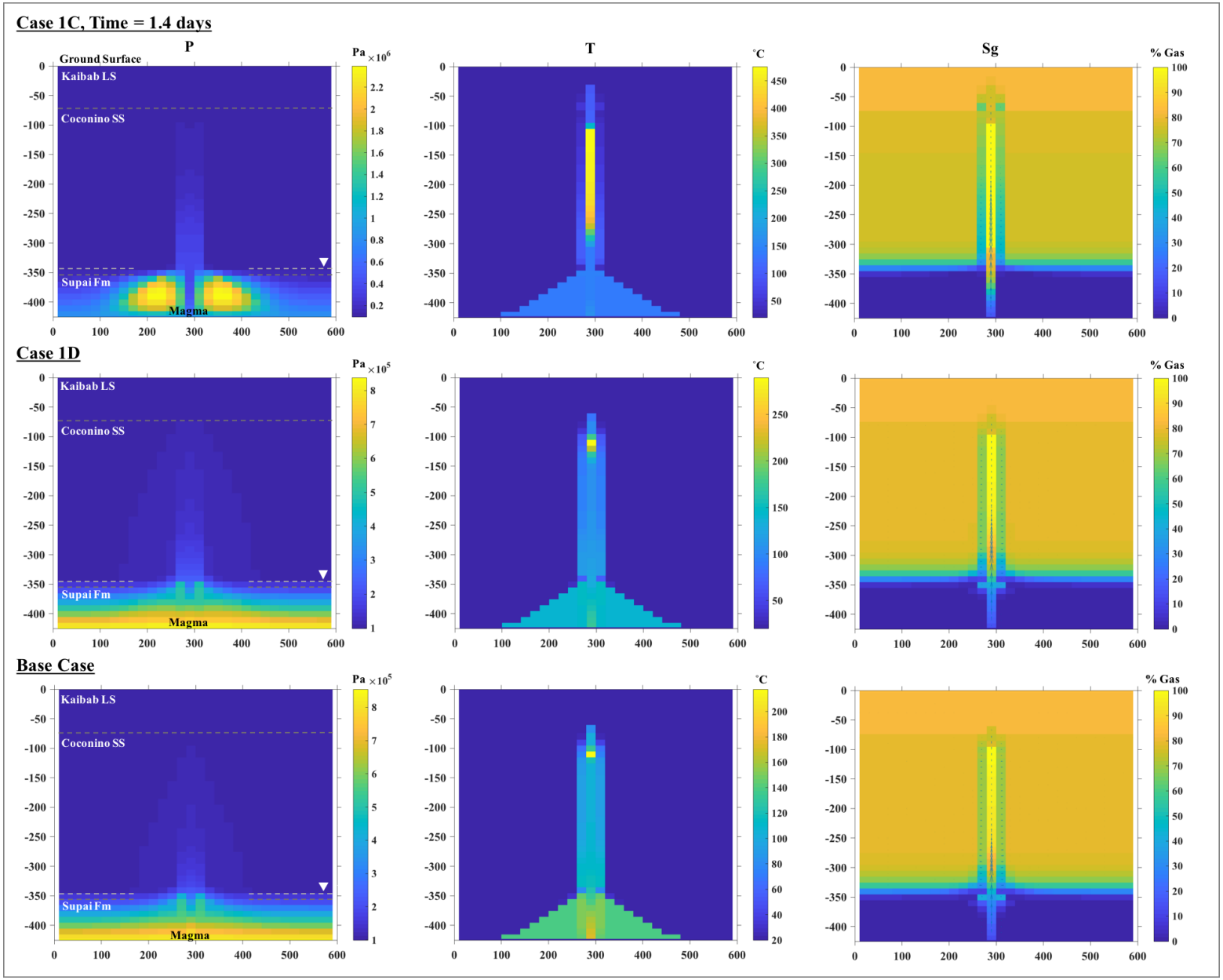
Case 1C, Time = 1.4 days
P
T
Sg
Ground Surface
Kaibab LS
Coconino SS
Supai Fm
Magma
Pa
×10^6
°C
% Gas
Case 1D
Pa
×10^5
°C
% Gas
Base Case
Pa
×10^5
°C
% Gas

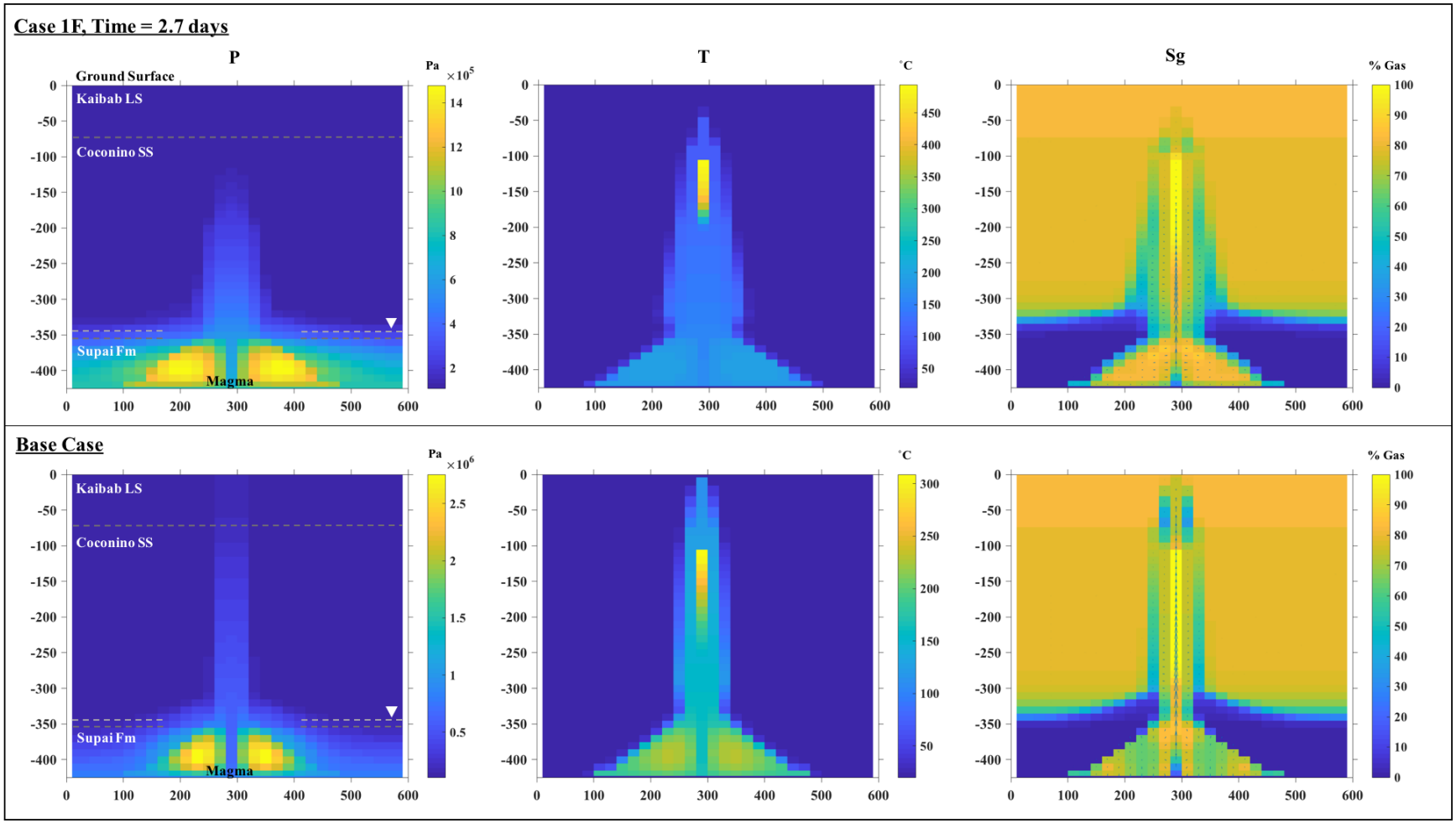

Figure 17: Pressure, temperature, and gas saturation at ~2.7 days for a rapid heat injection simulation with increased country-rock permeability in the x-direction (Case 1F). Largest gas flow rate vector in fracture zone: $V_Z = 0.54$ kg/s, $V_X = 4.86 \times 10^{-4}$ kg/s (Case 1F).

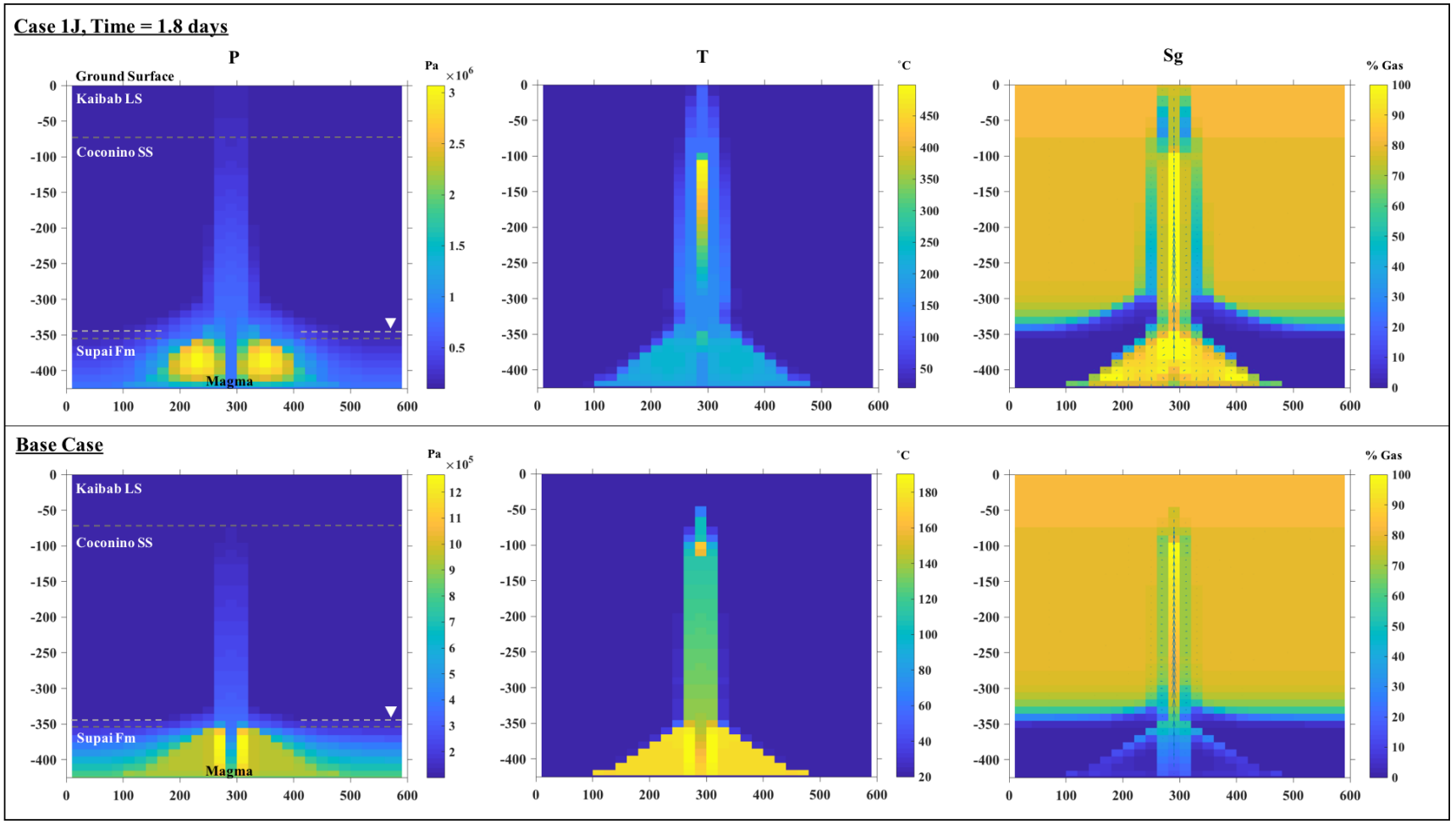

Figure 18: Pressure, temperature, and gas saturation at ~1.8 days for rapid heat injection simulations with increased heat rate (Case 1J) and base-case heat rate. Largest gas flow rate vector in fracture zone: $V_Z = 0.45$ kg/s, $V_X = 1.50 \times 10^{-5}$ kg/s (Case 1J).

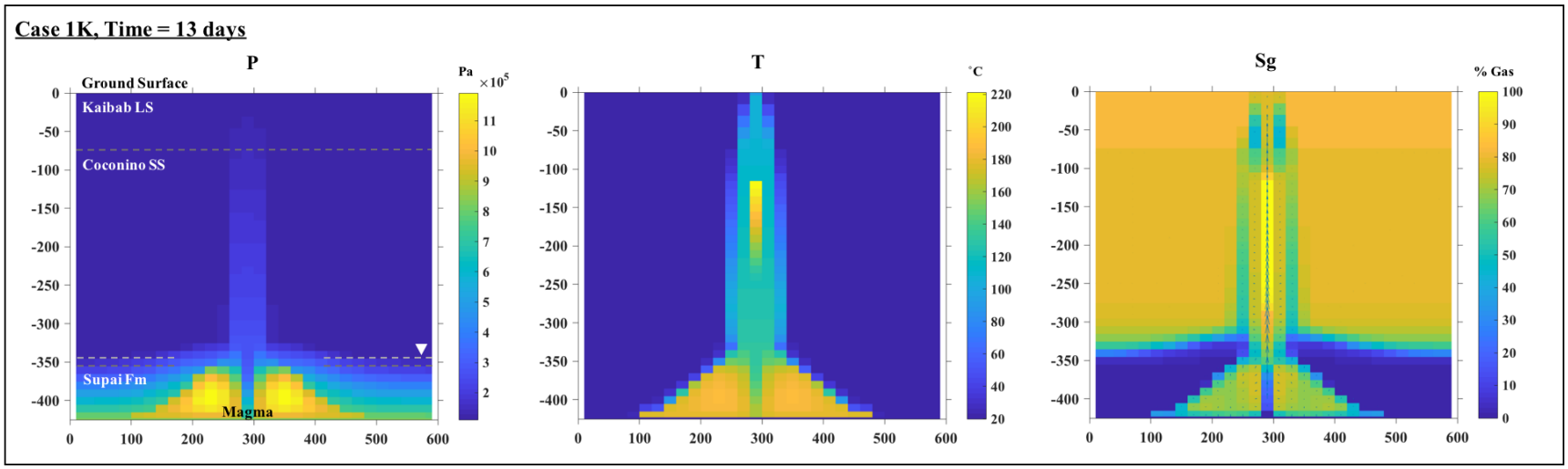

Figure 19: Pressure, temperature, and gas saturation at ~13 days for a rapid timed heat injection simulation with decreased heat rate (Case 1K). Largest gas flow rate vector in fracture zone: $V_Z = 6.74 \times 10^{-2}$ kg/s, $V_X = 7.55 \times 10^{-6}$ kg/s (Case 1K).

Figure 20 (next page): Pressure, temperature, and gas saturation at ~2.1 days for rapid heat injection simulations with a raised water table at 315 m depth (Case 1L) and a lowered water table at 375 m depth (Case 1M). Largest gas flow rate vectors in fracture zones: $V_Z = 0.52$ kg/s, $V_X = 1.35 \times 10^{-5}$ kg/s (Case 1L); $V_Z = 0.17$ kg/s, $V_X = 1.05 \times 10^{-5}$ kg/s (Case 1M).

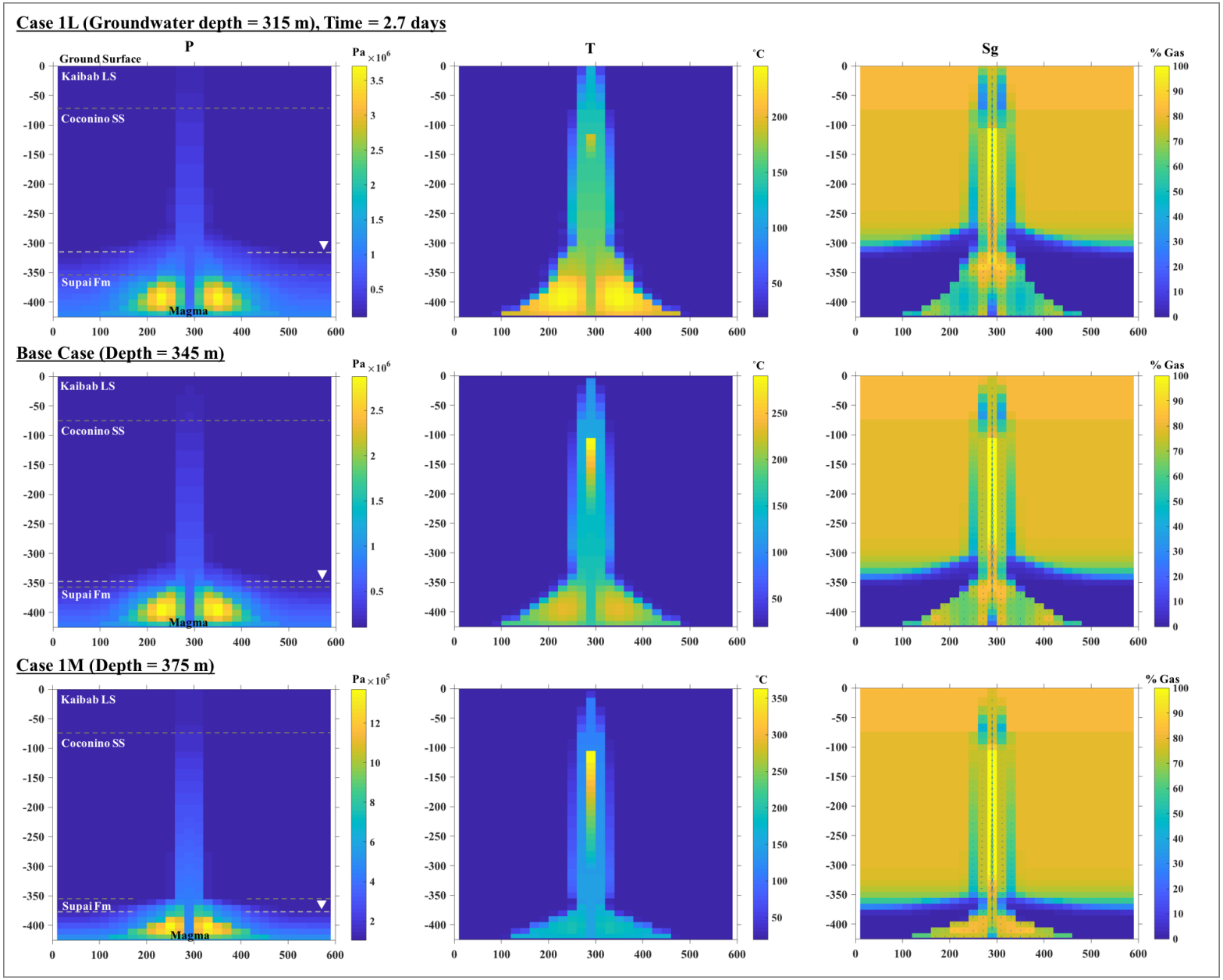
Case 1L (Groundwater depth = 315 m), Time = 2.7 days
P
T
Sg
Ground Surface
Kaibab LS
Coconino SS
Supai Fm
Magma
Pa ×10^6
°C
% Gas
Base Case (Depth = 345 m)
Case 1M (Depth = 375 m)
Pa ×10^5

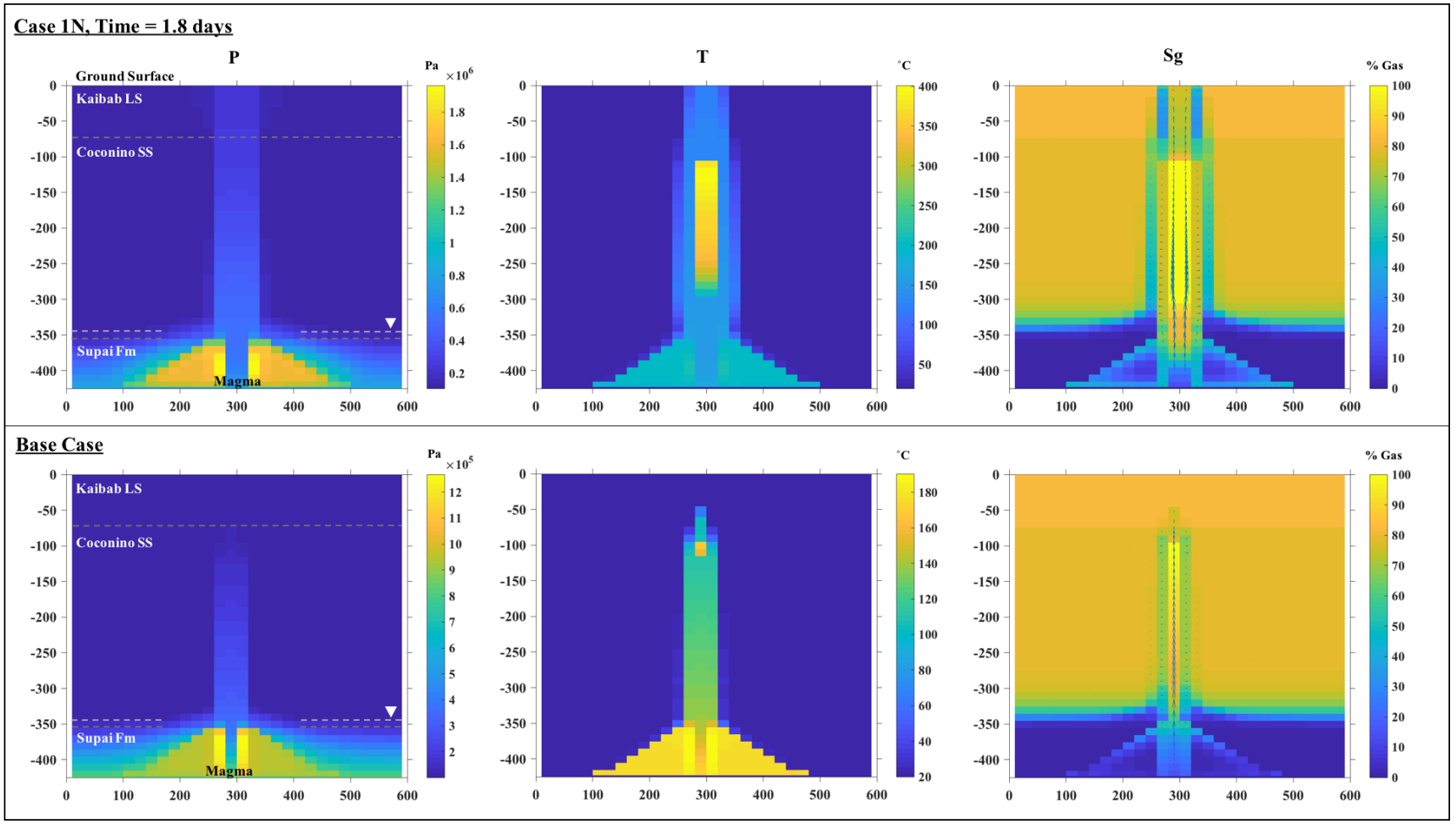

Figure 21: Pressure, temperature, and gas saturation at ~2.1 days for rapid heat injection simulations with a 40-m-wide fracture (Case 1N) and a 20-m-wide fracture (base case). Largest gas flow rate vector in fracture zone: $V_Z = 0.16$ kg/s, $V_X = 1.46 \times 10^{-2}$ kg/s (Case 1N).

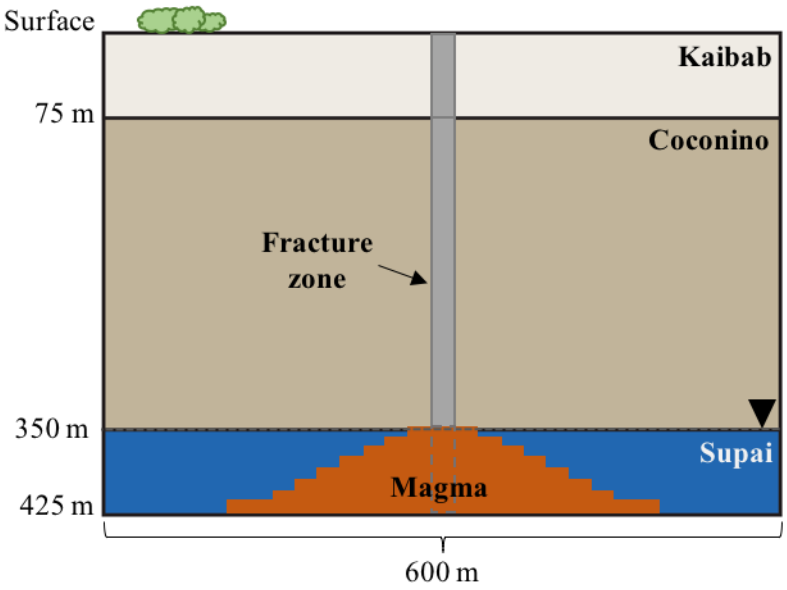

Figure 22: Schematic diagram showing the standard setup for constant-rate, slow heat injection models. In the small models, the magma source is 360 m wide at the base and 60 m wide at the water table.

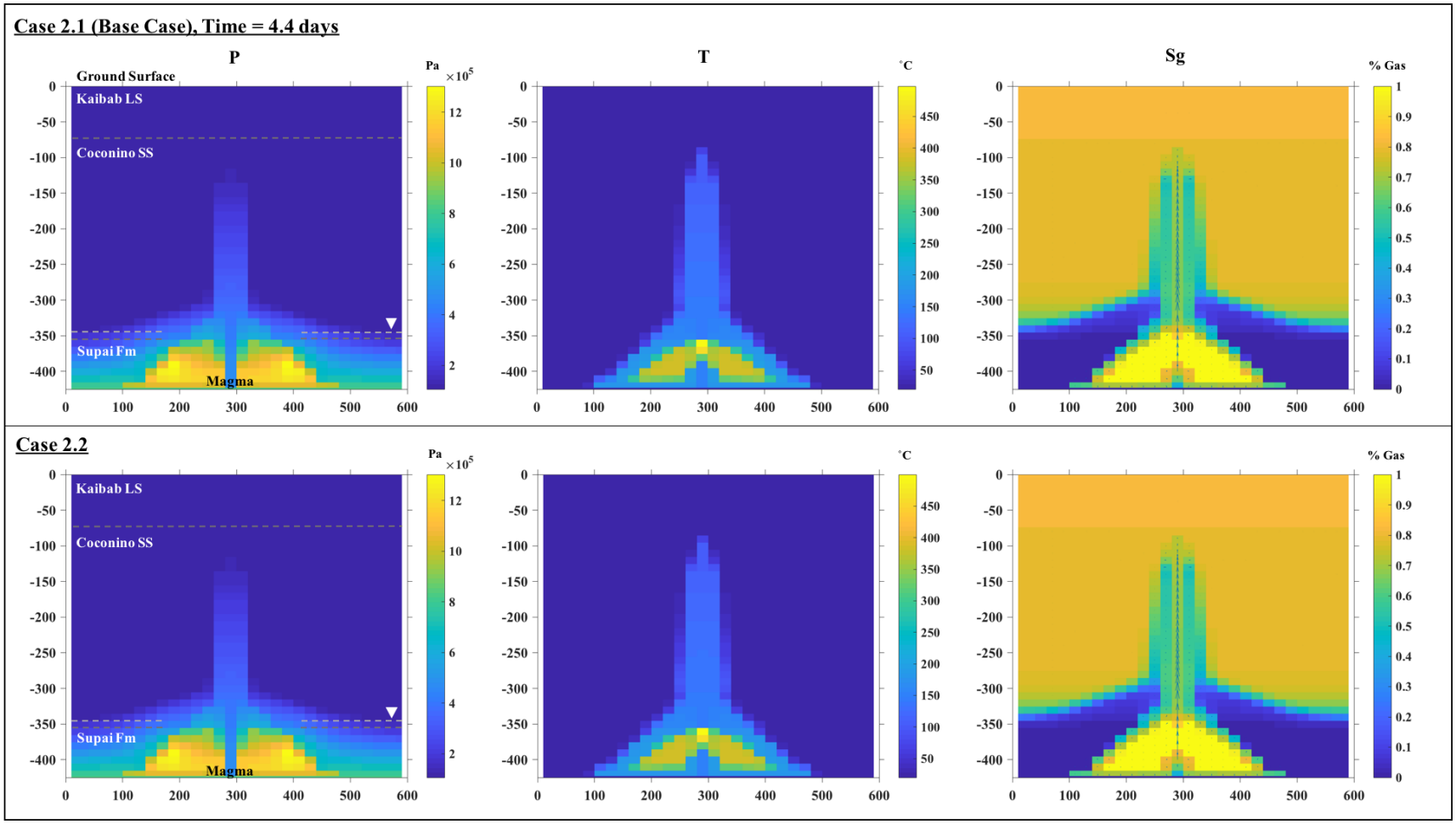

Figure 23: Pressure, temperature, and gas saturation at ~4.4 days for stalled heat injection simulations under standard conditions. Fracture extent from Kaibab-Coconino boundary to 425 m (Case 2.1, top) and from top boundary to 425 m (Case 2.2, bottom). Largest gas flow rate vectors in fracture zone: $V_Z = 0.15$ kg/s, $V_X = 4.45 \times 10^{-6}$ kg/s (Case 2.1); $V_Z = 0.15$ kg/s, $V_X = 3.65 \times 10^{-7}$ kg/s (Case 2.2).

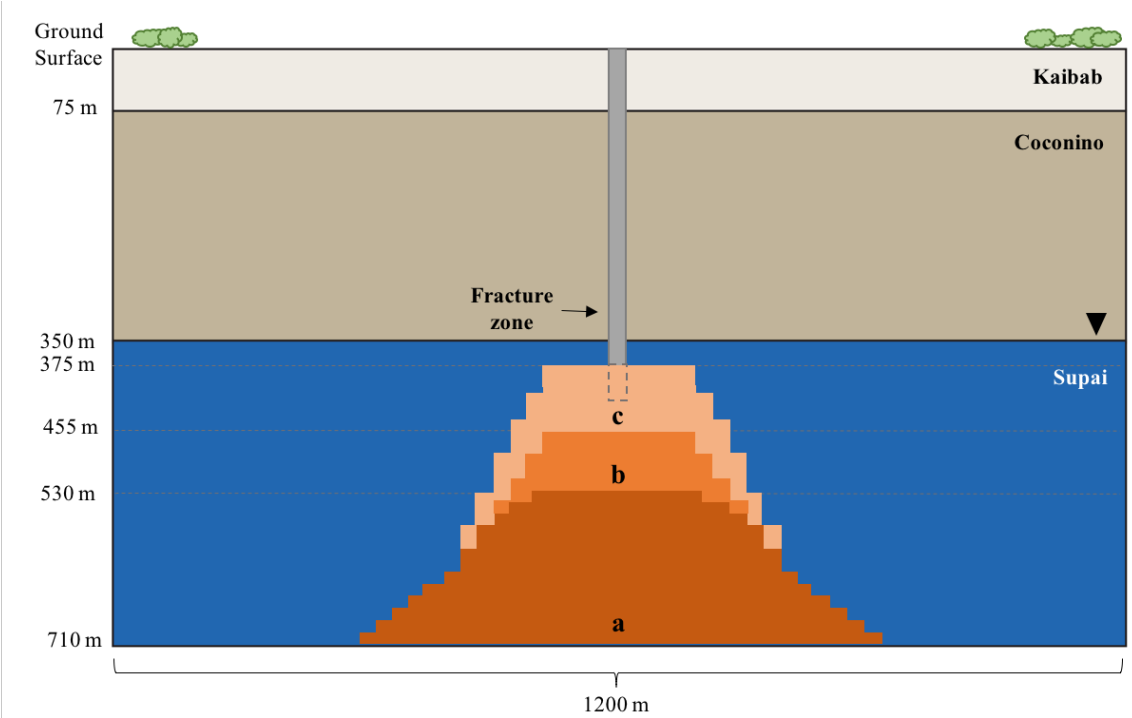

Figure 24: Schematic diagram showing the large mesh, slow heat injection setup. (a) indicates the area of direct heat injection for the model at standard conditions and the first step of the series of injections at a decreased heat rate. (b) is the added zone of heat injection in the second step of the low heat model, and (c) is added in the final step. Fracture extent is indicated by the dashed gray line into zone (c).

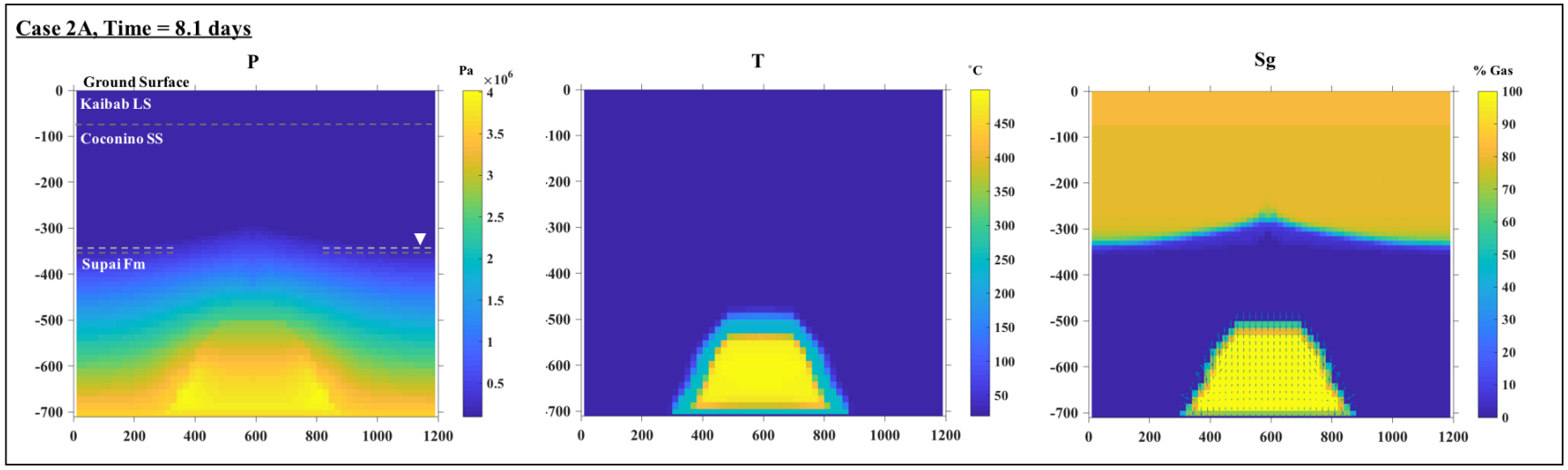

Figure 25: Pressure, temperature, and gas saturation at ~8.1 days for a large-scale, stalled heat injection simulation under standard conditions (Case 2A). Fracture extends from top boundary to 425 m, and heat injection reaches 525 m. Largest gas flow rate vector in fracture zone: $V_Z = 1.25 \times 10^{-2}$ kg/s, $V_X = -6.47 \times 10^{-3}$ kg/s.

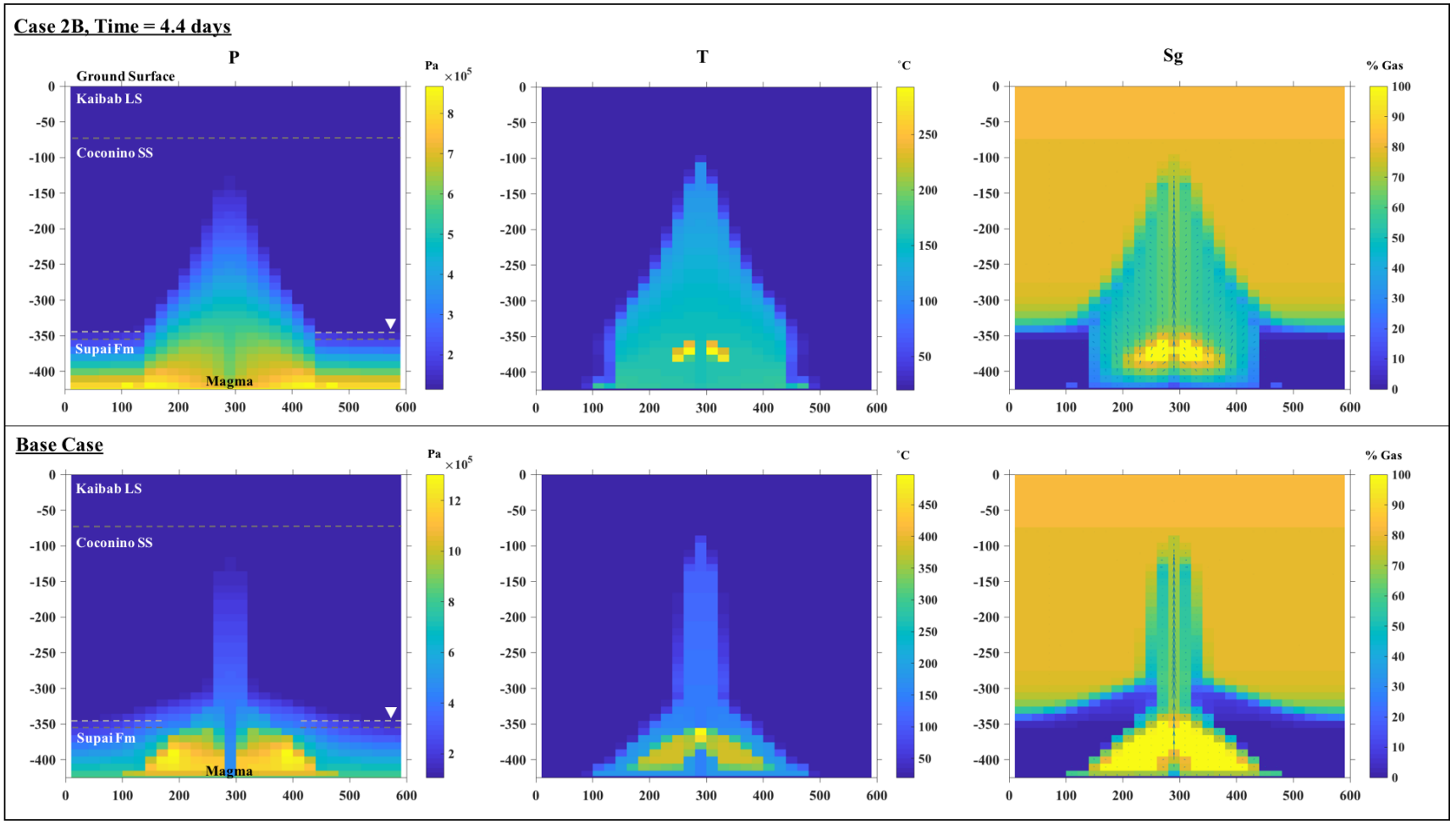

Figure 26: Pressure, temperature, and gas saturation at ~4.4 and 5.6 days for a stalled heat injection simulation with increased country-rock permeability (Case 2B). Largest gas flow rate vector in fracture zone: $V_Z = 0.27$ kg/s, $V_X = -4.50 \times 10^{-7}$ kg/s (Case 2B).

Figure 27 (following page): Pressure, temperature, and gas saturation at ~4 days for stalled heat injection simulations with low (Case 2C), moderately low (Case 2D), and base-case permeabilites. Largest gas flow rate vector in fracture zones: $V_Z = 0.25$ kg/s, $V_X = 0$ kg/s (Case 2C); $V_Z = 0.44$ kg/s, $V_X = -1.44 \times 10^{-6}$ kg/s (Case 2D).

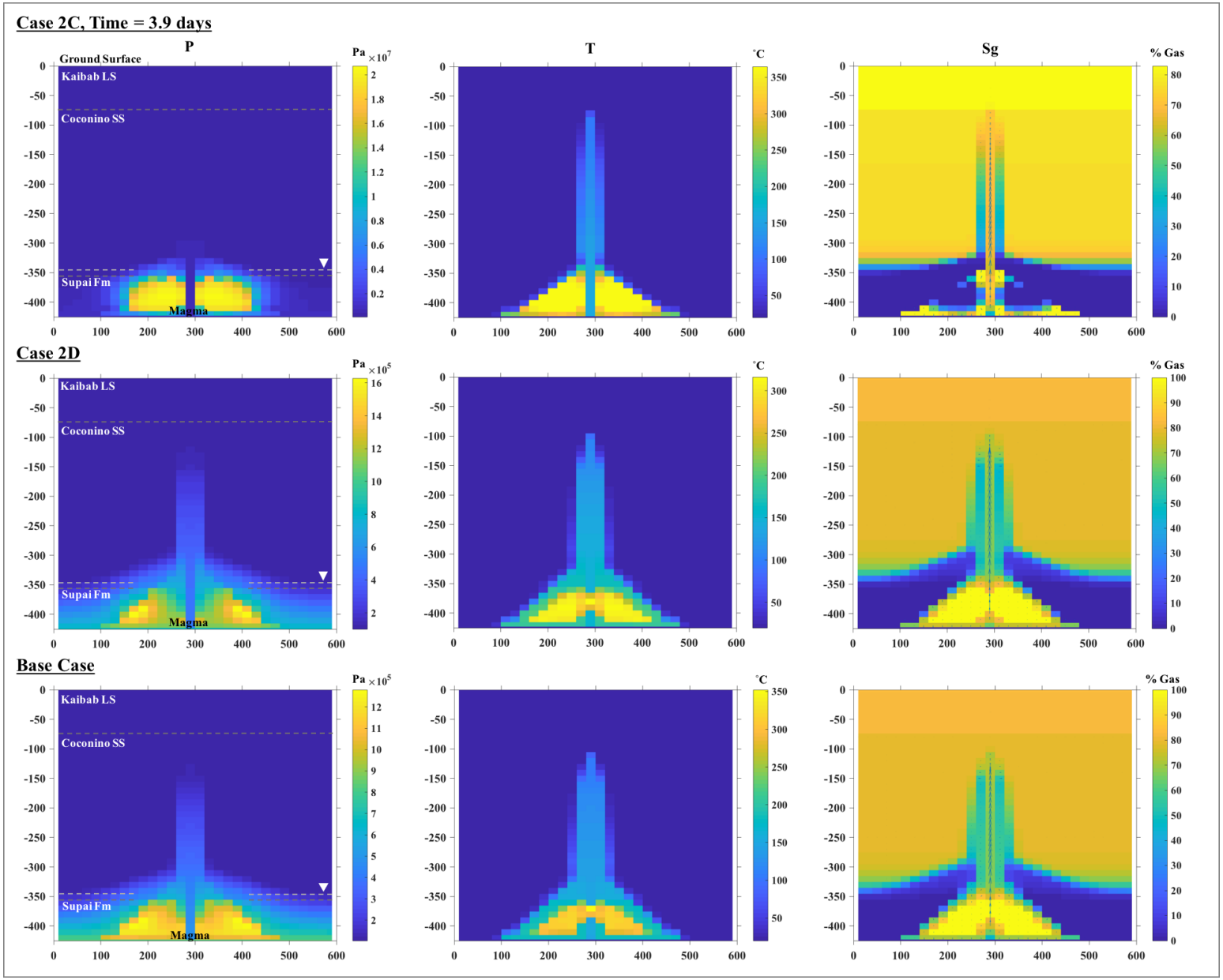
Case 2C, Time = 3.9 days
P
T
Sg
Ground Surface
Kaibab LS
Coconino SS
Supai Fm
Magma
Pa
×10^7
°C
% Gas
Case 2D
Pa
×10^5
Base Case

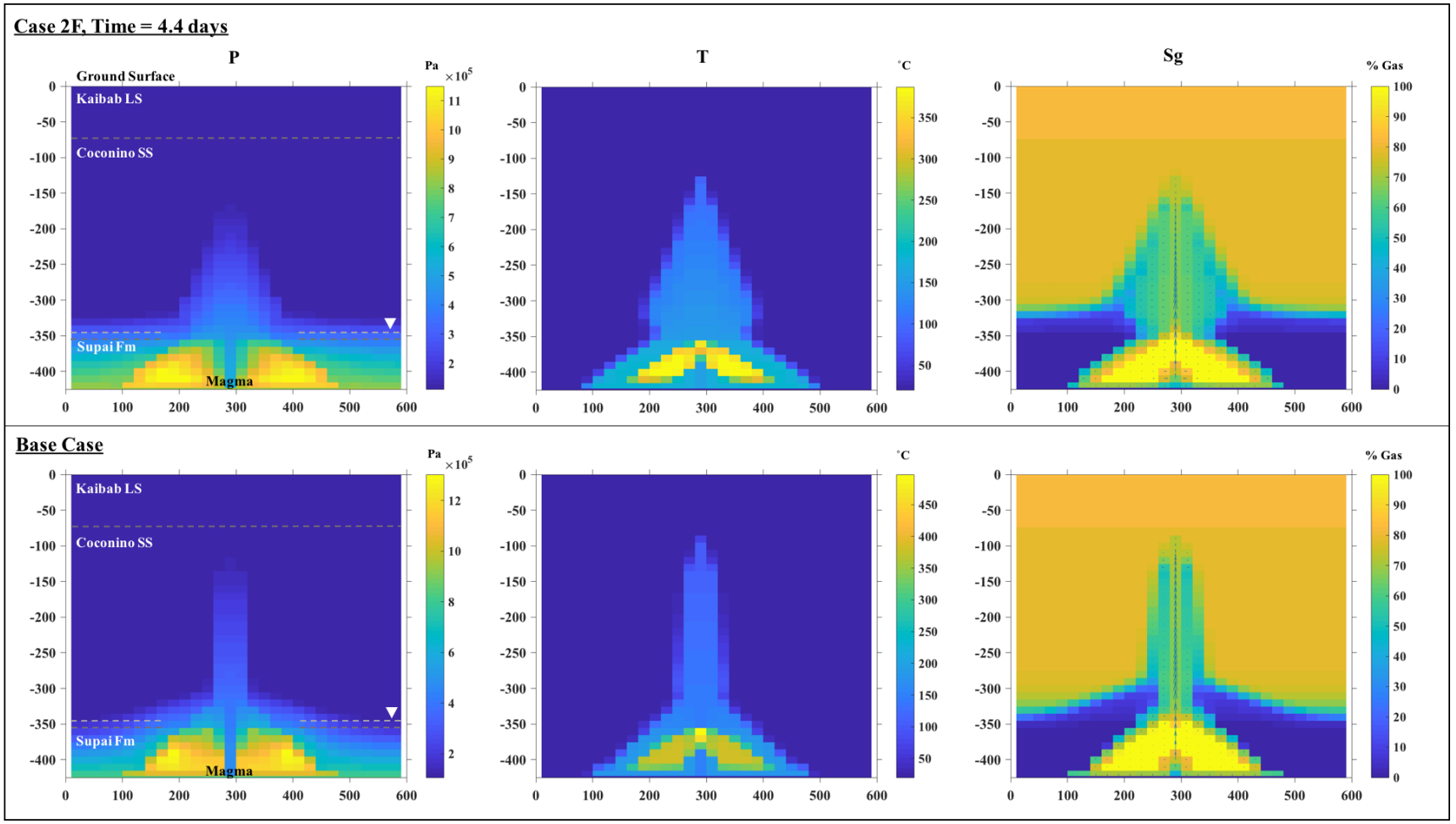

Figure 28: Pressure, temperature, and gas saturation at ~4.4 days for a stalled heat injection simulation with increased country-rock permeability in the x-direction (Case 2F). Largest gas flow rate vector in fracture zone: $V_Z = 0.27$ kg/s, $V_X = 2.34 \times 10^{-4}$ kg/s (Case 2F).

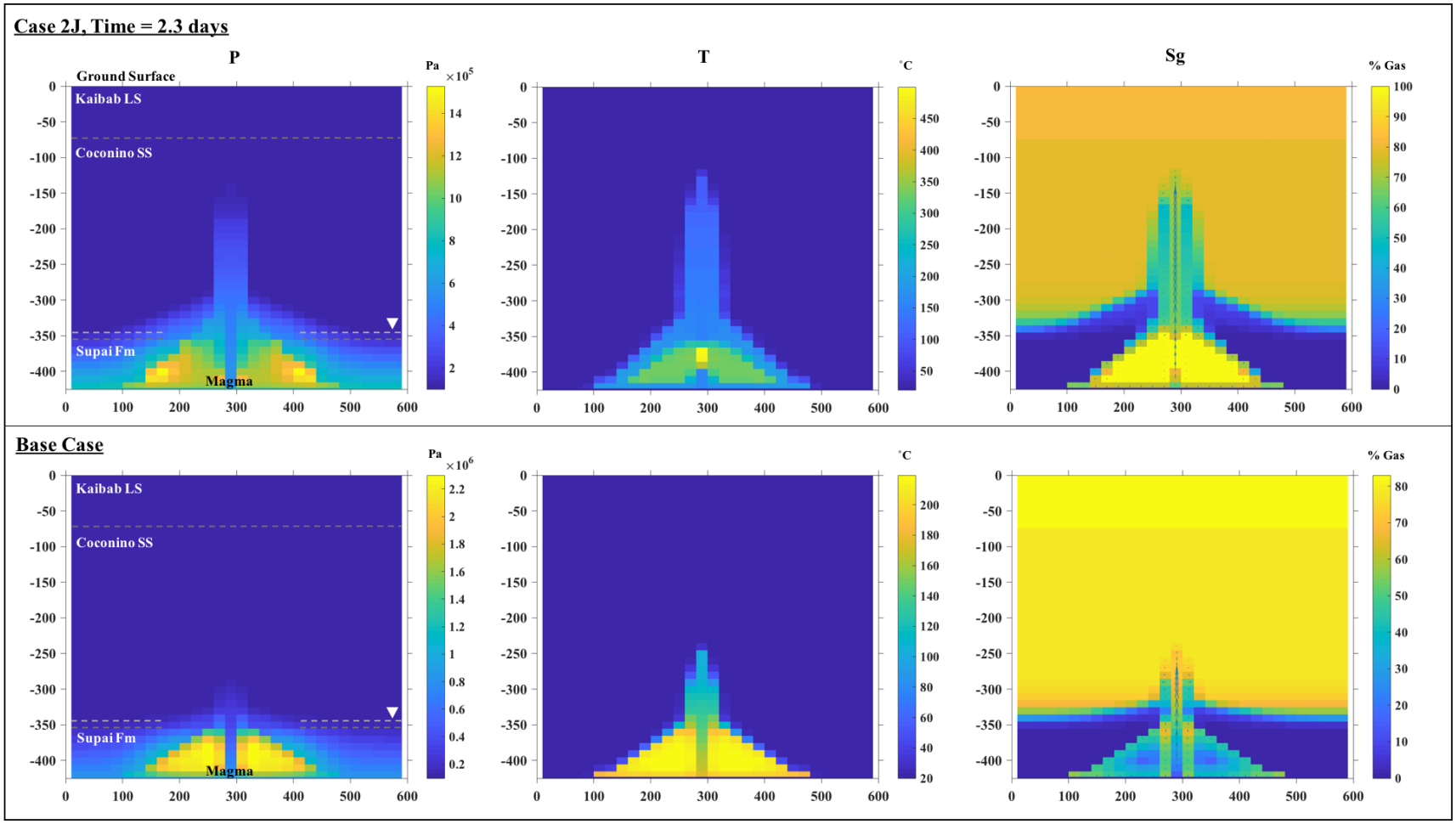

Figure 29: Pressure, temperature, and gas saturation at ~2.3 days for stalled heat injection simulations with increased heat rate (Case 2J) and base-case heat rate. Largest gas flow rate vector in fracture zone: $V_Z = 0.19$ kg/s, $V_X = 5.30 \times 10^{-7}$ kg/s (Case 2J).

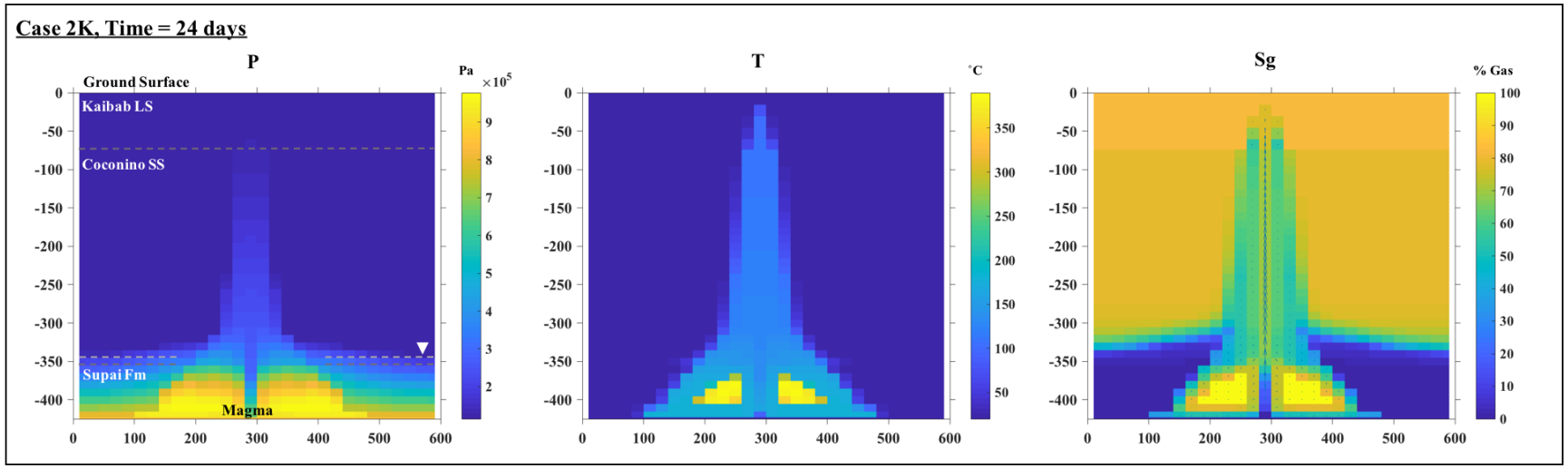

Figure 30: Pressure, temperature, and gas saturation at ~24 days for a stalled heat injection simulation with decreased heat rate (Case 2K). Largest gas flow rate vector in fracture zone: $V_Z = 5.00 \times 10^{-2}$ kg/s, $V_X = 4.85 \times 10^{-6}$ kg/s.

Figure 31 (next page): Pressure, temperature, and gas saturation for stalled heat injection simulations with water-table depth at 315 m (Case 2L), 345 m (Case 2.1), and 375 m (Case 2M). Largest gas flow rate vector in fracture zones: $V_Z = 0.20$ kg/s, $V_X = 9.00 \times 10^{-7}$ kg/s (Case 2L); $V_Z = 0.13$ kg/s, $V_X = 1.20 \times 10^{-10}$ kg/s..

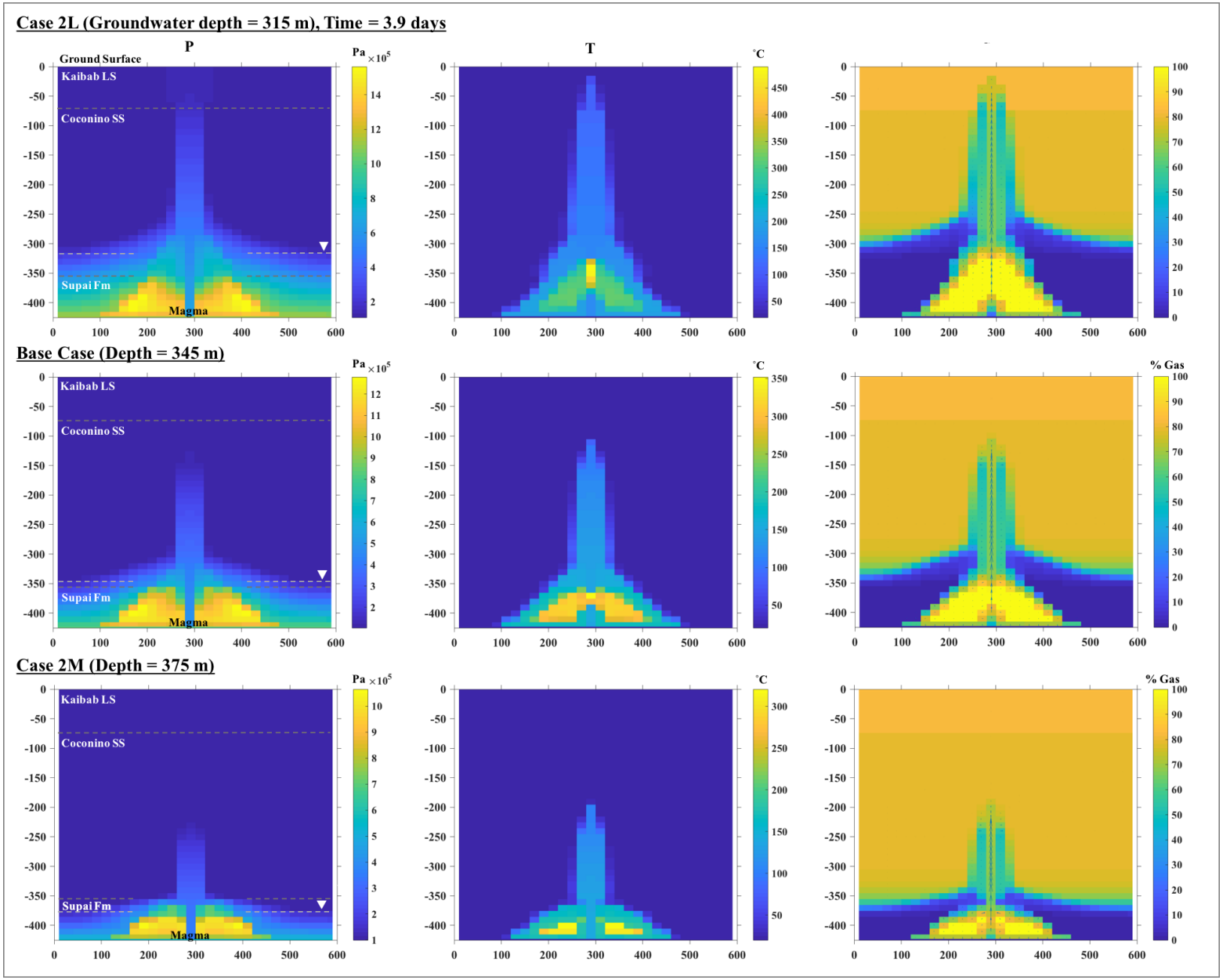
Case 2L (Groundwater depth = 315 m), Time = 3.9 days
P
T
Pa
×10^5
°C
% Gas
Ground Surface
Kaibab LS
Coconino SS
Supai Fm
Magma
Base Case (Depth = 345 m)
Case 2M (Depth = 375 m)

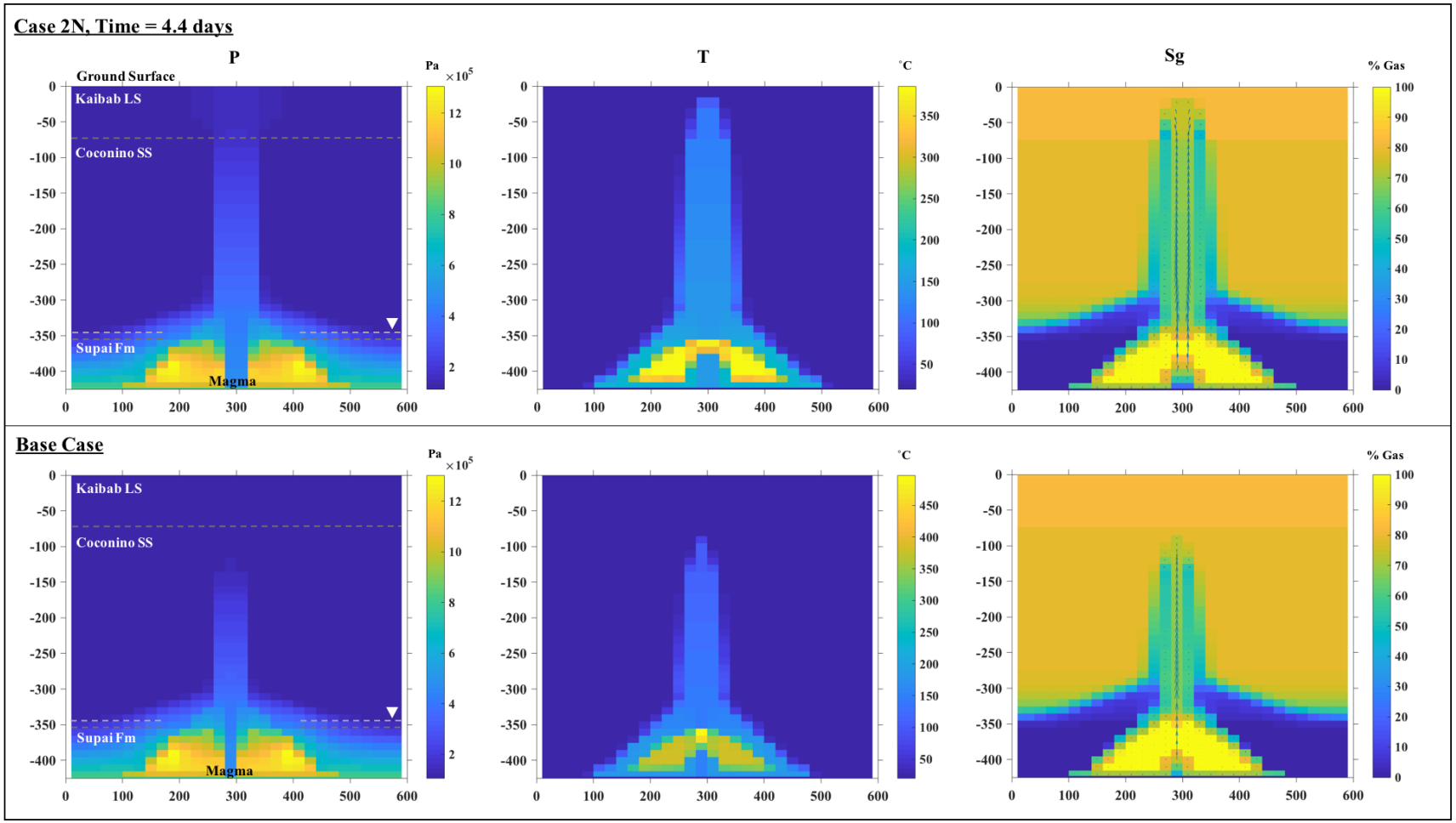

Figure 32: Pressure, temperature, and gas saturation for stalled heat injection simulations with a 40-m-wide fracture zone (Case 2N) and the base case 20-m-wide fracture zone. Largest gas flow rate vector in fracture zone: $V_Z = 0.12$ kg/s, $V_X = 1.63 \times 10^{-3}$ kg/s.

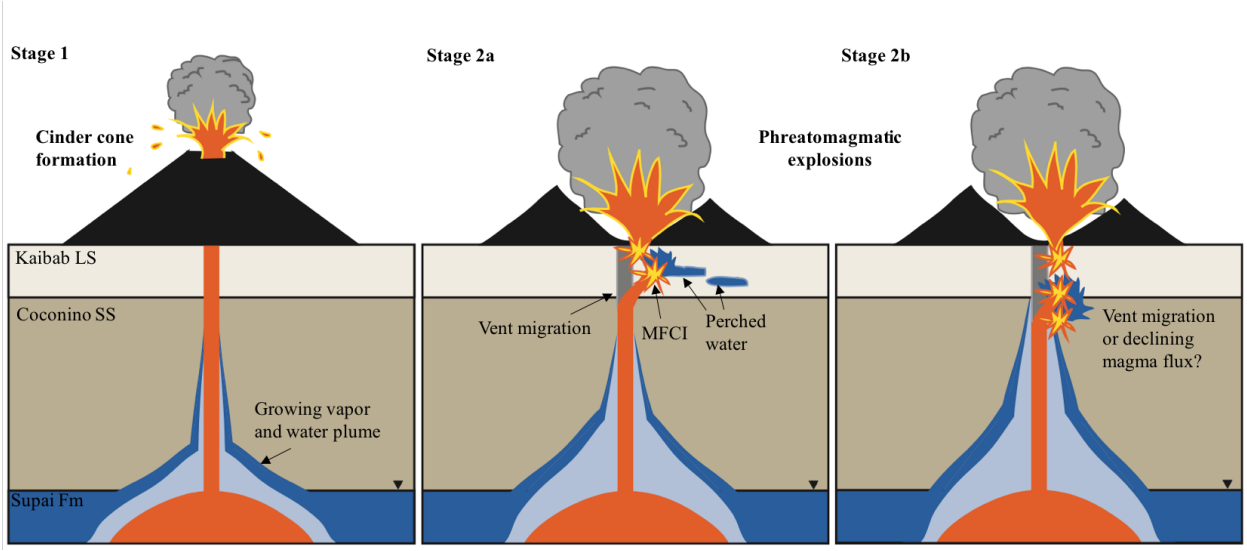

Figure 33: Schematic diagram showing possible scenarios for the eruption of Colton Crater. The eruption started with Strombolian activity, building a large cinder cone (Stage 1). Phreatomagmatic explosions may have been caused by vent migration meeting pre-existing perched water (Stage 2a) or water that had been driven up as vapor throughout eruption (Stage 2b). Water from either source could have also flowed into the vent as a result of declining or stalled magma flux.

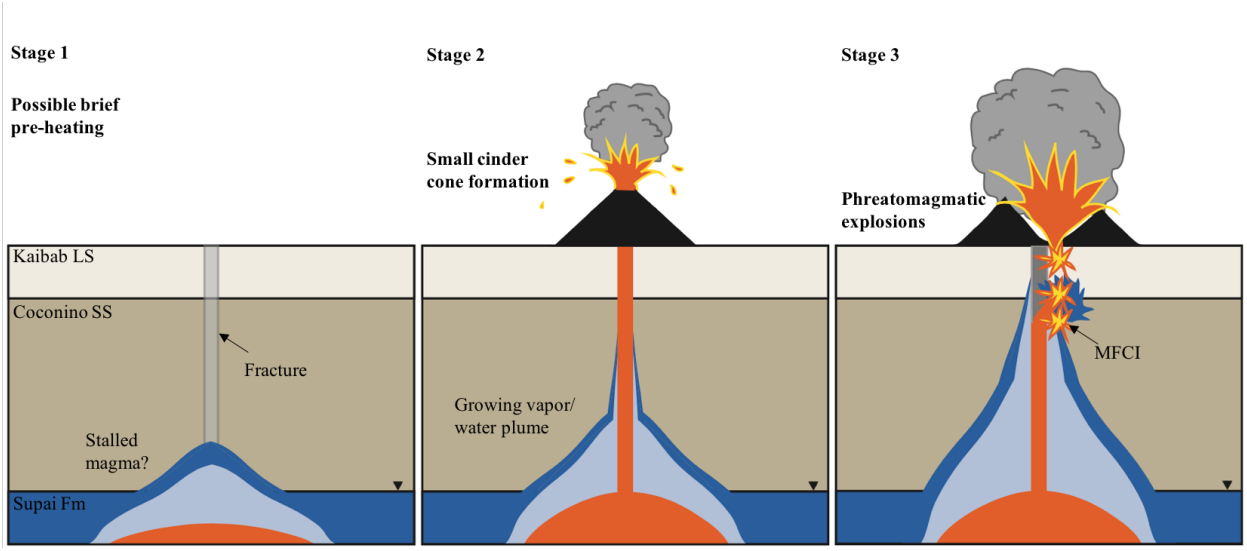

Figure 34: Schematic diagram showing possible eruptive activity of Rattlesnake Crater. The eruption began with a brief dry period (Stage 1). The presence of a magma body near the water table may have driven up a large quantity of vapor and condensed water prior to or during eruption (Stage 2), which could then interact with branching dikes to begin phreatomagmatic explosions (Stage 3).

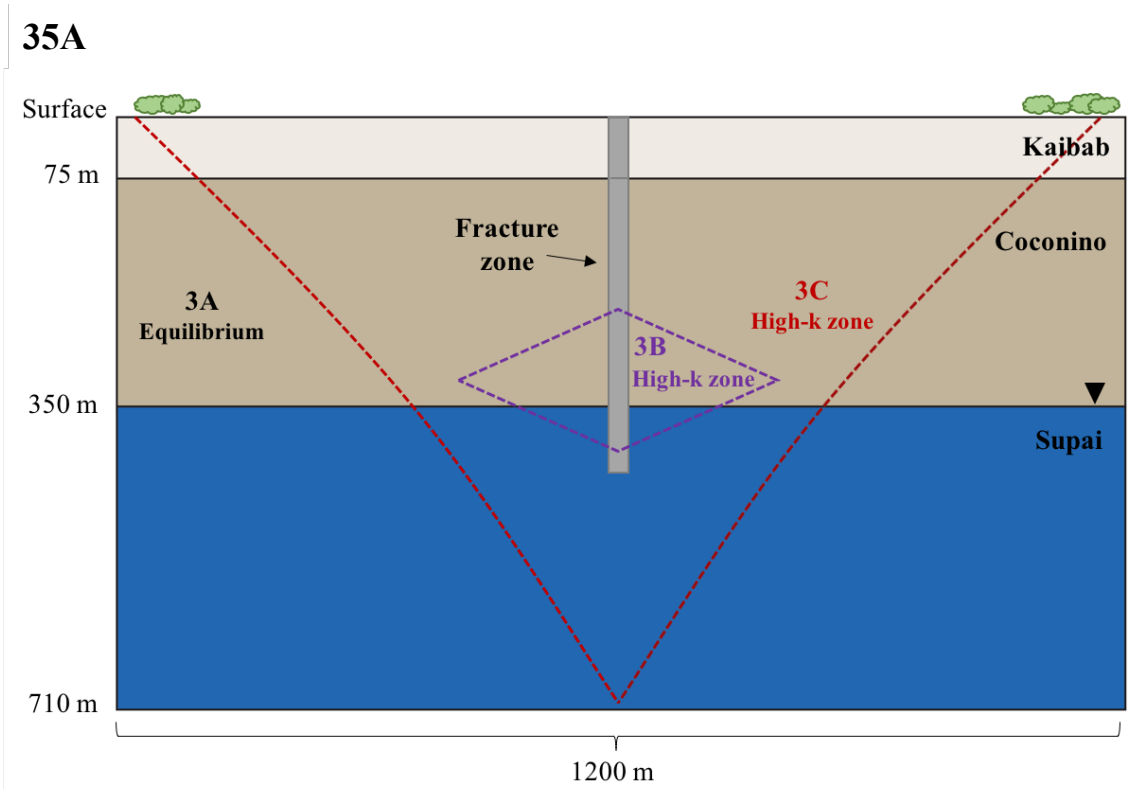

Figure 35: (A) Simplified schematic diagram showing changes to initial conditions of each step of the progressive diatreme growth simulation. Case 3A is started at equilibrium (B) Pressure, temperature, and gas saturation for a simplified model of progressive diatreme growth. Case 3A (top) shows magma injection up to 100 m depth after ~4.4 days. Case 3B (middle) is a continuation of Case 3A, but with a zone of high permeability added to represent explosions occurring near the raised water table. Case 3C (bottom) is a continuation of Case 3B with a large-scale, high-permeability diatreme structure.

35B

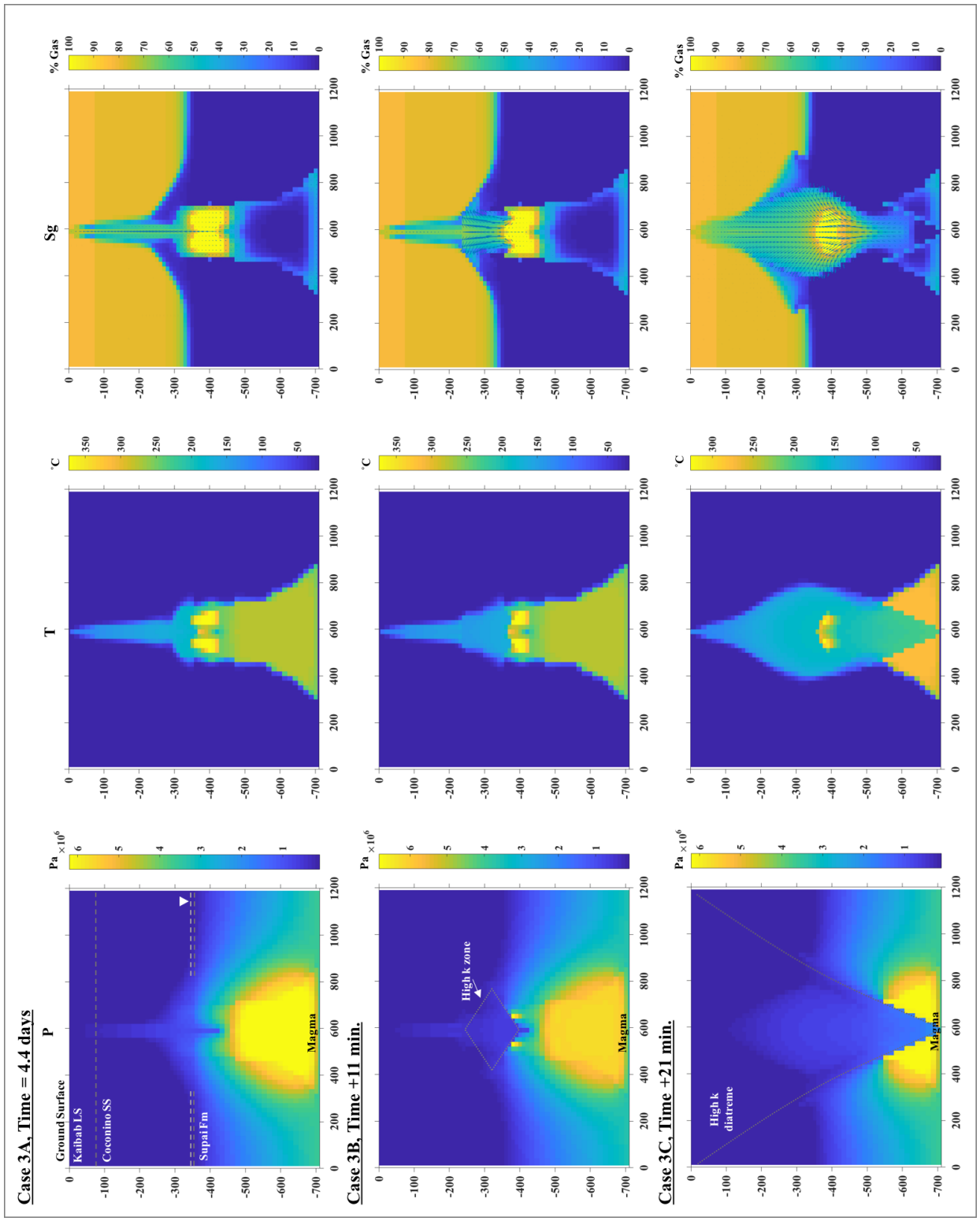
Case 3A, Time = 4.4 days
P
T
Sg
Pa
°C
% Gas
Ground Surface
Kaibab LS
Coconino SS
Supai Fm
Magma
Case 3B, Time +11 min.
High k zone
Case 3C, Time +21 min.
High k diatreme

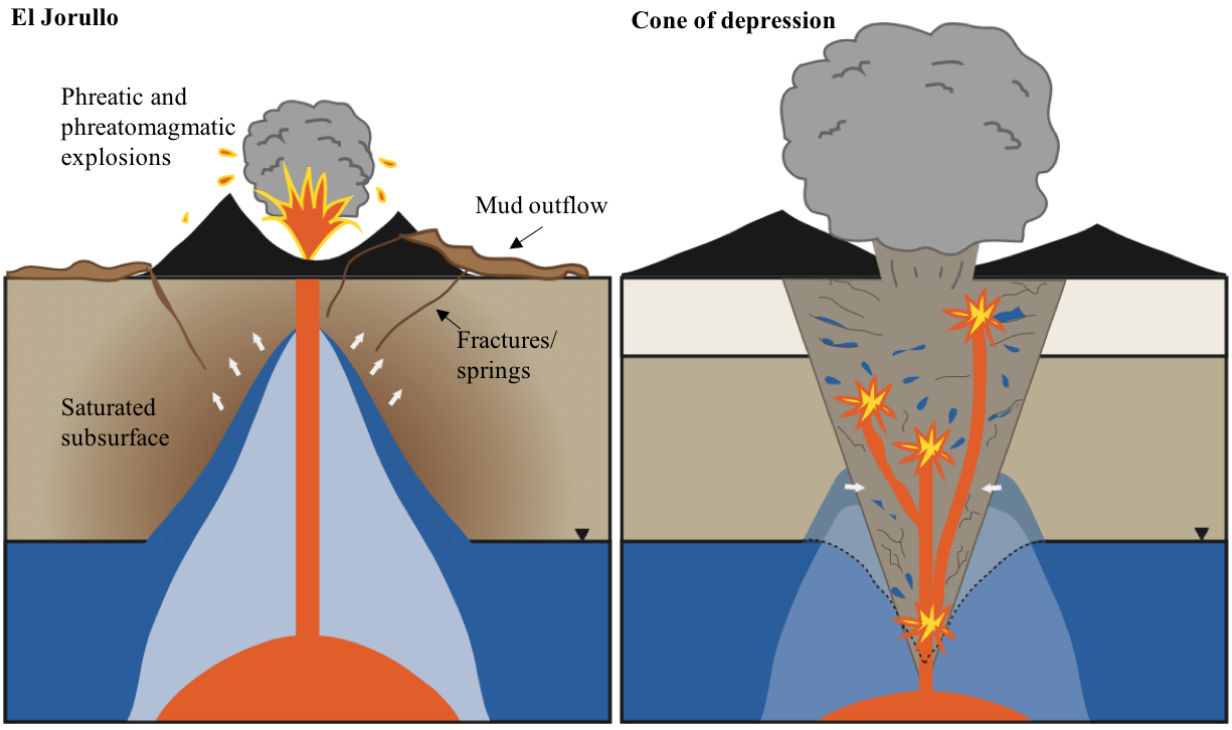

Figure 36: (Left-hand side) Schematic demonstrating possible syn-eruptive vapor and liquid water transport driving the surficial mud flows around El Jorullo. A plume of heated vapor and associated condensing water could saturate permeable subsurface material prior to and during an eruption, forming mud that is then driven out of the ground through fractures and springs. (Right-hand side) The modeled processes may help drive shallow explosions in locations where the water table itself is depleted throughout an eruption. Upward vapor transport may provide shallow liquid water to many locations throughout the diatreme and surrounding area, which can then interact with intra-diatreme dikes and produce explosions.

APPENDIX A

RESOURCE DATA

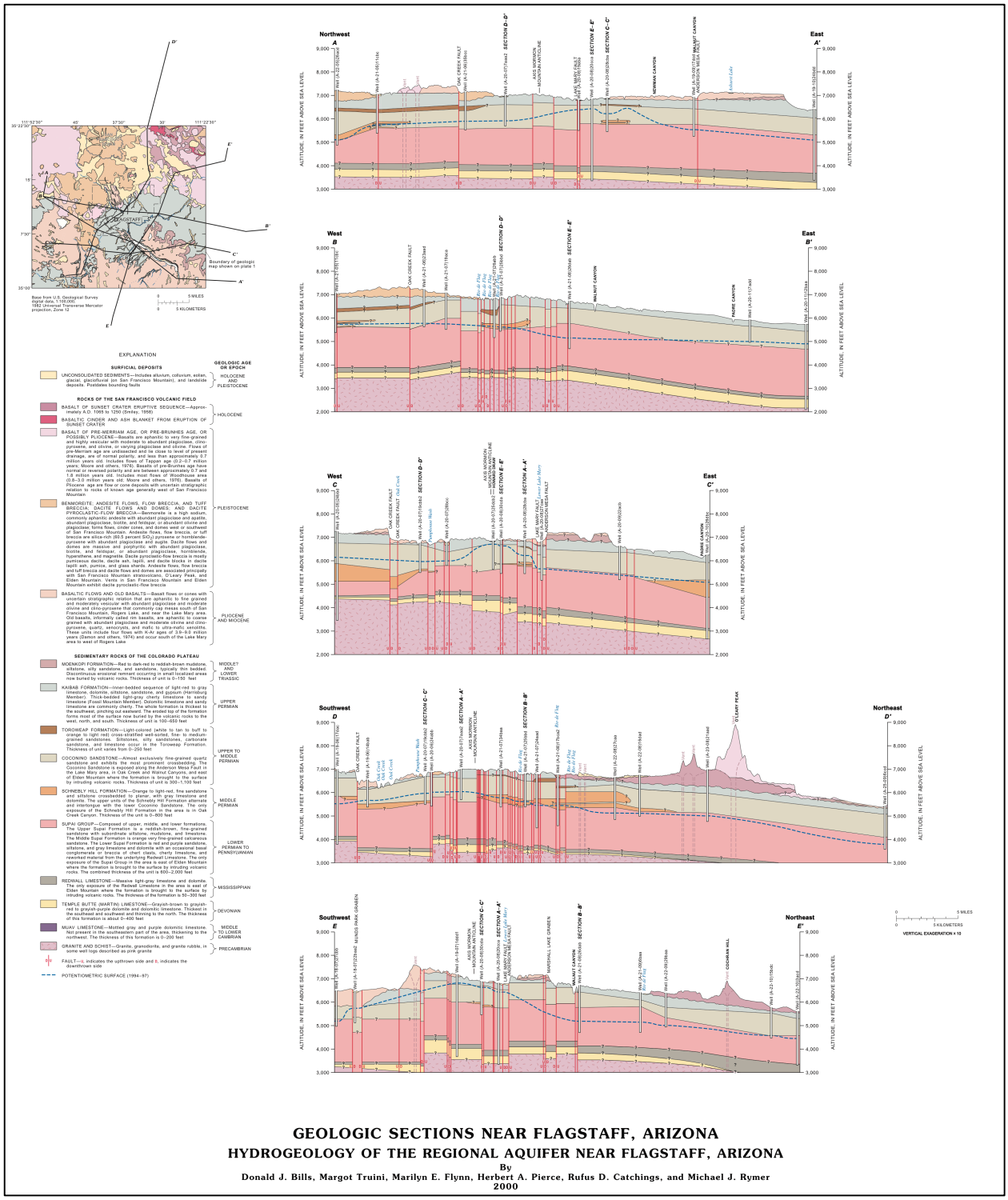

Figure A-1: Geologic cross sections near Flagstaff, AZ. From Bills et al. (2000).

Water-level data for wells near Flagstaff, Arizona

[Wells are in order by well-reference number. Dashes indicate no data]

Well-reference number	Well name or owner	Site identifier	Latitude	Longitude	Water level: Date of measurement	Water level: Depth below land surface, in feet	Water level: Altitude, in feet
1	Pine Flats	(A-19-06)W27aaa	35°00'35"	111°44'18"	07-15-75	9.0	5,531
Do.	Do.	do.	do.	do.	04-11-94	6.6	5,533
2	Pine Grove	(A-19-09)17dcd	35°01'24"	111°27'35"	12-11-67	1,320.2	5,637
Do.	Do.	do.	do.	do.	06-05-95	1,416.0	5,541
3	Oil Discovery 1	(A-19-06)17dac	35°01'43"	111°46'32"	11-05-74	Dry	---
4	ADOT-89A	(A-19-06)W14bab	35°02'00"	111°43'55"	05-20-80	826.8	5,663
Do.	Do.	do.	do.	do.	04-07-94	819.0	5,671
5	LMEX-1	(A-19-08)05ddd1	35°03'05"	111°33'50"	04-05-94	141.8	6,818
6	Federal 1	(A-19-07)01ddd1	35°03'06"	111°35'55"	04-05-89	365.7	6,809
Do.	Do.	do.	do.	do.	08-17-95	365.6	6,809
7	Walter	(A-19-08)05add	35°03'30"	111°33'50"	09-15-79	31.0	6,929
8	Tilley	(A-19-08)04bbd	35°03'43"	111°33'37"	10-27-78	19.5	6,920
9	Henson	(A-19-08)04bbb	35°03'50"	111°33'35"	05-30-79	25.0	6,955
10	LMEX-2	(A-20-08)33cdb	35°04'05"	111°33'20"	04-05-94	407.6	6,532
11	LMEX-3	(A-20-08)32cab1	35°04'15"	111°34'25"	11-01-94	13.0	6,867
12	TH-4	(A-20-07)35bac	35°04'33"	111°37'34"	08-17-95	545.3	6,330
13	LM-9	(A-20-08)30dca	35°04'51"	111°35'25"	08-01-94	243.0	6,632
14	TH-3	(A-20-08)30cdd1	35°04'56"	111°35'25"	04-05-94	219.6	6,650
15	LMEX-4	(A-20-07)25dcb1	35°04'55"	111°36'15"	08-17-95	125.4	6,715
16	LM-7	(A-20-08)27cas	35°05'07"	111°32'10"	03-01-89	1,119.0	5,676
Do.	Do.	do.	do.	do.	08-01-94	1,138.5	5,656
17	Old LM-9	(A-20-08)28cba	35°05'10"	111°33'25"	12-05-89	640.0	6,220
Do.	Do	do.	do.	do.	04-05-94	639.5	6,220
18	Cook-2	(A-20-08)30cba2	35°05'10"	111°35'40"	04-13-95	127.1	6,683
19	Mountainaire	(A-20-07)28bcc	35°05'11"	111°40'00"	03-30-78	791.0	5,994
20	Kachina-2	(A-20-07)30bdb	35°05'16"	111°41'50"	04-14-94	455.3	6,030
21	Wahlers	(A-20-08)30bdb	35°05'20"	111°35'30"	06-12-85	120.0	6,700
22	Bathen	(A-20-08)30abc	35°05'30"	111°35'10"	09-06-82	150.0	6,670
Do.	Do.	do.	do.	do.	06-07-95	130.0	6,690
23	LMO-2	(A-20-08)29bbb	35°05'32"	111°34'43"	04-11-85	260.0	6,605
24	Kachina-1	(A-20-07)30bbc	35°05'33"	111°42'05"	04-14-94	628.5	6,046
25	Garrison	(A-20-08)30abb	35°05'35"	111°35'15"	11-11-72	260.0	6,540
26	LM-6	(A-20-08)27bbb	35°05'37"	111°32'32"	09-01-81	990.0	5,820
27	LMEX-6	(A-20-07)23dca	35°05'45"	111°37'10"	08-17-95	617.8	6,257
28	LMO-1	(A-20-08)28cca2	35°05'50"	111°34'30"	04-11-85	235.0	6,585
29	LM-8	(A-20-08)28cca	35°05'47"	111°34'30"	02-01-88	313.3	6,506
Do.	Do.	do.	do.	do.	02-01-95	394.0	6,425
30	Kachina-3	(A-20-07)20cca	35°05'47"	111°40'57"	05-12-95	694.3	6,021
31	Suiter	(A-20-08)19dda	35°05'50"	111°34'50"	08-09-95	379.2	6,441
32	LM-5	(A-20-08)20dbc	35°05'53"	111°34'07"	10-01-88	301.9	6,515
33	Schnieder	(A-20-08)19dac	35°05'55"	111°34'59"	04-14-78	273.0	6,522
34	FH-1	(A-20-07)19cbb2	35°05'58"	111°34'05"	09-01-87	697.0	5,993
Do.	Do.	do.	do.	do.	04-11-95	720.4	5,970
35	FH Test Well	(A-20-07)19cbb1	35°06'00"	111°34'05"	08-12-85	635.0	6,055
36	LMO-3	(A-20-08)20acd	35°06'10"	111°34'10"	12-13-85	562.0	6,233
37	FH-4	(A-20-06)24adb	35°06'10"	111°42'25"	06-30-87	678.0	6,082
Do.	Do.	do.	do.	do.	04-11-95	717.5	6,042
38	Potter-1	(A-20-05)24bbd	35°06'16"	111°49'24"	09-09-66	1,096.5	6,144
39	Morrison	(A-20-06)19beb	35°06'25"	111°48'25"	07-14-81	83.0	7,080
Do.	Do.	do.	do.	do.	04-07-94	82.2	7,081
40	LM-4	(A-20-08)19aba	35°06'25"	111°35'05"	02-01-88	347.6	6,461
Do.	Do.	do.	do.	do.	02-01-95	417.0	6,392
41	FH-5	(A-20-06)24abb	35°06'25"	111°42'03"	09-23-87	703.0	6,067
Do.	Do.	do.	do.	do.	04-11-95	752.5	6,017
42	FH-3	(A-20-07)19aba	35°06'26"	111°41'26"	08-30-87	863.0	6,037
Do.	Do.	do.	do.	do.	11-01-96	875.0	6,025
43	Whitley-1	(A-20-08)18cac1	35°06'48"	111°35'27"	07-23-97	516.0	6,209
44	Whitley-2	(A-20-08)18bac	35°06'50"	111°35'35"	04-28-92	620.0	6,200
45	LM-2	(A-20-08)18bcc	35°07'00"	111°35'47"	12-01-86	477.4	6,355
Do.	Do.	do.	do.	do.	11-01-94	542.0	6,290
46	LM-1	(A-20-08)18bbb	35°07'16"	111°35'44"	03-01-89	591.8	6,248
Do.	Do.	do.	do.	do.	11-01-95	597.0	6,243
47	LM-3	(A-20-07)12dab	35°07'36"	111°36'02"	07-01-87	761.2	6,069
Do.	Do.	do.	do.	do.	10-01-94	748.5	6,082
48	WM-9	(A-20-06)11bdc	35°07'45"	111°43'56"	11-07-85	982.0	6,108
Do.	Do.	do.	do.	do.	06-01-95	972.0	6,118
49	WM-8	(A-20-06)11bdd	35°07'50"	111°43'50"	07-14-82	910.0	6,155
50	Roaldstad	(A-20-07)07adb	35°07'55"	111°41'20"	06-07-60	949.0	---
51	WM-11	(A-20-06)11baa	35°08'05"	111°43'50"	08-18-97	1,103.0	6,067
52	WM-7	(A-20-06)11bab	35°08'08"	111°44'01"	02-01-95	1,110.0	6,061
53	Tyrrell	(A-20-07)07aaa2	35°08'10"	111°41'10"	10-19-92	1,063.0	5,907
54	Kimmerly	(A-20-07)07aaa1	35°08'10"	111°41'10"	05-21-85	941.0	6,039
55	Heckathorne	(A-20-07)12bba	35°08'10"	111°36'40"	06-29-65	900.0	5,940
56	North Ranch	(A-20-07)02cca	35°08'25"	111°37'40"	09-11-87	900.0	5,955
Do.	Do.	do.	do.	do.	10-23-96	817.8	6,037
57	Airport Well	(A-20-07)04dac	35°08'28"	111°39'15"	11-08-95	830.3	6,130
58	WM-10	(A-20-06)02bcb	35°08'43"	111°44'17"	04-02-96	1,139.0	6,091
59	WM-6	(A-20-06)02bdb	35°08'49"	111°44'04"	05-01-87	1,132.0	6,069
Do.	Do.	do.	do.	do.	04-19-94	1,121.0	6,080
60	Skunk Canyon	(A-20-07)35aca	35°08'48"	111°38'17"	01-31-96	897.0	6,017
61	WM-5	(A-20-06)02bbb	35°08'55"	111°44'15"	12-08-88	1,108.7	6,077
Do.	Do.	do.	do.	do.	11-01-95	1,119.0	6,067
62	WM-4	(A-21-06)35ccc	35°09'05"	111°44'08"	02-01-96	1,228.0	5,938
63	WM-Test	(A-21-06)34cca	35°09'10"	111°45'05"	11-14-81	Dry	---
64	WM-2	(A-21-06)35ccb	35°09'16"	111°44'08"	02-01-72	1,246.0	5,921
Do.	Do.	do.	do.	do.	02-01-95	1,262.0	5,905
65	WM-1	(A-21-06)35cba	35°09'24"	111°44'01"	12-08-88	1,246.8	5,893
Do.	Do.	do.	do.	do.	04-19-94	1,260.0	5,880
66	WM-3	(A-21-06)35bcc	35°09'35"	111°44'10"	11-01-95	1,234.0	5,896
67	Mtn Dell-1	(A-21-07)32bbc1	35°09'46"	111°40'53"	08-09-95	1,023.5	5,886
68	Mtn Dell-2	(A-21-07)32bbc2	35°09'48"	111°40'52"	05-22-75	975.0	5,925
69	Kohner	(A-21-07)34baa	35°09'50"	111°38'20"	04-12-88	1,138.0	5,797
Do.	Do.	do.	do.	do.	04-12-88	1,138.0	5,784
70	NPS Walnut Canyon	(A-21-08)26dab	35°10'25"	111°30'37"	08-18-70	1,536.0	5,174
Do.	Do.	do.	do.	do.	08-13-97	1,525.2	5,185
71	Flag Ranch	(A-21-06)25bcd	35°10'25"	111°42'52"	10-20-83	1,122.0	5,928
Do.	Do.	do.	do.	do.	08-11-95	1,182.9	5,867
72	Purl	(A-21-07)25bbd	35°10'43"	111°36'37"	11-17-96	1,173.0	5,617
73	LA-1	(A-21-07)26abd	35°10'45"	111°37'05"	10-05-84	1,168.0	5,627
Do.	Do.	do.	do.	do.	11-13-95	1,151.4	5,644
74	LA-2	(A-21-07)26abb	35°10'53"	111°37'12"	07-20-95	1,150.0	5,650
75	Potter-2	(A-21-07)24ccc	35°10'55"	111°36'30"	08-09-79	12.4	6,748
76	LA-3	(A-21-07)23dcc	35°10'58"	111°37'17"	11-13-95	1,218.2	5,627
77	CVWC	(A-21-09)23cba	35°11'15"	111°24'55"	01-03-83	1,206.0	5,064
78	Rio de Flag MW-1	(A-21-07)23cac	35°11'20"	111°38'00"	04-29-96	44.0	6,751
79	Siskan Ranch	(A-21-06)24bcb	35°11'27"	111°43'03"	06-12-96	1,390.0	5,820
80	Roirdan	(A-21-07)20bdb	35°11'30"	111°40'40"	09-19-62	1,220.0	5,750
81	Ponderosa Paper-2	(A-21-07)22ada	35°11'30"	111°37'50"	10-10-67	1,233.0	5,632
82	Hidden Hollow	(A-21-07)19aca	35°11'30"	111°41'16"	01-14-77	1,320.0	5,750
83	Ponderosa Paper-1	(A-21-07)22aad	35°11'35"	111°37'50"	06-25-66	1,273.0	5,582
84	Henden	(A-21-06)23aad	35°11'35"	111°43'10"	09-06-95	1,440.0	5,780
85	Foxglenn-1	(A-21-07)24aad	35°11'37"	111°35'48"	12-21-96	1,319.0	5,456
86	Fried	(A-21-06)22bab	35°11'40"	111°44'55"	11-14-92	Dry	---
87	Porter	(A-21-09)15dda	35°11'55"	111°25'05"	01-01-65	1,215.0	5,050
88	Pill	(A-21-09)14acc	35°12'10"	111°24'30"	06-24-66	1,205.0	5,065
89	ADOT-Winona	(A-21-09)17acc	35°12'15"	111°27'40"	08-08-79	1,323.0	5,117
Do.	Do.	do.	do.	do.	08-08-95	1,314.1	5,126
90	Continental-2	(A-21-08)17bca2	35°12'23"	111°34'28"	02-22-97	1,303.5	5,446
91	Continental-1	(A-21-08)17bca1	35°12'24"	111°34'27"	10-21-96	[1]1,550.0	5,200
92	NAD-1	(A-21-05)11cbc	35°12'45"	111°50'30"	08-28-50	1,273.0	5,767
Do.	Do.	do.	do.	do.	09-10-95	1,303.1	5,737
93	Burns	(A-21-06)10daa	35°13'00"	111°44'15"	05-26-87	[2]1,275.0	---
94	BBDP-Cosnino	(A-21-09)08bcc	35°13'05"	111°28'10"	07-18-90	1,338.0	5,112
Do.	Do.	do.	do.	do.	03-12-97	1,333.0	5,117
95	Ritland	(A-21-07)09acc	35°13'05"	111°39'25"	02-09-91	1,516.0	5,494
96	Wilbur	(A-21-09)10dbd	35°13'20"	111°26'00"	07-30-66	1,227.0	5,063
97	Pugh	(A-21-07)09bac	35°13'22"	111°39'37"	06-30-89	1,530.0	5,570
Do.	Do.	do.	do.	do.	08-09-95	1,505.2	5,595
98	Foster	(A-21-09)11bbb	35°13'25"	111°25'00"	04-09-90	1,137.0	5,068
99	BBDP-Flowers	(A-21-09)05ddd	35°13'30"	111°27'15"	07-21-75	1,270.0	5,095
Do.	Do.	do.	do.	do.	05-01-95	1,269.0	5,096
100	Crockett	(A-21-05)01acc3	35°13'55"	111°48'50"	04-20-94	97.2	7,037
101	BBDP-MVR-1	(A-21-09)06baa	35°14'16"	111°28'50"	08-08-95	1,264.2	5,146
102	Garrett-Bacon	(A-22-07)34dda	35°14'33"	111°37'54"	09-25-97	1,920.0	5,290
103	Mitchell	(A-22-08)35aac	35°15'10"	111°30'35"	06-20-66	1,456.7	5,103
104	EPNG-6	(A-22-05)26adc2	35°15'35"	111°49'40"	08-01-53	2,010.0	5,220
105	EPNG-5	(A-22-05)26acd	35°15'35"	111°49'50"	07-01-53	2,120.0	5,110
106	Koch Field	(A-22-08)27caa	35°15'40"	111°33'05"	05-01-94	1,496.0	5,129
107	US Grisp	(A-22-09)29baa	35°16'00"	111°27'50"	12-17-73	1,383.0	5,007
108	Hart Valley	(A-22-06)26aaa	35°16'06"	111°46'08"	02-23-88	Dry	---
109	Cromer School	(A-22-08)26bbb	35°16'08"	111°31'18"	01-22-86	1,463.0	5,122
110	BBDP-Marijka	(A-22-08)23aab	35°16'56"	111°30'52"	06-25-88	1,500.0	5,075
Do.	Do.	do.	do.	do.	05-01-94	1,502.0	5,073
111	BBDP-Sunset	(A-22-08)23aab	35°17'00"	111°30'55"	12-05-86	1,507.0	5,063
Do.	Do.	do.	do.	do.	05-01-94	1,507.0	5,063
112	AT&T	(A-22-08)16dad	35°17'28"	111°32'35"	06-12-63	1,635.0	5,115
113	IB-9	(A-23-07)33aab2	35°20'27"	111°35'00"	09-15-73	143.2	9,637
114	NPS Sunset Ctr-2	(A-23-08)21aad	35°22'05"	111°32'35"	01-31-79	1,960.3	5,010
Do.	Do.	do.	do.	do.	10-02-98	1,962.6	5,007
115	AZWC-5	(A-18-07)15ccc2	34°56'16"	111°38'54"	01-09-81	706.9	5,728
116	Bradshaw Fee-1	(A-18-04)34abb	34°54'14"	111°55'32"	08-22-74	329.2	4,151
117	Drye	(A-21-11)19bcb	35°11'45"	111°16'10"	04-04-78	796.0	4,974
118	Moody	(A-21-10)18dac	35°12'10"	111°25'15"	11-30-78	990.0	5,015
119	Kutlkuhn	(A-22-10)15bdc	35°17'40"	111°19'10"	07-01-75	1,112.0	4,593
120	Salt Well	(A-22-11)19ccc	35°16'25"	111°16'20"	10-20-54	1,000.0	4,590
121	NPS Wupatki HQ	(A-25-10)30bdb	35°31'10"	111°22'20"	10-27-58	781.0	4,149
Do.	Do.	do.	do.	do.	05-26-98	782.6	4,152
122	NPS-Citadel	(A-25-09)06ccd	35°34'10"	111°28'45"	01-23-67	1,582.9	3,798
Do.	Do.	do.	do.	do.	02-21-97	1,587.2	3,794
123	Oil test	(A-22-10)03acd	35°19'30"	111°18'45"	10-05-66	1,138.0	4,452
124	Rhoten Spr.	(A-23-10)01bbb	35°25'05"	111°17'20"	10-19-54	740.0	4,283

[1] Well caved in and collapsed before water level stabilized.
[2] Well obstructed.

gallons per day

Hydrogeologic data for wells that discharge water from the regional aquifer, Flagstaff, Arizona

[Wells are in order by well-reference number. Dashes indicate no data. >, greater than. CS, Coconino Sandstone; SG, Supai Group; KF, Kaibab Formation; SH, Schnebly Hill Formation]

Well-reference number	Local well name	Site identifier	Latitude	Longitude	Year test	Well yield, in gallons per minute	Drawdown, in feet	Saturated thickness, in feet	Screened interval, in feet	Pumping period, in days	Recovery period, in days	Transmissivity, in gallons per day per foot: Drawdown	Transmissivity, in gallons per day per foot: Recovery	Hydrologic conductivity- in gallons per day per foot squared: Drawdown	Hydrologic conductivity- in gallons per day per foot squared: Recovery	Storativity, dimensionless	Specific yield	Porosity	Specific capacity, in gallons per minute per foot	Lithology of saturated zone	Surface strike of principal structure
2	Pine Grove	(A-19-09)17dcd	35°01'24"	111°27'35"	1967	50.0	---	391	261	---	---	---	---	---	---	---	---	---	0.6	SG	---
Do.	Do.	do.	do.	do.	1967	15	25	---	---	0.66	---	---	---	---	---	---	---	---	---	---	---
4	ADOT-89A	(A-19-06)W14bab	35°02'00"	111°43'55"	1978	51.0	0	275	200	2.00	---	---	---	---	---	---	---	---	---	SG	---
5	LMEX-1	(A-19-08)05ddd1	35°03'05"	111°33'50"	1992	330	83.0	1,008	889	.50	.50	2,500	2,680	2.81	2.92	---	---	---	3.98	CS, SG	---
6	Federal 1	(A-19-07)01ddd1	35°03'06"	111°35'55"	1992	270	74.0	360	825	.50	.50	1,500	1,800	4.62	5.54	---	---	---	3.65	KF, CS, SG	---
10	LMEX-2	(A-20-08)33cdb	35°04'05"	111°33'20"	1992	69.0	63.0	749	719	.50	.50	800	700	1.11	.97	---	---	---	1.10	CS, SG	---
11	LMEX-3	(A-20-08)32cab1	35°04'15"	111°34'25"	1992	320	270.0	1,141	934	.50	.50	600	300	.64	.32	---	---	---	1.18	CS, SG	N.60°W.
13	LM-9	(A-20-08)30dca	35°04'51"	111°35'25"	1991	220	74.0	360	825	.50	10.0	940	1,200	.73	.93	---	---	---	.82	CS, SG	N.54°W.
14	TH-3	(A-20-08)30cdd1	35°04'56"	111°35'25"	1992	---	56.0	1,079	45	10.0	10.0	3,350	3,974	3.10	3.68	0.01 to 0.03	---	---	---	KF, CS, SG	---
15	LMEX-4	(A-20-07)25dcb1	35°04'55"	111°36'15"	1992	100	251.0	900	720	.10	.10	100	100	.14	.14	---	---	---	.40	CS, SG	---
20	Kachina-2	(A-20-07)30bdb	35°05'16"	111°41'50"	1969	55.0	35.0	372	---	.20	---	---	---	---	---	---	---	---	1.60	CS	---
21	Whalers	(A-20-08)30bdb	35°05'20"	111°35'30"	1985	15.0	60.0	85	100	---	---	---	---	---	---	---	---	---	.25	KF, CS	---
24	Kachina-1	(A-20-07)30bbc	35°05'33"	111°42'05"	1978	34.0	20.0	452	210	.08	---	---	---	---	---	---	---	---	1.70	CS, SG	---
27	LMEX-6	(A-20-07)23dca	35°05'45"	111°37'10"	1992	57.0	60.0	531	892	.50	.50	400	500	.75	.94	---	---	---	.95	CS, SG	---
28	LMO-1	(A-20-08)20cca2	35°05'50"	111°34'30"	1992	---	38.0	659	300	---	84.0	17,000	16,000	28.8	24.3	.05	---	---	---	KF, CS	---
29	LM-8	(A-20-08)20cca	35°05'47"	111°34'30"	1992	1,700	285.0	914	700	90.0	90.0	26,000	24,000	---	28.0	---	---	0.095 to 0.14	6.00	CS, SG	N.13°W.
31	Suiter	(A-20-08)19dda	35°05'50"	111°34'50"	1990	10.0	40.0	113	---	---	---	---	---	---	---	---	---	---	.25	CS	---
32	LM-5	(A-20-08)20dbc	35°05'53"	111°34'07"	1992	485	178.0	929	675	90.0	90.0	3,000	3,000	---	4.00	---	---	---	2.70	CS, SG	N.76°W.
34	FH-1	(A-20-07)19cbb2	35°05'58"	111°42'05"	1986	110	205.0	555	525	9.70	9.70	[2]2,904	[2]3,630	5.23	6.54	.00023	0.0002	---	.54	SH, SG	N.53°W.
37	FH-4	(A-20-06)24adb	35°06'10"	111°42'25"	1987	152	234.0	577	545	1.50	---	[2]747	---	1.29	---	---	---	---	.65	CS, SH, SG	N.53°W.
40	LM-4	(A-20-08)19aba	35°06'25"	111°35'05"	1992	620	288.0	937	480	90.0	90.0	20,000	11,690	21.3	8.50	115	---	---	2.20	CS, SG	N.68°W; N.42°W.
41	FH-5	(A-20-06)24abb	35°06'25"	111°42'03"	1987	220	274.0	647	625	4.00	.05	2,159	1,930	3.30	3.04	---	---	---	.80	CS, SG	N.53°W.
43	FH-3	(A-20-07)19aba	35°06'26"	111°41'26"	1987	90.0	245.0	547	520	3.10	---	[2]456	---	.83	---	---	---	---	.37	CS, SH, SG	---
44	Whitley-2	(A-20-08)18cac2	35°06'50"	111°35'35"	1992	35.0	20.0	590	640	---	---	---	---	---	---	---	---	---	1.80	CS	---
45	LM-2	(A-20-08)18bcc	35°07'00"	111°35'47"	1992	430	346.0	523	512	90.0	90.0	---	4,000	---	6.00	---	---	---	1.24	CS	N.68°W.
46	LM-1	(A-20-08)18bbb	35°07'16"	111°35'44"	1963	500	276	700	108	7.63	15.4	[2]1,386	---	1.98	2.77	---	---	---	1.81	CS	N.67°W.
Do.	LM-1 redevelopment	do.	do.	do.	1996	300	267	540	439	.5	1.04	---	444.9	---	.82	---	---	---	---	---	---
47	LM-3	(A-20-07)12dab	35°07'36"	111°36'02"	1966	167	211.0	281	317	1.50	.90	1,000	1,000	3.60	3.60	---	---	---	.79	CS	N.64°W.
48	WM-9	(A-20-06)11bdc	35°07'45"	111°43'56"	1986	677	471.0	858	610	4.67	.16	2,201	---	2.56	---	---	---	---	1.43	KF, CS, SG	N.24°W.
51	WM-11	(A-20-06)11baa	35°08'05"	111°43'50"	1998	491	249	844	702	3.25	.19	3,700	7,200	5.48	4.87	---	.13	1.97	1.97	CS, SH, SG	N.24°W.
52	WM-7	(A-20-06)11bab	35°08'08"	111°44'01"	1978	727	308.5	680	640	18.2	1.80	18,300	35,000	28.6	54.7	---	.14	.20 to .50	4.60	CS, SG	N.24°W.
53	Tyrrell	(A-20-07)07aaa2	35°08'10"	111°41'10"	1993	10.0	12.0	212	----	---	---	---	---	---	---	---	---	---	.83	CS	N.50°W.
56	North Ranch	(A-20-07)02cca	35°08'25"	111°37'40"	1987	40.0	20.0	240	----	---	---	---	---	---	---	---	---	---	2.00	SG	N.60°W.
58	WM-10	(A-20-06)02bcb	35°08'43"	111°44'17"	1996	121	250.0	640	460	3.00	.30	4,460	4,013	6.97	6.27	---	.08	---	1.28	CS, SG	N.24°W.
59	WM-6	(A-20-06)02bdb	35°08'47"	111°44'04"	1972	560	365.5	584	600	208	150	8,400	15,100	14.4	25.8	---	---	---	1.53	CS	N.24°W.; N.83°W.
60	Skunk Canyon	(A-20-07)03aca	35°08'48"	111°38'17"	1996	150	669.0	884	800	1.00	1.00	[2]237	373	.27	.42	---	---	---	.22	CS, SH, SG	N.56°W.; N.30°W.
61	WM-5	(A-20-06)02bbb	35°08'55"	111°44'15"	1972	400	82.2	500	550	24.0	114	31,200	30,750	62.4	61.4	---	.08	---	4.87	CS	N.83°W.; N.24°W.
62	WM-4	(A-21-06)35ccc	35°09'05"	111°44'08"	1972	436	283.0	410	304	193	150	5,700	8,600	13.9	20.9	---	---	---	1.54	CS	N.24°W.
64	WM-2	(A-21-06)35ccb	35°09'16"	111°44'08"	1972	295	64.8	375	300	185	150	18,150	21,850	48.4	58.3	---	---	---	4.56	CS	N.24°W.
65	WM-1	(A-21-06)35cba	35°09'24"	111°44'01"	1972	---	13.1	363	360	208	127	29,600	28,700	81.5	79.1	---	.08	---	---	CS	N.24°W.
66	WM-3	(A-21-06)35bcc	35°09'35"	111°44'10"	1979	403	81.4	385	300	168	150	14,500	20,000	37.7	51.9	---	---	---	4.95	CS	N.24°W.
67	Mtn Dell-1	(A-21-07)32bbc1	35°09'46"	111°40'53"	1976	206	200.0	215	1,050	.004	.03	---	---	---	---	---	---	---	1.03	CS, SG	N.73°W.
70	NPS Walnut Canyon	(A-21-08)26dab	35°10'25"	111°30'37"	1970	36.0	252.5	444	514	.70	.91	[2]204	---	.46	---	---	.098	---	.14	SG	---
71	Flag Ranch	(A-21-06)25bcd	35°10'25"	111°42'52"	1983	86.0	287.0	626	590	1.00	---	---	---	---	---	---	---	---	.30	SG	N.70°W.; N.63°W.
72	Purl	(A-21-07)25bbd	35°10'43"	111°36'37"	1990	8.00	0	155	160	---	---	---	---	---	---	---	---	---	---	CS, SH, SG	---
73	LA-1	(A-21-07)26abd	35°10'45"	111°37'05"	1975	101	30.1	322	274	4.84	.98	[2]4,504	---	13.99	---	---	---	---	3.36	SG	N.59°W.
77	CVWC	(A-21-09)23cba	35°11'15"	111°24'55"	1983	7.00	---	69	70	---	---	---	---	---	---	---	---	---	---	SG	---
79	Saskan Ranch	(A-21-06)24bcb	35°11'27"	111°43'03"	1997	17.0	53.0	287	140	1.10	.10	[2]444	---	1.55	---	---	---	---	.32	SH, SG	---
80	Roirdan	(A-21-07)20bdb	35°11'30"	111°40'40"	1962	30.0	---	400	395	---	---	---	---	---	---	---	---	---	---	SG	---
82	Hidden Hollow	(A-21-07)19aca	35°11'30"	111°41'16"	1977	10.0	---	231	231	---	---	---	---	---	---	---	---	---	---	SG	---
84	Henden	(A-21-06)23aad	35°11'35"	111°43'10"	1994	15.0	0	110	120	1.50	---	---	---	---	---	---	---	---	---	CS, SG	---
85	Foxglenn-1	(A-21-07)24aad	35°11'37"	111°35'48"	1997	450	168.0	691	1,135	3.05	3.45	2,536	2,343	3.67	3.99	---	---	---	2.68	SG	N.8°W.; N.42°W.
88	Pill	(A-21-09)14acc	35°12'10"	111°24'30"	1966	7.50	8.80	112	120	.09	.02	[2]818	---	1.30	---	---	---	---	.85	CS	---
89	ADOT-Winona	(A-21-09)17acc	35°12'15"	111°27'40"	1972	18.0	150.0	512	448	.99	---	[2]143	---	.28	---	---	---	---	.12	SG	---
90	Continental-2	(A-21-08)17

[Latitude and longitude are in degrees, minutes, and seconds and referenced to NAD 83; ft, feet; ft bls, feet below land surface; NA, information not available]

Bureau of Reclamation well designation	Station number	Latitude	Longitude	Distance from pumping well (ft)	Land-surface altitude (ft above NAVD 88)	Hole depth (ft bls)	Static water level (ft bls)	Date	Preforations	
									Top (ft bls)	Bottom (ft bls)
				Site 1						
PW-1A	351023111062002	35°10'24.31"	111°06'23.26"	0	5,379.39	1,134	611.42	02/17/2005	837	1,077
OW-1	351022111061801	35°10'21.75"	111°06'21.63"	290	5,381.57	1,179	614.82	02/10/2005	686	1,086
5T-533		35°10'21.97"	111°06'27.76"	415	5,385.3	802	615.2	02/17/2005	597	792
				Site 2						
PW-2A		35° 12' 18.48"	111° 02' 17.05"	687	5,021.49	1,096	321.55	03/08/2005		
PW-2B	351213111022101	35° 12' 13.32"	111° 02' 22.45"	0	5,030.13	1,096	330.95	04/20/2005	576.5	996.5
OW-2A (deep)		35° 12' 16.33"	111° 02' 19.32"	402	4,985.28	1,140	323.16	02/11/2005	1,100	1,120
OW-2A (middle)		35° 12' 16.33"	111° 02' 19.32"	402	4,985.28	1,140	323.24	02/11/2005	661	681
OW-2A (shallow)		35° 12' 16.33"	111° 02' 19.32"	402	4,985.28	1,140	323.25	02/11/2005	400	420
OW-2	351214111022101	35° 12' 14.38"	111° 02' 24.11"	178	5,029.13	1,068	328.33	04/18/2005	698	998
5M-94	351215111021701	35° 12' 15.18"	111° 02' 20.35"	251	5,027.45	388	327.82	01/29/2005	Open from 163 to 388	
				Site 3						
PW-3	350958110562201	35°09'55.84"	110°56'25.55"	0	4,909.27	1,128	225.5	02/09/2005	696	1,076
OW-3A (deep)	350959110562302	35°09'57.2"	110°56'22.54"	248	4,882.25	755	225.98	02/04/2005	694	714
OW-3A (shallow)	350959110562303	35°09'57.2"	110°56'22.54"	248	4,882.25	755	225.68	02/04/2005	250	270
OW-3C (deep)		35°09'57.59"	110°56'19.91"	474	4,880.57	1,180	226.64	02/17/2005	1,150	1,170
OW-3C (middle)		35°09'57.59"	110°56'19.91"	474	4,880.57	1,180	226.45	02/17/2005	680	700
OW-3C (shallow)		35°09'57.59"	110°56'19.91"	474	4,880.57	1,180	226.38	02/17/2005	240	260
5M-88	351001110562601	35°10'0.59"	110°56'28.61"	547	4,903.74	425	222.63	02/11/2005	Open from 388 to 425	
Sunshine	350706111014701	35007'05.52"	111001'49.15"	NA	5,351.94	1,155	562.04	02/26/2005	NA	

Table A-2: Locations and selected construction data for wells near Leupp, Arizona. From Hoffman et al. (2006).

Estimated hydraulic properties from numerical-model simulations at test-well sites 1, 2, and 3 near Leupp, Arizona

[(gal/min)/ft, gallons per minute per foot of drawdown; ft^2/d, foot squared per day; ft/d, foot per day; NC, not calculated; ft-1, per foot. Specific-capacity values were determined during constant-rate aquifer test]

Hydraulic property	Site 1	Site 2	Site 3
Specific capacity, (gal/min)/ft	2	7.5	2.4
Transmissivity, ft^2/d	7,000	18,000	5,400
Hydraulic conductivity of Coconino Sandstone, ft/d	28	42	11
Hydraulic conductivity of Schnebly Hill Formation, ft/d	NC	.5	.2
Hydraulic conductivity of interfingered of the Coconino Sandstone/Schnebly Hill Formation, ft/d	8	.04	.9
Hydraulic conductivity of Upper Supai Formation, ft/d	[1].1	NC	.2
Specific yield, dimensionless	.06	.08	.05
Specific storage, ft-1	$2x10^{-6}$	$2x10^{-6}$	$2x10^{-6}$
Vertical-to-horizontal anisotropy, dimensionless	.5	[1].2	.17

[1]Estimated on the basis of results from site 3.

Table A-3: Estimated hydraulic properties from numerical-model simulations for wells near Leupp, Arizona. From Hoffman et al. (2006).

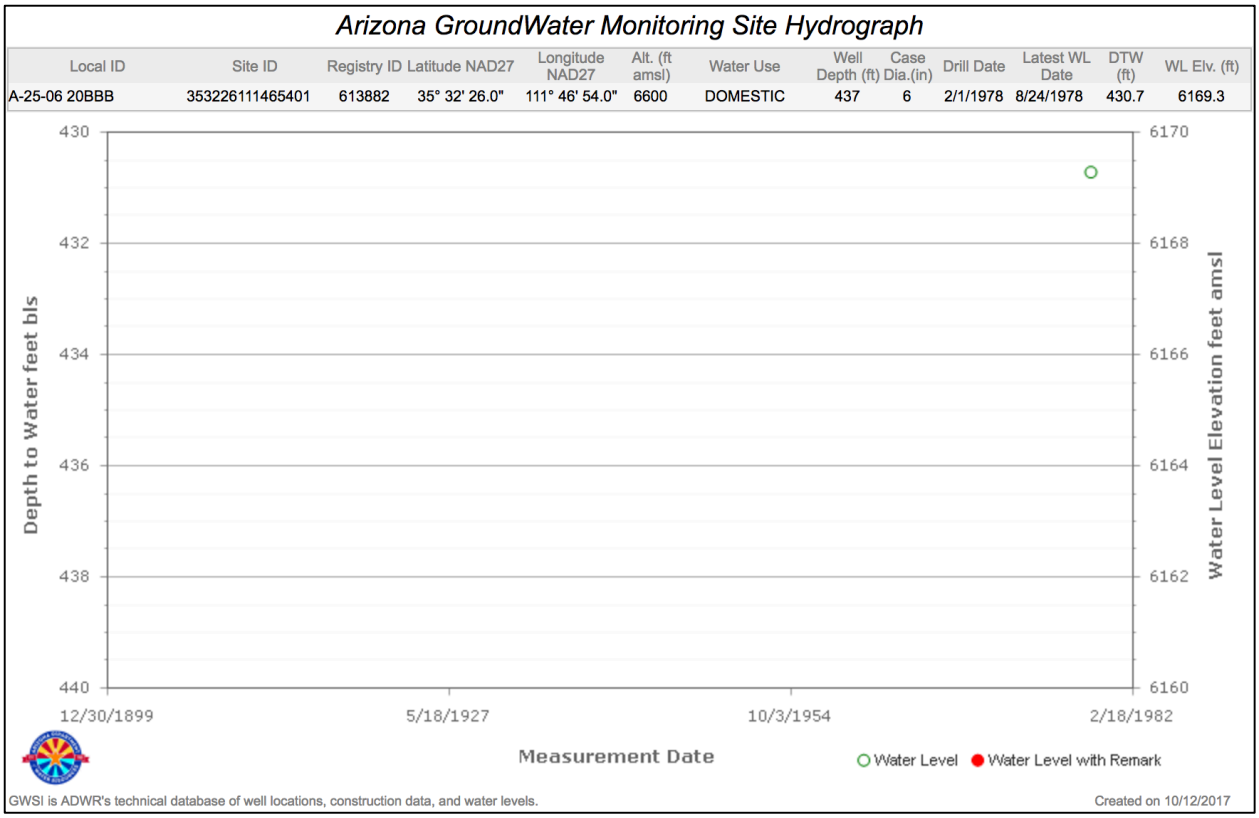

Figure A-2: Hydrograph showing depth to groundwater at a well ~12.5 km west of Colton Crater. From ADWR (2017).

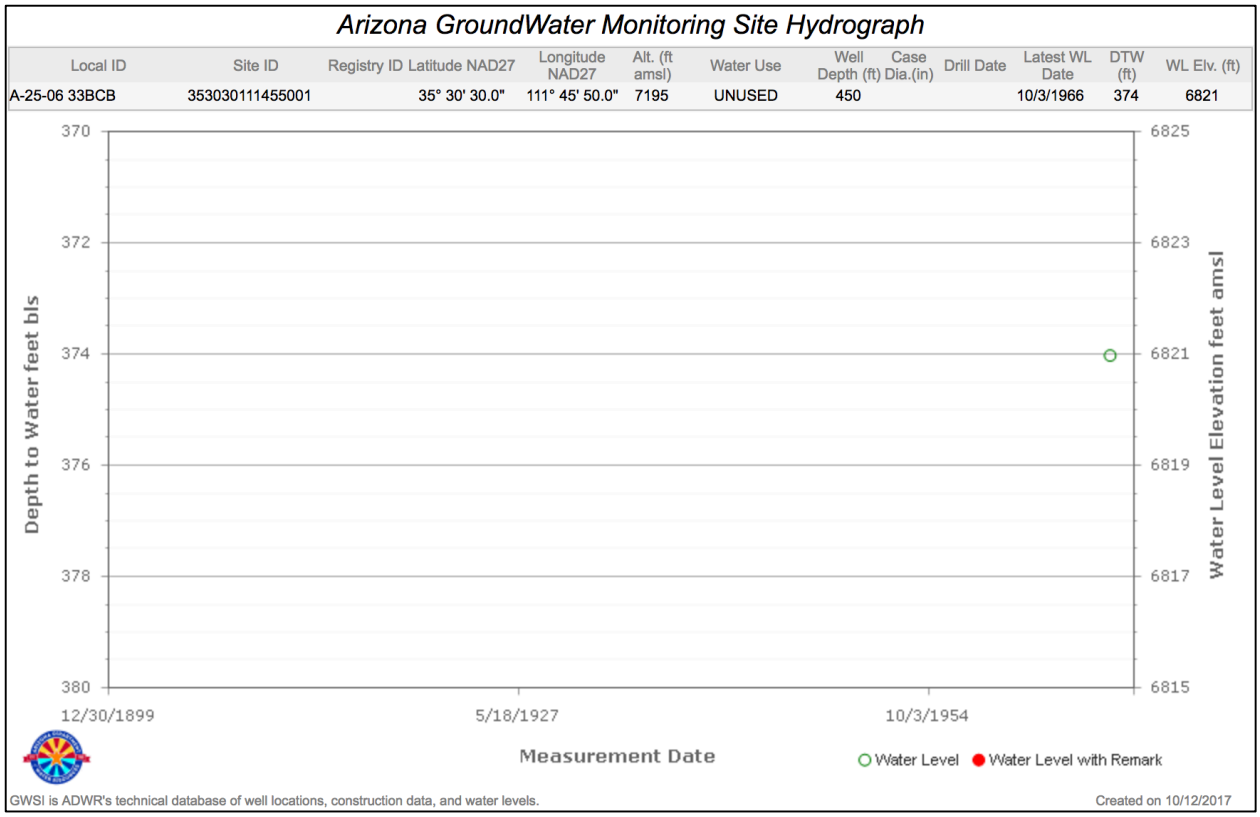

Figure A-3: Hydrograph showing depth to groundwater for a well ~12.9 km WSW of Colton Crater. From ADWR (2017).

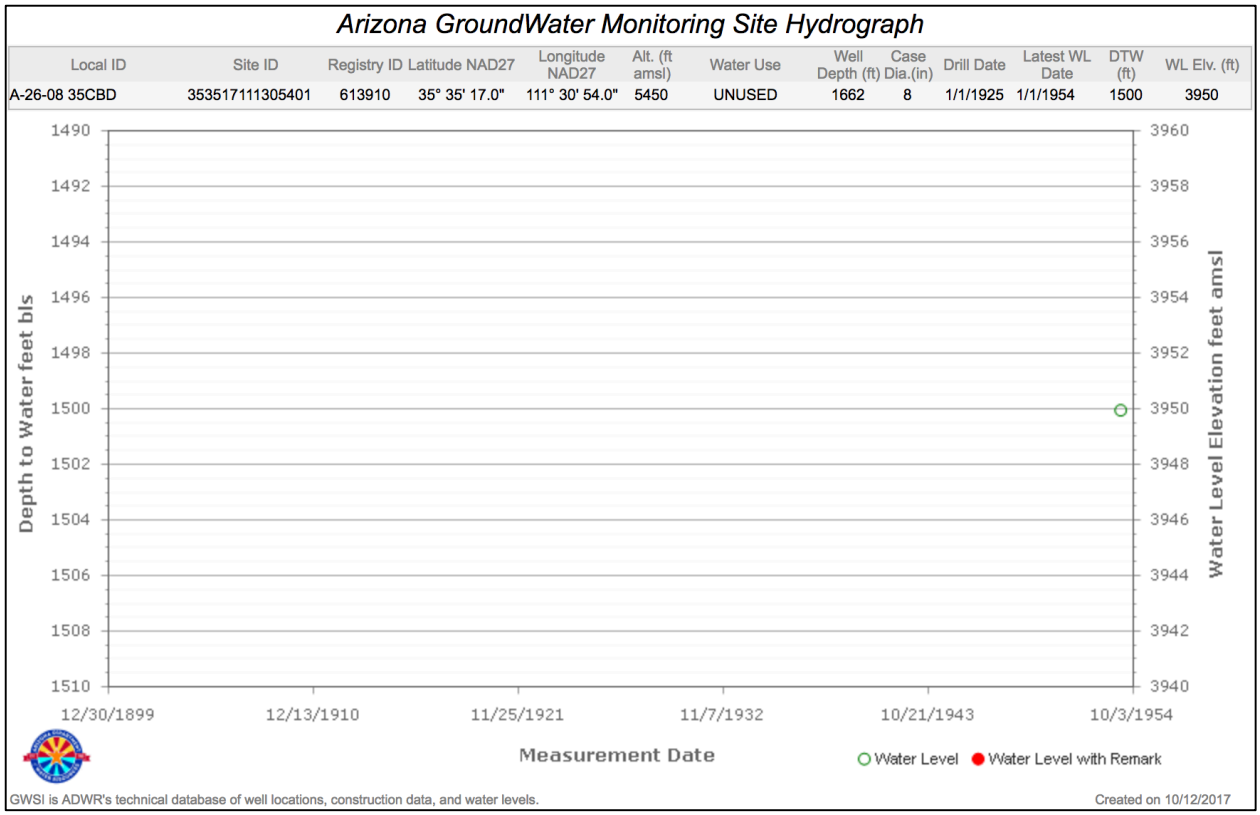

Figure A-4: Hydrograph showing depth to groundwater for a well ~11.3 km ENE of Colton Crater. From ADWR (2017).

DEPARTMENT OF WATER RESOURCES
99 EAST VIRGINIA AVENUE
PHOENIX, ARIZONA 85004

REGISTRATION OF EXISTING WELLS

READ INSTRUCTIONS ON BACK OF THIS FORM BEFORE COMPLETING
PRINT OR TYPE – FILE IN DUPLICATE

03

FOR OFFICE USE ONLY
REGISTRATION NO. 55- 801678
FILE NO. A(21-10)16 BDC
FILED 8/21/84 (DATE) AT PM (TIME)
INA —
AMA —

REGISTRATION FEE (CHECK ONE)
EXEMPT WELL (NO CHARGE) ☐
NON-EXEMPT WELL – $10.00 ☐

LATE FEE $10.00 ☐

1. Name of Registrant:
WILLIAM F MOODY
1345 E OCOTILLO (Address) PHX (City) AZ (State) 85016 (Zip)

2. File and/or Control Number under previous groundwater law:
_____ (File Number) 35- _____ (Control Number)

3. a. The well is located within the SW ¼ SE ¼ NW ¼, Section 16, of Township 21 N/~~S~~ Range 10 E/~~W~~ G & SRB & M, in the County of COCONINO.

b. If in a subdivision: Name of subdivision _____, Lot No. _____, Address _____.

4. The principal use(s) of water (Examples: irrigation - stockwater - domestic - municipal - industrial)
STOCK WATER & DOMESTIC.

5. If for irrigation use, number of acres irrigated from well _____.

6. Owner of land on which well is located. If same as Item 1, check this box ☒
_____
_____ (Address) (City) (State) (Zip)

7. Well data (If data not available, write N/A)
a. Depth of Well 1,080 feet
b. Diameter of casing 8 inches
c. Depth of casing NA feet
d. Type of casing NA .
e. Maximum pump capacity (15 HP) gallons per minute.
f. Depth to water 1040 feet below land surface.
g. Date well completed NA (Month) (Day) 1959 (Year).

8. The place(s) of use of water. If same as Item 3, check this box ☒
____¼ ____¼ ____¼, Section ____ Township _____ Range _____
____¼ ____¼ ____¼, Section ____ Township _____ Range _____
Attach additional sheet if necessary.

9. DATE 8/21/84 SIGNATURE OF REGISTRANT Robert B Moody

Figure A-5: Registration form showing depth to groundwater at a well <1.5 km SW of Rattlesnake Crater.

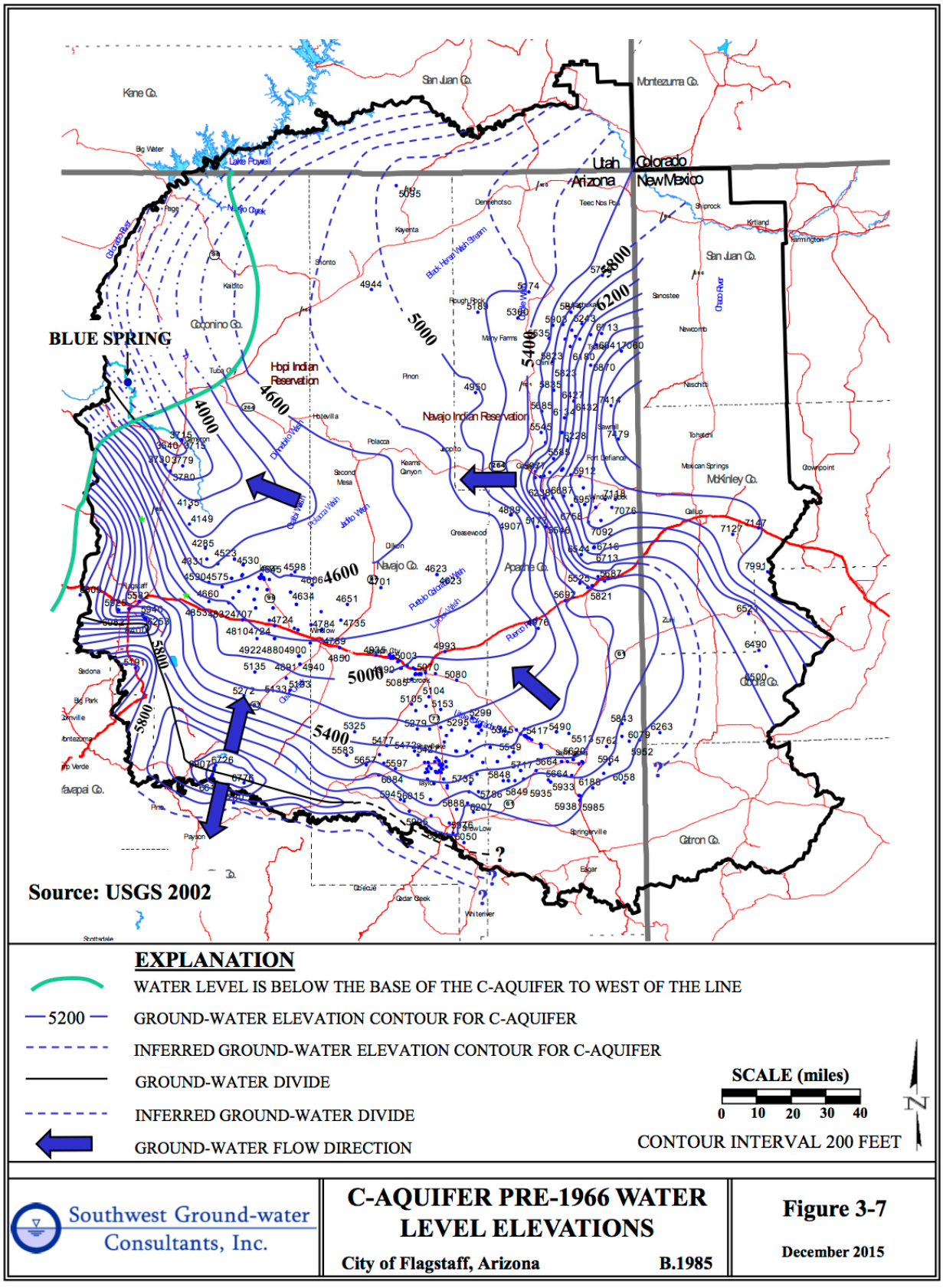

Figure A-6: Potentiometric surface map of the C-Aquifer prior to 1966. From SGC (2015).

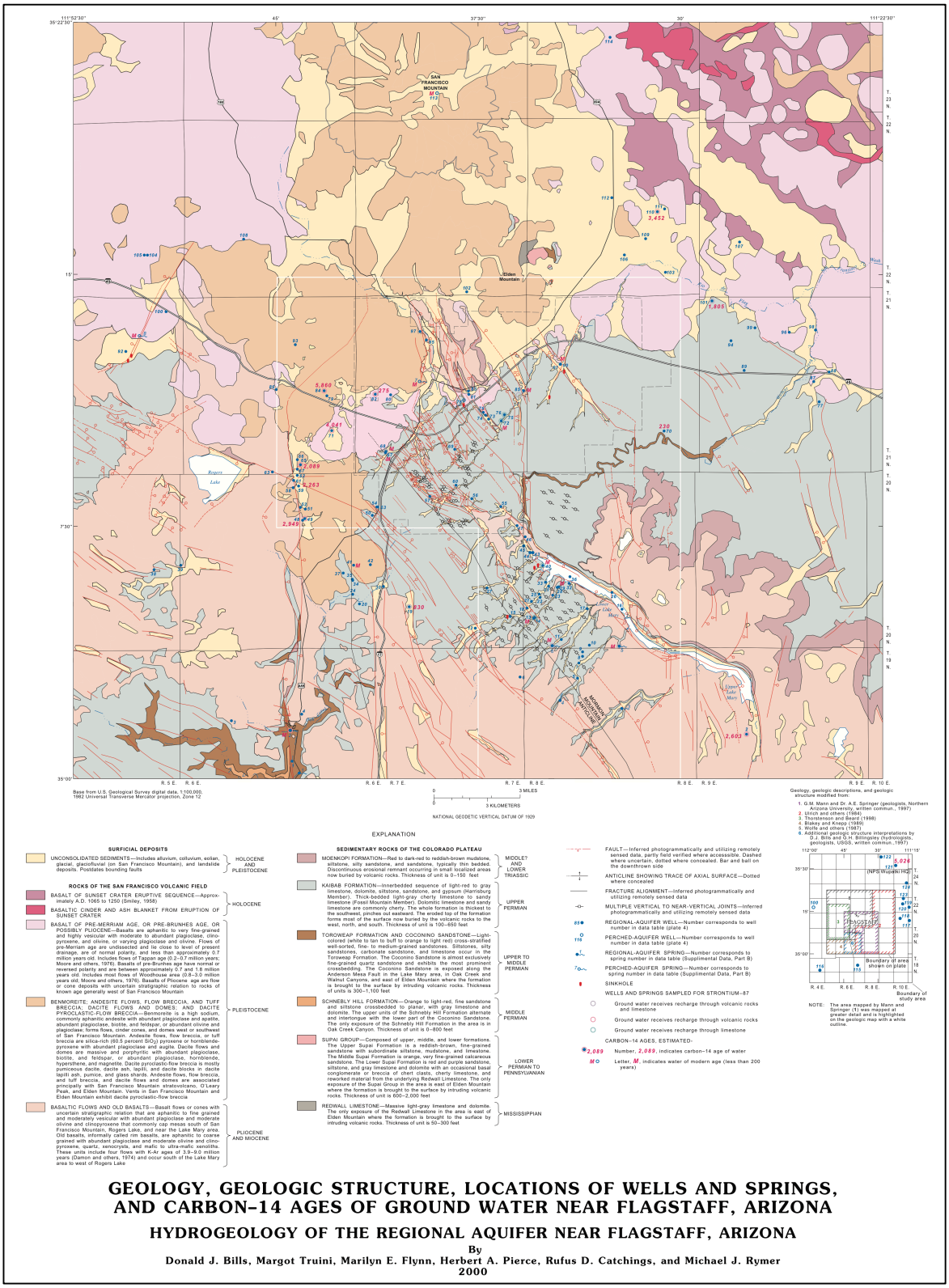

Figure A-7: Geology, Geologic Structure, Locations of Wells and Springs, and Carbon-14 Ages of Ground Water near Flagstaff, Arizona. From Bills et al. (2000).

APPENDIX B

FIELD DATA

Table B-1: Fracture measurement data for Coconino Sandstone outcrop in Walnut Canyon, Arizona.

Fracture Data: Coconino Sandstone, Walnut Canyon												
Outcrop	Strike	Dip	Length (cm)	Aperture				Fracture Permeability				Notes
				Range (in)	Min (cm)	Max (cm)	Avg (cm)	min (cm^2)	max (cm^2)	avg (cm^2)	avg (m^2)	
RC1	125	25	--	0.2-0.5	0.51	1.27	0.89	0.02	0.13	0.07	6.59E-06	A 1- Horizontal bedding plane/ fracture
A	129	63	--	0.4-0.6	1.02	1.52	1.27	0.09	0.19	0.13	1.34E-05	2- Intersecting vertical fracture
	139	65	391.16	0.3	--	--	0.76	--	--	0.05	4.84E-06	3- Vertical fracture
10/12/16	94	6	--	0.6-1.2	1.52	3.05	2.29	0.19	0.77	0.44	4.35E-05	4- Horizontal bedding plane/ fracture; top of unit
Sunny, clear	135	65	30.48	0-0.2	0.00	0.51	0.25	0.00	0.02	0.01	5.38E-07	5- Vertical branching
	111	87	--	0.2-0.3	0.51	0.76	0.64	0.02	0.05	0.03	3.36E-06	6- Vertical Unit Continues; 2-3 in. variable weathering
	94	85	--	0-7.5	--	--	19.05	--	--	30.24	3.02E-03	7- Vertical heavily eroded; Closing upward
RC2												B- Heavily eroded, multiple fractures in 12ft wide section
B	100	84	--	0.1-0.3	0.25	0.76	0.51	0.01	0.05	0.02	2.15E-06	1- Vertical closed
	--	--	--	6.0-11.0	15.24	27.94	21.59	19.35	65.05	38.84	3.88E-03	2- Vertical (top 6-11 in.)
	103	90	220.98	0.1-0.6	0.25	1.52	0.89	0.01	0.19	0.07	6.59E-06	2A
	104	89	220.98	0.2-0.6	0.51	1.52	1.02	0.02	0.19	0.09	8.60E-06	2B
	90	89	--	0.1	--	--	0.25	--	--	0.01	5.38E-07	3
	95	84	50	4.5	--	--	11.43	--	--	10.89	1.09E-03	4a- Iron alteration
	95	84	--	0.2-0.4	0.51	1.02	0.76	0.02	0.09	0.05	4.84E-06	4b
	101	83	57.6	0.1	--	--	0.25	--	--	0.01	5.38E-07	5A- vertical; iron alteration
	101	83	--	1.0-1.5	2.54	3.81	3.18	0.54	1.21	0.84	8.40E-05	5A-2
	105	86	--	0.1-0.2	0.25	0.51	0.38	0.01	0.02	0.01	1.21E-06	5B
RC3	80	60	33.02	0.1	--	--	0.25	--	--	0.01	5.38E-07	C 1- Vertical
C	65	54	116.84	0.05-0.1	0.13	0.25	0.19	0.00	0.01	0.00	3.02E-07	2- Vertical
	74	70	88.9	0.05-0.1	0.13	0.25	0.19	0.00	0.01	0.00	3.02E-07	3A- Vertical
	105	66	64.77	0-0.1	0.00	0.25	0.13	0.00	0.01	0.00	1.34E-07	3A- Vertical
	64	58	104.14	0.05-0.1	0.13	0.25	0.19	0.00	0.01	0.00	3.02E-07	C 4- Vertical
	48	--	22.86	0.05-0.1	0.13	0.25	0.19	0.00	0.01	0.00	3.02E-07	4A- Vertical
	82	23	27.94	0-0.1	0.00	0.25	0.13	0.00	0.01	0.00	1.34E-07	5- Horizontal
	87	37	82.55	0-0.05	0.00	0.13	0.06	0.00	0.00	0.00	3.36E-08	6- Horizontal
	102	26	25.4	0.05	--	0.13	0.13	--	0.00	0.00	1.34E-07	7-Horizontal
RC4	110	83	--	240	--	--	609.60	--	--	--	--	D- Large open vertical with trees (high uncertainty)
D	104	90	--	3.5-6.5	8.89	16.51	12.70	6.59	22.72	13.44	1.34E-03	1
	104	90	--	4	--	--	10.16	--	--	8.60	8.60E-04	
Strike/Dip min:	48	6				Aperture min:	0.00			Average k min:	3.36E-08	
Max:	139	90				Max:	27.94			Max:	3.88E-03	
Average:	98.2	70				Average:	3.20			Average:	3.71E-04	
Mode:	104	84				Mode:	0.25			Mode:	5.3763E-07	

Table B-2: Fracture measurement data for Kaibab Limestone outcrops near Colton Crater, Arizona. Gray indicates uncertainty in measurement or recording.

Fracture Data: Kaibab Limestone near Colton Crater											
Outcrop	Strike	Dip	Length (cm)	Aperture (cm)			Fracture Permeability				Notes
				Min	Max	Avg	Min (cm)	Max (cm)	Avg (cm^2)	Avg (m^2)	
CK1	131	SV	25.4	0.6	0.8	0.7	0.03	0.05	0.04	4.08E-06	
7/22/16	--	--	33.02	--	--	9	--	--	--	--	void
SP Graben-outer	--	--	25.4	1.2	1.2	1.2	0.12	0.12	0.12	1.20E-05	
	--	--	10.16	1.5	1.5	1.5	0.19	0.19	0.19	1.88E-05	
First measurements	--	--	6.99	2	2	2	0.33	0.33	0.33	3.33E-05	
No Brunton	--	--	8.89	7.5	7.5	7.5	4.69	4.69	4.69	4.69E-04	
	--	--	9.4	0.6	0.6	0.6	0.03	0.03	0.03	3.00E-06	
	--	--	6.35	0.7	0.7	0.7	0.04	0.04	0.04	4.08E-06	
	--	--	13.72	2	2	2	0.33	0.33	0.33	3.33E-05	
	--	--	4.32	0.2	0.9	0.55	0.00	0.07	0.03	2.52E-06	
	--	H	55.25	0.5	0.7	0.6	0.02	0.04	0.03	3.00E-06	
	--	V	54.61	0.1	0.3	0.2	0.00	0.01	0.00	3.33E-07	
	--	--	9.53	0	0.1	0.05	0.00	0.00	0.00	2.08E-08	
	--	--	10.8	0.1	0.1	0.1	0.00	0.00	0.00	8.33E-08	
	--	--	5.72	0.1	0.1	0.1	0.00	0.00	0.00	8.33E-08	
	--	--	4.47	0	0.1	0.05	0.00	0.00	0.00	2.08E-08	
	--	--	4.19	0	0.1	0.05	0.00	0.00	0.00	2.08E-08	
	--	--	8.89	0	0.1	0.05	0.00	0.00	0.00	2.08E-08	
	--	--	8.89	0	0.1	0.05	0.00	0.00	0.00	2.08E-08	
	--	--	8.89	0	0.1	0.05	0.00	0.00	0.00	2.08E-08	
	--	--	14.61	0.4	0.4	0.4	0.01	0.01	0.01	1.33E-06	
	--	--	10.16	0.4	1.76	1.08	0.01	0.26	0.10	9.72E-06	
Strike/Dip min:	--	--		Aperture min:		0.00		Average k min:		2.08E-08	
Max:	--	--		Max (excluding voids):		7.50		Max:		4.69E-04	
Average:	--	--		Average:		0.93		Average:		2.83E-05	
Mode:	--	--		Mode of averages:		0.05		Mode:		2.08E-08	
CK2	--	8	100	0.70	0.8	0.75	0.04	0.05	0.05	4.69E-06	Primarily vertical/ subvertical fractures
7/22/16	--	--	51.435	0.7	0.9	0.80	0.04	0.07	0.05	5.33E-06	Highly weathered, surface exposure
SP Graben-inner	--	--	12.065	0.7	0.7	0.70	0.04	0.04	0.04	4.08E-06	3
	--	--	100	1.7	1.7	1.70	0.24	0.24	0.24	2.41E-05	4
	--	--	16.51	0.7	0.7	0.70	0.04	0.04	0.04	4.08E-06	4a
	--	--	6.604	1	1	1.00	0.08	0.08	0.08	8.33E-06	5
	--	H	100	2.5	3.5	3.00	0.52	1.02	0.75	7.50E-05	6
	--	--	17.78	0.7	0.7	0.70	0.04	0.04	0.04	4.08E-06	7
	--	--	39.37	0.4	0.4	0.40	0.01	0.01	0.01	1.33E-06	8
	--	--	10.16	0.3	0.3	0.30	0.01	0.01	0.01	7.50E-07	9
	--	--	10.795	0.2	0.2	0.20	0.00	0.00	0.00	3.33E-07	10
	--	--	10.795	0.1	0.1	0.10	0.00	0.00	0.00	8.33E-08	11
	--	--	10.16	0.4	0.4	0.40	0.01	0.01	0.01	1.33E-06	12
	--	--	7.62	0.05	0.05	0.05	0.00	0.00	0.00	2.08E-08	13
	--	--	5.588	0.05	0.05	0.05	0.00	0.00	0.00	2.08E-08	14
	--	--	14.605	0.05	0.05	0.05	0.00	0.00	0.00	2.08E-08	15
	--	--	5.08	0.05	0.05	0.05	0.00	0.00	0.00	2.08E-08	16
	--	--	6.985	0.05	0.05	0.05	0.00	0.00	0.00	2.08E-08	17
	--	--	5.08	0.05	0.05	0.05	0.00	0.00	0.00	2.08E-08	18
	--	--	5.08	0.05	0.05	0.05	0.00	0.00	0.00	2.08E-08	19
	--	--	9.525	0.05	0.05	0.05	0.00	0.00	0.00	2.08E-08	20
Strike/Dip min:	--	--		Aperture min:		0.05		Average k min:		2.08E-08	
Max:	--	--		Max (excluding voids):		3.50		Max:		7.50E-05	
Average:	--	--		Average:		0.53		Average:		6.37E-06	
Mode:	--	--		Mode of averages:		0.05		Mode:		2.08E-08	

Table B-2 (cont.)

Outcrop	Strike	Dip	Length (cm)	Aperture (cm)			Fracture Permeability				Notes
				Min	Max	Avg	Min (cm)	Max (cm)	Avg (cm^2)	Avg (m^2)	
CK3	300	86	55.5	5.5	8	6.75	2.52	5.33	3.80	3.80E-04	1-- see image
8/8/16	300	86	12	0.1	0.1	0.1	0.00	0.00	0.00	8.33E-08	1a
North Graben	298	SV	70	0.1	0.3	0.2	0.00	0.01	0.00	3.33E-07	1b
	300	SV	13	0.1	0.1	0.1	0.00	0.00	0.00	8.33E-08	1c-- discontinuous
	290	67	35	0.1	0.2	0.15	0.00	0.00	0.00	1.88E-07	1d
	285	72	15	0.1	0.1	0.1	0.00	0.00	0.00	8.33E-08	2
	283	V	13.5	0.2	0.5	0.35	0.00	0.02	0.01	1.02E-06	3
	302	V	7	0.1	0.2	0.15	0.00	0.00	0.00	1.88E-07	4
	308	V	10	0.2	0.2	0.2	0.00	0.00	0.00	3.33E-07	5
	305	V	15.5	0.2	0.2	0.2	0.00	0.00	0.00	3.33E-07	6
	312	74	10.5	0.1	0.1	0.1	0.00	0.00	0.00	8.33E-08	7
	312	74	4	0.1	0.1	0.1	0.00	0.00	0.00	8.33E-08	7b
	308	V	11	0.1	0.2	0.15	0.00	0.00	0.00	1.88E-07	8
	326	V	86	0.2	0.3	0.25	0.00	0.01	0.01	5.21E-07	9
	292	SV	15	0.3	0.9	0.6	0.01	0.07	0.03	3.00E-06	10
	286	V	11	0.2	0.3	0.25	0.00	0.01	0.01	5.21E-07	11-- Part <0.1 aperture
	300	V	53	0.1	0.5	0.3	0.00	0.02	0.01	7.50E-07	12
	304	V	45.5	0.05	0.1	0.075	0.00	0.00	0.00	4.69E-08	13
	294	V	20	0.1	0.2	0.15	0.00	0.00	0.00	1.88E-07	14
	292	V	27	0.05	0.1	0.075	0.00	0.00	0.00	4.69E-08	15
	295	H	27	1	1.5	1.25	0.08	0.19	0.13	1.30E-05	16
Strike/Dip min:	283	--		Aperture min:		0.05		Average k min:		4.69E-08	
Max:	326	--		Max (excluding voids):		8.00		Max:		3.80E-04	
Average:	299.6	--		Average:		0.55		Average:		1.91E-05	
Mode:	300.0	--		Mode of averages:		0.10		Mode:		8.33E-08	
CK4	215	84	29	0.1	0.1	0.1	0.00	0.00	0.00	8.33E-08	1-- Max 1.3x 7.0 cm
8/16/16	150	35	47	0.05	0.05	0.05	0.00	0.00	0.00	2.08E-08	1a
Wash W of graben	215	39	20.5	0.05	0.05	0.05	0.00	0.00	0.00	2.08E-08	1b
	136	50	33	0.5	1	0.75	0.02	0.08	0.05	4.69E-06	2
	147	42	55	0.1	0.1	0.1	0.00	0.00	0.00	8.33E-08	3-- offshoot=11 x 0.1
	176	64	20	0.3	1.5	0.9	0.01	0.19	0.07	6.75E-06	4
	150	60	36	0.05	0.05	0.05	0.00	0.00	0.00	2.08E-08	5
	183	1	100	0.1	0.1	0.1	0.00	0.00	0.00	8.33E-08	6-- 3 layers-- bedding plane
	208	65	23	0.2	0.3	0.25	0.00	0.01	0.01	5.21E-07	7
	193	1	83	0.1	0.2	0.15	0.00	0.00	0.00	1.88E-07	8
	219	34	12	0.05	0.05	0.05	0.00	0.00	0.00	2.08E-08	9
	203	32	9	0.05	0.1	0.075	0.00	0.00	0.00	4.69E-08	10
	177	SV	21	0.05	0.1	0.075	0.00	0.00	0.00	4.69E-08	11-- +3 cm offshoot
	186	14	12	0.05	0.05	0.05	0.00	0.00	0.00	2.08E-08	12
	165	66	12	0.05	0.1	0.075	0.00	0.00	0.00	4.69E-08	13
Strike/Dip min:	136	1		Aperture min:		0.05		Average k min:		2.08E-08	
Max:	219	84		Max (excluding voids):		1.50		Max:		6.75E-06	
Average:	181.5	41.9		Average:		0.19		Average:		8.43E-07	
Mode:	215.0	1.0		Mode of averages:		0.05		Mode:		2.08E-08	
CK5	284	89	31	0.2	0.5	0.35	0.00	0.02	0.01	1.02E-06	1
8/16/16	305	52	6	0.7	0.7	0.7	0.04	0.04	0.04	4.08E-06	1a
Wash W of graben	304	V	17	0.05	0.1	0.075	0.00	0.00	0.00	4.69E-08	2
	300	V	29	0.1	1.5	0.8	0.00	0.19	0.05	5.33E-06	2a-- 6 cm long max
	269	90	45.5	5	5	5	2.08	2.08	2.08	2.08E-04	3
	310	80	41	1	1	1	0.08	0.08	0.08	8.33E-06	3a
	314	79	29	0.2	0.7	0.45	0.00	0.04	0.02	1.69E-06	3b
	305	75	28	1	1	1	0.08	0.08	0.08	8.33E-06	3c
	274	75	31	1	1	1	0.08	0.08	0.08	8.33E-06	3d
	305	V	26	0.2	0.7	0.45	0.00	0.04	0.02	1.69E-06	4
	302	12	6	1.5	1.5	1.5	0.19	0.19	0.19	1.88E-05	4b
	271	V- 30	19.5	0.05	0.5	0.275	0.00	0.02	0.01	6.30E-07	5
	291	42	7	0.1	0.3	0.2	0.00	0.01	0.00	3.33E-07	6
	226	20	35	0.1	0.2	0.15	0.00	0.00	0.00	1.88E-07	7
	312	20	30.5	0.05	0.1	0.075	0.00	0.00	0.00	4.69E-08	8
	272	1	24	0.1	0.3	0.2	0.00	0.01	0.00	3.33E-07	9
	310	4	100	3	4	3.5	0.75	1.33	1.02	1.02E-04	10
	308	3	100	0.1	0.5	0.3	0.00	0.02	0.01	7.50E-07	11
	311	2	100	0.05	0.1	0.075	0.00	0.00	0.00	4.69E-08	12
Strike/Dip min:	226	1		Aperture min:		0.05		Average k min:		4.69E-08	
Max:	314	90		Max (excluding voids):		5.00		Max:		2.08E-04	
Average:	293.3	42.9		Average:		0.90		Average:		1.95E-05	
Mode:	305.0	75.0		Mode of averages:		0.08		Mode:		4.69E-08	

Table B-3: Fracture measurement data for Kaibab Limestone outcrops near Rattlesnake Crater, Arizona. Gray indicates uncertainty in measurement or recording.

Fracture Data: Kaibab Limestone near Rattlesnake Crater											
Outcrop	Strike	Dip	Length (cm)	Aperture (cm)			Fracture Permeability				Notes
				Min	Max	Avg	min (cm^2)	max (cm^2)	avg (cm^2)	avg (m^2)	
RK1	--	SH	34.54	0.20	0.20	0.20	0.00	0.00	0.00	3.33E-07	1
7/24/16	--	SV	22.86	2.50	2.50	2.50	0.52	0.52	0.52	5.21E-05	2a
San Franisco Wash	--	SV	21.59	0.70	0.80	0.75	0.04	0.05	0.05	4.69E-06	2b
S: 300, D: 80	--	SH	59.69	1.20	2.00	1.60	0.12	0.33	0.21	2.13E-05	3
	--	SH	34.29	12.07	12.07	12.07	--	--	--	--	4-- Hole
	24	75	23	--	--	1.50	--	--	0.19	1.88E-05	1a
	--	--	24	--	--	0.70	--	--	0.04	4.08E-06	1b
	--	--	49	3.00	3.50	3.25	0.75	1.02	0.88	8.80E-05	1c
	30	7	34.5	1.00	2.00	1.50	0.08	0.33	0.19	1.88E-05	2
	19	2	38	0.05	0.70	0.38	0.00	0.04	0.01	1.17E-06	3
	26	SH, variable	40	1.00	3.00	2.00	0.08	0.75	0.33	3.33E-05	4
	20	SH, variable	23	3.00	3.50	3.25	0.75	1.02	0.88	8.80E-05	5a
	--	--	15	--	--	20.00	--	--	--	--	5b-- Void
	12	0	22.5	1.00	1.50	1.25	0.08	0.19	0.13	1.30E-05	6a
	--	--	9	0.40	0.50	0.45	0.01	0.02	0.02	1.69E-06	6b
	15	10	41	1.50	2.00	1.75	0.19	0.33	0.26	2.55E-05	7a
	--	--	8	--	--	0.20	--	--	0.00	3.33E-07	7b
	19	SH	9.5			3.00	0.00	0.00	0.75	7.50E-05	8
	20	22	52	6.00	8.00	7.00	3.00	5.33	4.08	4.08E-04	9
	25	0	70	1.00	2.00	1.50	0.08	0.33	0.19	1.88E-05	10a
	--	--	31.5	1.50	10.00	5.75	--	--	--	--	10b-- Void
	26	SH	24	2.00	3.00	2.50	0.33	0.75	0.52	5.21E-05	11a
	--	--	15	3.00	3.50	3.25	--	--	--	--	11a Void
	--	--	9	--	--	0.10	--	--	0.00	8.33E-08	11b
	--	--	3.5	--	--	0.05	--	--	0.00	2.08E-08	11c
	--	--	5	--	--	0.05	--	--	0.00	2.08E-08	11d
	--	--	7	--	--	0.05	--	--	0.00	2.08E-08	11e
	--	--	14.5	0.10	0.20	0.15	0.00	0.00	0.00	1.88E-07	11f
	--	--	4	--	--	0.30	--	--	0.01	7.50E-07	11g
	--	--	35.4	15.00	51.00	33.00	--	--	--	--	11h-- Void, 35 cm depth
	37	70	3.75	0.10	0.20	0.15	0.00	0.00	0.00	1.88E-07	12a
	1	68	4.2	0.10	0.20	0.15	0.00	0.00	0.00	1.88E-07	12b
	6	69	14.5	0.05	0.10	0.08	0.00	0.00	0.00	4.69E-08	12c
	27	80	9.5	0.05	0.20	0.13	0.00	0.00	0.00	1.30E-07	12d
	43	85	6.5	--	--	0.10	--	--	0.00	8.33E-08	12e
	21	SH	31	0.10	0.20	0.15	0.00	0.00	0.00	1.88E-07	13a
	24	SH	17.5	0.10	0.20	0.15	0.00	0.00	0.00	1.88E-07	13b
	19	SH	16	0.10	0.25	0.18	0.00	0.01	0.00	2.55E-07	13c
	11	SH	22	0.10	0.20	0.15	0.00	0.00	0.00	1.88E-07	13d
	12	SH	5.5	0.10	0.30	0.20	0.00	0.01	0.00	3.33E-07	13e
	48	V	10	--	--	0.20	--	--	0.00	3.33E-07	14
	38	V	5.5	--	--	0.10	--	--	0.00	8.33E-08	15
	35	19	16.5	0.05	0.30	0.18	0.00	0.01	0.00	2.55E-07	16a
	28	5	11.75	0.05	0.30	0.18	0.00	0.01	0.00	2.55E-07	16b
	27	19	26.25	0.05	0.30	0.18	0.00	0.01	0.00	2.55E-07	16c
	27	30	33.25	0.05	0.15	0.10	0.00	0.00	0.00	8.33E-08	16d
	21	V-99	24.75	--	--	0.20	--	--	0.00	3.33E-07	17a
	11-330	V	20	0.20	0.50	0.35	0.00	0.02	0.01	1.02E-06	17b
	5	V	21	0.10	0.20	0.15	0.00	0.00	0.00	1.88E-07	17c
	5	V	8	--	--	0.10	--	--	0.00	8.33E-08	17d
	6	--	4.5	--	--	0.10	--	--	0.00	8.33E-08	18a
	--	--	3	--	--	0.10	--	--	0.00	8.33E-08	18b
	--	--	2	0.05	0.10	0.08	0.00	0.00	0.00	4.69E-08	18c
	--	--	5.5	--	--	0.10	--	--	0.00	8.33E-08	18d
	--	--	9	0.10	0.20	0.15	0.00	0.00	0.00	1.88E-07	18e
	--	V	6.75	0.10	0.20	0.15	0.00	0.00	0.00	1.88E-07	19a
	--	H	7.3	0.05	0.10	0.08	0.00	0.00	0.00	4.69E-08	19b
	--	V	7.5	0.05	0.10	0.08	0.00	0.00	0.00	4.69E-08	19c
	--	H	7.5			0.10	0.00	0.00	0.00	8.33E-08	19d
	--	SV	9.5	0.05	0.10	0.08	0.00	0.00	0.00	4.69E-08	19e
	--	V	2.5	--	--	0.05	--	--	0.00	2.08E-08	20a
	--	V	13	0.05	0.10	0.08	0.00	0.00	0.00	4.69E-08	20b
	--	--	14.5	0.10	0.90	0.50	0.00	0.07	0.02	2.08E-06	20c
	--	--	11	--	--	0.10	--	--	0.00	8.33E-08	20d
	--	H	23	0.05	0.10	0.08	0.00	0.00	0.00	4.69E-08	20e
Strike/Dip min:	1	0			Aperture min:	0.05			Average k min:	2.08E-08	
Max:	48	99			Max (excluding voids):	7.00			Max:	4.08E-04	
Average:	21.8	35.1			Average:	0.68			Average:	1.56E-05	
Mode:	19.0	0.0			Mode of averages:	0.10			Mode:	8.33E-08	

Table B-3 (cont.)

Outcrop	Strike	Dip	Length (cm)	Aperture (cm)			Fracture Permeability				Notes
				Min	Max	Avg	min (cm^2)	max (cm^2)	avg (cm^2)	avg (m^2)	
RK2	104	75	55	0.10	0.20	0.15	0.00	0.00	0.00	1.88E-07	1a
7/26/16	--	--	35	0.10	0.20	0.15	0.00	0.00	0.00	1.88E-07	1b
SF Wash	105	88	28	--	--	0.30	--	--	0.01	7.50E-07	2
S: 122, D: 0	115	6	40.5	--	--	0.10	--	--	0.00	8.33E-08	3-- Appears filled- weathering feature?
	150	V	6	--	--	0.10	--	--	0.00	8.33E-08	4
	114	V	14.5	0.10	0.20	0.15	0.00	0.00	0.00	1.88E-07	5
	116	V	21.5	0.10	0.20	0.15	0.00	0.00	0.00	1.88E-07	6a
	--	--	9.5	0.05	0.10	0.08	0.00	0.00	0.00	4.69E-08	6b
	115	85	17.5	0.10	0.20	0.15	0.00	0.00	0.00	1.88E-07	7a
	--	--	8	0.10	0.20	0.15	0.00	0.00	0.00	1.88E-07	7b
	--	--	10.5	1.50	6.00	3.75	0.19	3.00	1.17	1.17E-04	7c
	119	H	36.5	--	--	0.20	--	--	0.00	3.33E-07	8
	139	V	46	0.20	0.60	0.40	0.00	0.03	0.01	1.33E-06	9a
	--	--	5	--	--	0.05	--	--	0.00	2.08E-08	9b
	--	--	9	--	--	0.05	--	--	0.00	2.08E-08	9c
	--	--	2.5	--	--	0.10	--	--	0.00	8.33E-08	9d
	--	--	10	--	--	0.10	--	--	0.00	8.33E-08	9e
	--	--	15	--	--	0.10	--	--	0.00	8.33E-08	9f
	90	76	23	0.40	0.60	0.50	0.01	0.03	0.02	2.08E-06	10
	344	50	17.5	0.30	0.60	0.45	0.01	0.03	0.02	1.69E-06	11
	100	67	8	--	--	0.10	--	--	0.00	8.33E-08	12
	332	66	13.5	0.20	0.40	0.30	0.00	0.01	0.01	7.50E-07	13a
	--	--	4	--	--	2.50	--	--	0.52	5.21E-05	13b-- Void
	95	74	16	0.05	0.10	0.08	0.00	0.00	0.00	4.69E-08	14
	90	V	19	--	--	0.01	--	--	0.00	8.33E-10	15
	89	V	12.5	--	--	0.10	--	--	0.00	8.33E-08	16a
	--	--	18	--	--	0.05	--	--	0.00	2.08E-08	16b
	122	85	19	1.00	2.25	1.63	0.08	0.42	0.22	2.20E-05	17
	100	SV	5.5	0.10	0.20	0.15	0.00	0.00	0.00	1.88E-07	18a
	--	--	4.5	0.10	0.20	0.15	0.00	0.00	0.00	1.88E-07	18b
Strike/Dip min:	89	6			Aperture min:	0.05			Average k min:	8.33E-10	
Max:	344	88			Max (excluding voids):	6.00			Max:	1.17E-04	
Average:	135.5	67.2			Average:	0.34			Average:	6.68E-06	
Mode:	115.0	85.0			Mode of averages:	0.15			Mode:	1.88E-07	
RK3											Unfractured ~2.5m thick
7/30/16	--	--	--	--	--	--	--	--	--	--	Spalling present
SF Wash											
RK4	320	60	23.5	0.10	0.20	0.15	0.00	0.00	0.00	1.88E-07	
7/30/16	320	H	29	0.10	0.20	0.15	0.00	0.00	0.00	1.88E-07	2a
SF Wash	348	23	5.5	0.50	0.60	0.55	0.02	0.03	0.03	2.52E-06	2b
	335	68	38	0.10	0.30	0.20	0.00	0.01	0.00	3.33E-07	3a
	291	22	9	0.10	0.20	0.15	0.00	0.00	0.00	1.88E-07	3b
	350	SV	18.5	0.50	2.00	1.25	0.02	0.33	0.13	1.30E-05	3c
	312	H	100	--	--	2.20	--	--	0.40	4.03E-05	4a
	312	9	21	--	--	1.00	--	--	0.08	8.33E-06	4b
	312	SH	100	0.02	0.05	0.04	0.00	0.00	0.00	1.02E-08	5
	345	V	22	--	--	0.10	--	--	0.00	8.33E-08	6a
	284	78	26	0.05	1.00	0.53	0.00	0.08	0.02	2.30E-06	6b
	312	H	26	--	--	0.05	--	--	0.00	2.08E-08	7
	305	83	29	0.02	0.05	0.04	0.00	0.00	0.00	1.02E-08	8
	--	--	--	--	--	--	--	--	--	--	9: Void-area
	330	SH	17	0.05	1.00	0.53	0.00	0.08	0.02	2.30E-06	9a
	330	SH	26	1.30	3.60	2.45	0.14	1.08	0.50	5.00E-05	9b
Strike/Dip min:	284	9			Aperture min:	0.02			Average k min:	1.02E-08	
Max:	350	83			Max (excluding voids):	3.60			Max:	5.00E-05	
Average:	320.4	49			Average:	0.62			Average:	7.99E-06	
Mode:	312.0	--			Mode of averages:	0.15			Mode:	1.88E-07	
RK5	340	71	61	0.30	0.40	0.35	0.01	0.01	0.01	1.02E-06	1a
7/30/16	--	--	29	0.10	0.20	0.15	0.00	0.00	0.00	1.88E-07	1b-- Overhang
SF Wash	17	V	30.5	0.20	0.30	0.25	0.00	0.01	0.01	5.21E-07	2
	341	62	27	0.20	1.20	0.70	0.00	0.12	0.04	4.08E-06	3
	350	60	18	0.10	0.90	0.50	0.00	0.07	0.02	2.08E-06	4
	330	75	16.2	0.10	0.20	0.15	0.00	0.00	0.00	1.88E-07	5- 5&6 parallel; both listed as 5
	330	75	3.5	--	--	0.10	--	--	0.00	8.33E-08	6
	~330 (est)	~H	21	0.01	0.05	0.03	0.00	0.00	0.00	7.50E-09	7
	"	"	15	0.01	0.05	0.03	0.00	0.00	0.00	7.50E-09	8-- All horizontal hairline fractures
	"	"	7.5	0.01	0.05	0.03	0.00	0.00	0.00	7.50E-09	9
	"	"	10	0.01	0.05	0.03	0.00	0.00	0.00	7.50E-09	10
	"	"	11	0.01	0.05	0.03	0.00	0.00	0.00	7.50E-09	11
	"	"	11	0.01	0.05	0.03	0.00	0.00	0.00	7.50E-09	12
Strike/Dip min:	17	60			Aperture min:	0.01			Average k min:	7.50E-09	
Max:	350	75			Max (excluding voids):	1.20			Max:	4.08E-06	
Average:	284.7	68.6			Average:	0.18			Average:	6.32E-07	
Mode:	330.0	75			Mode of averages:	0.03			Mode:	7.50E-09	

Table B-3 (cont.)

Outcrop	Strike	Dip	Length (cm)	Aperture (cm)			Fracture Permeability				Notes
				Min	Max	Avg	min (cm^2)	max (cm^2)	avg (cm^2)	avg (m^2)	
RK6			180	0.10	0.20	0.15	0.00	0.00	0.00	1.88E-07	1- Mineralized, discontinuous
7/31/16			100	0.60	0.70	0.65	0.03	0.04	0.04	3.52E-06	2
SF Wash											Largely unfractured, massive 2.5-3 m thick
											Highly weathered
RK7	311	90	130	0.00	0.10	0.05	0.00	0.00	0.00	2.08E-08	1
7/31/16	--	--	6.2	--	--	2.50	--	--	0.52	5.21E-05	1a
SF Wash	288	0	26	--	--	2.00	--	--	0.33	3.33E-05	2
	288	0	17	0.05	0.10	0.08	0.00	0.00	0.00	4.69E-08	3
	288	0	21.5	--	--	0.10	--	--	0.00	8.33E-08	4
	290	6	17	--	--	0.05	--	--	0.00	2.08E-08	5
	290	0	30	0.05	0.10	0.08	0.00	0.00	0.00	4.69E-08	6
	341	irregular	36	--	--	0.10	--	--	0.00	8.33E-08	7
	349	irregular	11	0.10	0.20	0.15	0.00	0.00	0.00	1.88E-07	8
	295	?	10	--	--	0.00	--	--	0.00	0.00E+00	9
	297	0	13	0.00	0.50	0.25	0.00	0.02	0.01	5.21E-07	10
	240	50	32	--	--	0.10	--	--	0.00	8.33E-08	11
	275	90	40	0.00	0.10	0.05	0.00	0.00	0.00	2.08E-08	12
	300	0	21.5	--	--	0.10	--	--	0.00	8.33E-08	13
	272	0	135	0.10	0.20	0.15	0.00	0.00	0.00	1.88E-07	14
	--	--	12.5	0.20	0.50	0.35	0.00	0.02	0.01	1.02E-06	15
	273	90	4.5	--	--	0.30	--	--	0.01	7.50E-07	16
Strike/Dip min:	240	0			Aperture min:	0.00			Average k min:	0.00E+00	
Max:	349	90			Max (excluding voids):	0.50			Max:	5.21E-05	
Average:	293.1	27.2			Average:	0.38			Average:	5.21E-06	
Mode:	288.0	0			Mode of averages:	0.10			Mode:	8.33E-08	
RK8	87	0	112	0.30	0.60	0.45	0.01	0.03	0.02	1.69E-06	1
7/31/16	--	--	19	1.00	7.80	4.40	0.08	5.07	1.61	1.61E-04	1a-- void
SF Wash	--	--	22	2.00	11.80	6.90	0.33	11.60	3.97	3.97E-04	1b-- void
	--	--	6.5	2.00	5.00	3.50	0.33	2.08	1.02	1.02E-04	1c-- void
	--	--	29	0.10	0.30	0.20	0.00	0.01	0.00	3.33E-07	2-- calcite infills from 1.0-1.5
	92	0	100	--	--	0.20	--	--	0.00	3.33E-07	3
	92		12	--	--	0.10	--	--	0.00	8.33E-08	4
	92		30	--	--	0.10			0.00	8.33E-08	5
	92		66	0.10	0.20	0.15	0.00	0.00	0.00	1.88E-07	6
	92		9	0.10	0.20	0.15	0.00	0.00	0.00	1.88E-07	7
	92		20	0.05	0.10	0.08	0.00	0.00	0.00	4.69E-08	8
	92		31.5	--	--	0.10	--	--	0.00	8.33E-08	9
	92		16	--	--	0.10	--	--	0.00	8.33E-08	10
	--	--	7	--	--	0.10	--	--	0.00	8.33E-08	11
	--	--	5.5	--	--	0.10	--	--	0.00	8.33E-08	12
	--	--	38	0.05	0.10	0.08	0.00	0.00	0.00	4.69E-08	13
	--	--	66	--	--	0.10	--	--	0.00	8.33E-08	14
	--	--	22	--	--	0.10	--	--	0.00	8.33E-08	15
	--	--	45	0.05	0.10	0.08	0.00	0.00	0.00	4.69E-08	16
	--	--	5	0.10	0.20	0.15	0.00	0.00	0.00	1.88E-07	17
	--	--	20	0.05	0.10	0.08	0.00	0.00	0.00	4.69E-08	18
	--	--	10.5	--	--	0.10	--	--	0.00	8.33E-08	19
	--	--	6	--	--	0.05	--	--	0.00	2.08E-08	20
	--	--	19.5	--	--	<0.05	--	--	--	--	21
	--	19	3	--	--	2.00	--	--	--	--	1a- All ~half circle voids
	--	22	2	--	--	7.80	--	--	--	--	1b
	--	6.5	2.5	--	--	11.80	--	--	--	--	1c
Strike/Dip min:	87	0			Aperture min:	0.05			Average k min:	2.08E-08	
Max:	92	--			Max (excluding voids):	11.80			Max:	3.97E-04	
Average:	91.4	--			Average:	1.54			Average:	2.89E-05	
Mode:	92.0	--			Mode of averages:	0.10			Mode:	8.33E-08	

Table B-3 (cont.)

Outcrop	Strike	Dip	Length (cm)	Aperture (cm)			Fracture Permeability				Notes
				Min	Max	Avg	min (cm^2)	max (cm^2)	avg (cm^2)	avg (m^2)	
RK9	68	80	68.5	0.40	0.50	0.45	0.01	0.02	0.02	1.69E-06	1
8/13/16	48	84	79.5	0.05	0.20	0.13	0.00	0.00	0.00	1.30E-07	2
West of RC	60	SV	26	0.05	0.20	0.13	0.00	0.00	0.00	1.30E-07	2a
	60	SV	14	0.10	0.20	0.15	0.00	0.00	0.00	1.88E-07	2b
	58	~45	28	0.20	0.30	0.25	0.00	0.01	0.01	5.21E-07	1b
	--	--	22	--	--	0.10	--	--	0.00	8.33E-08	2a
	40	SV	15	0.10	0.20	0.15	0.00	0.00	0.00	1.88E-07	2c
	18	H	17	0.05	0.10	0.08	0.00	0.00	0.00	4.69E-08	2d
	338	SV	14	0.20	0.30	0.25	0.00	0.01	0.01	5.21E-07	2e
	40	64	5.5	--	--	0.10	--	--	0.00	8.33E-08	2f
	40	SV	13	--	--	0.10	--	--	0.00	8.33E-08	3
	40	SV	4	--	--	0.05	--	--	0.00	2.08E-08	4
	5	40	38	0.05	0.20	0.13	0.00	0.00	0.00	1.30E-07	5-- Filled portions
	349	80	22	0.30	1.30	0.80	0.01	0.14	0.05	5.33E-06	6
	338	SV	12	--	--	0.10	--	--	0.00	8.33E-08	7
	48	SV	38	0.10	0.20	0.15	0.00	0.00	0.00	1.88E-07	8
	5	H	55	0.10	0.20	0.15	0.00	0.00	0.00	1.88E-07	9a
	5	H	33.5	0.60	1.00	0.80	0.03	0.08	0.05	5.33E-06	9b-- Seems filled
	30	SV	30	0.20	0.50	0.35	0.00	0.02	0.01	1.02E-06	10
	1	SV	27	0.05	0.30	0.18	0.00	0.01	0.00	2.55E-07	11
	42	SV	19	0.05	0.20	0.13	0.00	0.00	0.00	1.30E-07	12
	40	SV	50	--	--	0.20	--	--	0.00	3.33E-07	13
	6	V	16.5	0.10	0.20	0.15	0.00	0.00	0.00	1.88E-07	14
	339	SV	15	0.10	0.20	0.15	0.00	0.00	0.00	1.88E-07	15
	350	Irregular	44	0.10	0.20	0.15	0.00	0.00	0.00	1.88E-07	16
	28	SV	17	0.10	0.20	0.15	0.00	0.00	0.00	1.88E-07	16a
	355	Irregular	23.5	0.05	0.10	0.08	0.00	0.00	0.00	4.69E-08	16b
	5	SV	34	0.30	0.60	0.45	0.01	0.03	0.02	1.69E-06	17a-- Most closed
	78	SV	20	0.10	0.20	0.15	0.00	0.00	0.00	1.88E-07	17b-- Closed
	42	SV	15	--	--	--	--	--	--	--	18-- More vuggy, less fractured
	3	SV	25	0.05	0.20	0.13	0.00	0.00	0.00	1.30E-07	19
	44	SV	26	0.10	0.30	0.20	0.00	0.01	0.00	3.33E-07	20
	48	SV	10	0.05	0.20	0.13	0.00	0.00	0.00	1.30E-07	21
	--	--	26	--	--	13.00	--	--	14.08	1.41E-03	V1
	--	--	5	--	--	5.00	--	--	2.08	2.08E-04	V2
	--	--	4	--	--	4.00	--	--	1.33	1.33E-04	V3
	--	V	--	--	--	0.10	--	--	0.00	8.33E-08	x20 fractures… all appear mostly surficial
	--	--	--	--	--	0.10	--	--	0.00	8.33E-08	
	--	--	--	--	--	0.10	--	--	0.00	8.33E-08	
	--	--	--	--	--	0.10	--	--	0.00	8.33E-08	
	--	--	--	--	--	0.10	--	--	0.00	8.33E-08	
	--	--	--	--	--	0.10	--	--	0.00	8.33E-08	
	--	--	--	--	--	0.10	--	--	0.00	8.33E-08	
	--	--	--	--	--	0.10	--	--	0.00	8.33E-08	
	--	--	--	--	--	0.10	--	--	0.00	8.33E-08	
	--	--	--	--	--	0.10	--	--	0.00	8.33E-08	
	--	--	--	--	--	0.10	--	--	0.00	8.33E-08	
	--	--	--	--	--	0.10	--	--	0.00	8.33E-08	
	--	--	--	--	--	0.10	--	--	0.00	8.33E-08	
	--	--	--	--	--	0.10	--	--	0.00	8.33E-08	
	--	--	--	--	--	0.10	--	--	0.00	8.33E-08	
	--	--	--	--	--	0.10	--	--	0.00	8.33E-08	
	--	--	--	--	--	0.10	--	--	0.00	8.33E-08	
	--	--	--	--	--	0.10	--	--	0.00	8.33E-08	
	--	--	--	--	--	0.10	--	--	0.00	8.33E-08	
	--	--	--	--	--	0.10	--	--	0.00	8.33E-08	
	--	--	--	--	--	0.10	--	--	0.00	8.33E-08	
	--	--	--	--	--	0.10	--	--	0.00	8.33E-08	
Strike/Dip min:	1	40			Aperture min:	0.05			Average k min:	2.08E-08	
Max:	355	84			Max (excluding voids):	1.30			Max:	1.41E-03	
Average:	92.8	69.6			Average:	0.57			Average:	3.34E-05	
Mode:	40.0	80.0			Mode of averages:	0.10			Mode:	8.33E-08	
RK10	180	4	100	6.00	8.00	7.00	3.00	5.33	4.08	4.08E-04	1-- some spots 2.5 cm
8/13/16	203	79	~8.5	0.80	1.00	0.90	0.05	0.08	0.07	6.75E-06	2
SSE of RC	195	85	7.5	--	--	4.00	--	--	1.33	1.33E-04	3
	186	0	36	--	--	0.05	--	--	0.00	2.08E-08	4-- 0.05 cm to closed
	176	0	95	0.30	0.70	0.50	0.01	0.04	0.02	2.08E-06	5-- some closed
	180	2	10	0.10	0.20	0.15	0.00	0.00	0.00	1.88E-07	6
Strike/Dip min:	176	0			Aperture min:	0.10			Average k min:	2.08E-08	
Max:	203	85			Max (excluding voids):	8.00			Max:	4.08E-04	
Average:	186.7	28.3			Average:	2.10			Average:	9.18E-05	
Mode:	180.0	0.0			Mode of averages:	#N/A			Mode:	#N/A	

Table B-3 (cont.)

Outcrop	Strike	Dip	Length (cm)	Aperture (cm)			Fracture Permeability				Notes
				Min	Max	Avg	min (cm^2)	max (cm^2)	avg (cm^2)	avg (m^2)	
RK11	203	2	102	--	--	1.50	--	--	0.19	1.88E-05	1-- average aperture msmt
8/13/16	201	89	36	0.10	0.20	0.15	0.00	0.00	0.00	1.88E-07	2-- discontinuous ~17cm
SSE of RC	199	9	113	--	--	0.10	--	--	0.00	8.33E-08	3-- 1.5 cm aperture where broken
	226	V	21	0.05	1.00	0.53	0.00	0.08	0.02	2.30E-06	4-- filled with vegetation
	230	73	9.5	--	--	0.20	--	--	0.00	3.33E-07	4a
	236	80	9	0.20	1.00	0.60	0.00	0.08	0.03	3.00E-06	4b
	227	75	15	0.10	0.30	0.20	0.00	0.01	0.00	3.33E-07	5
	238	85	18	0.10	0.20	0.15	0.00	0.00	0.00	1.88E-07	6
	238	85	3	--	--	0.10	--	--	0.00	8.33E-08	6a
	218	SV	40	1.00	1.20	1.10	0.08	0.12	0.10	1.01E-05	7-- filled in
	140	65	33	0.10	0.20	0.15	0.00	0.00	0.00	1.88E-07	8
	160	SV	16	0.50	0.60	0.55	0.02	0.03	0.03	2.52E-06	9-- broken rock chunk
	209	SV	16	0.10	0.20	0.15	0.00	0.00	0.00	1.88E-07	10
	--	--	8.5	0.10	0.20	0.15	0.00	0.00	0.00	1.88E-07	underside of #5 shelf
	--	--	4	0.10	0.20	0.15	0.00	0.00	0.00	1.88E-07	
	--	--	8	0.10	0.20	0.15	0.00	0.00	0.00	1.88E-07	
Strike/Dip min:	140	2			Aperture min:	0.05			Average k min:	8.33E-08	
Max:	238	89			Max (excluding voids):	1.20			Max:	1.88E-05	
Average:	209.6	62.6			Average:	0.37			Average:	2.42E-06	
Mode:	238.0	85.0			Mode of averages:	0.15			Mode:	1.88E-07	
RK12	117	V	~4.6	3.00	5.00	4.00	0.75	2.08	1.33	1.33E-04	1-- Large scale vertical fractures
SF Wash	122	V	~4.6	3.00	5.00	4.00	0.75	2.08	1.33	1.33E-04	2
	108	V	~4.6	3.00	5.00	4.00	0.75	2.08	1.33	1.33E-04	3
	129	V	~4.6	3.00	5.00	4.00	0.75	2.08	1.33	1.33E-04	4
	117	V	~4.6	3.00	5.00	4.00	0.75	2.08	1.33	1.33E-04	5
Strike/Dip min:	108	--			Aperture min:	3.00			Average k min:	--	
Max:	129	--			Max (excluding voids):	5.00			Max:	--	
Average:	118.6	--			Average:	4.00			Average:	--	
Mode:	117.0	--			Mode of averages:	4.00			Mode:	--	

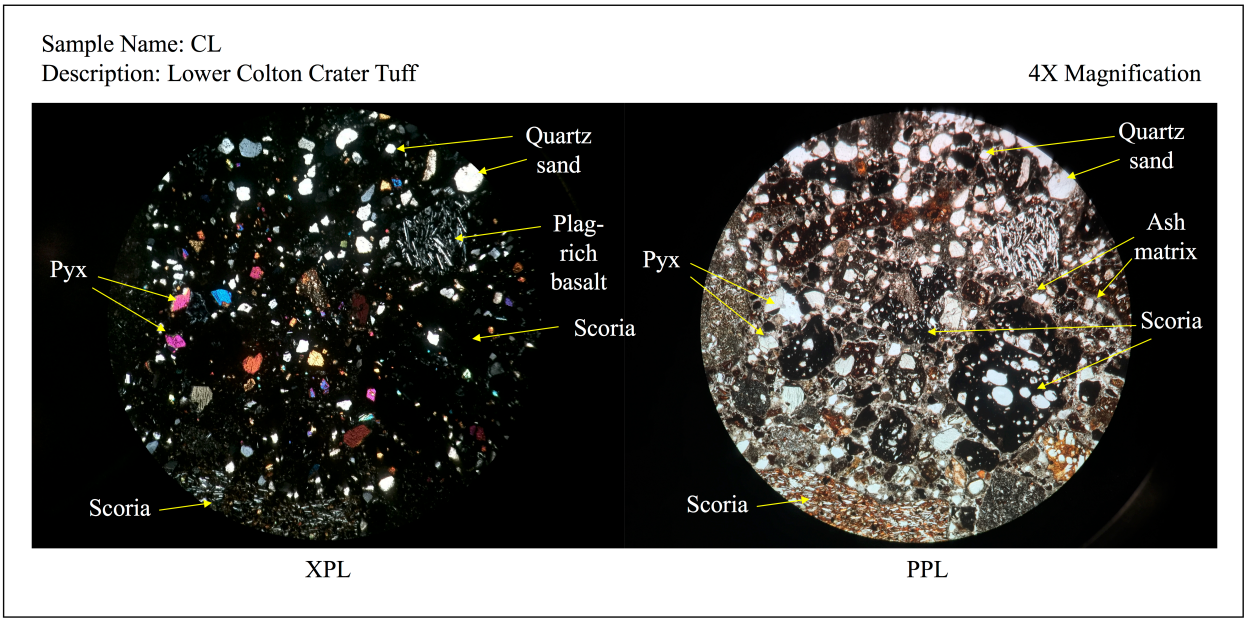

Figure B-1: Annotated photographs of thin section CL in XPL and PPL under 4x magnification.

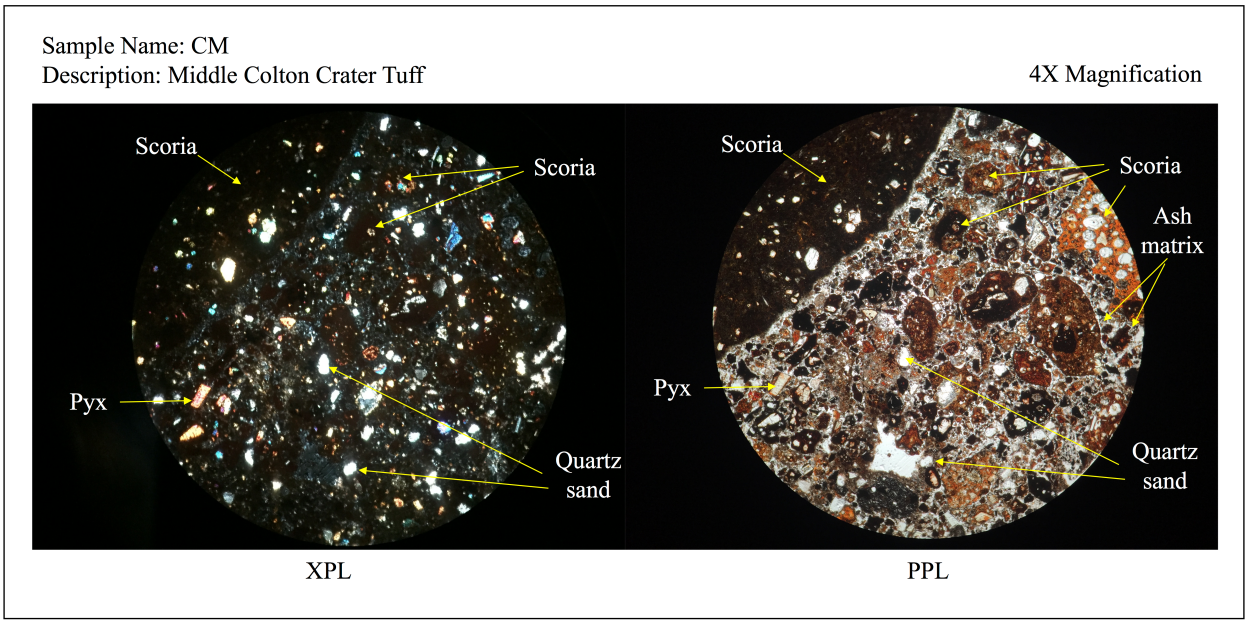

Figure B-2: Annotated photographs of thin section CM in XPL and PPL under 4x magnification.

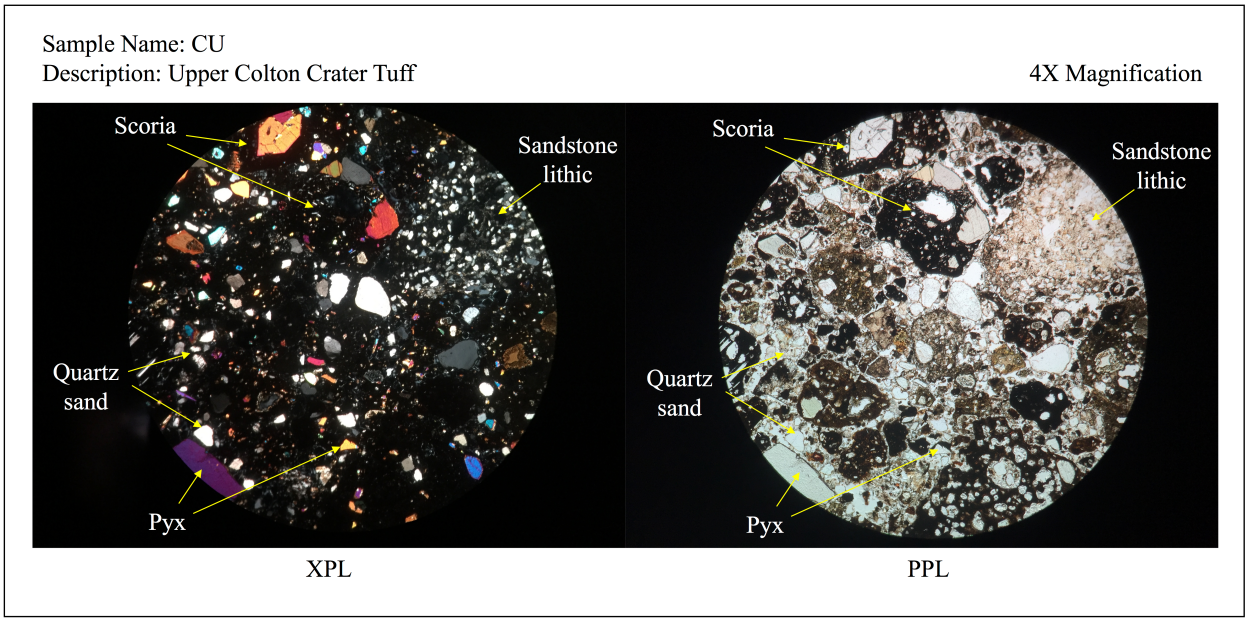

Figure B-3: Annotated photographs of thin section CU in XPL and PPL under 4x magnification.

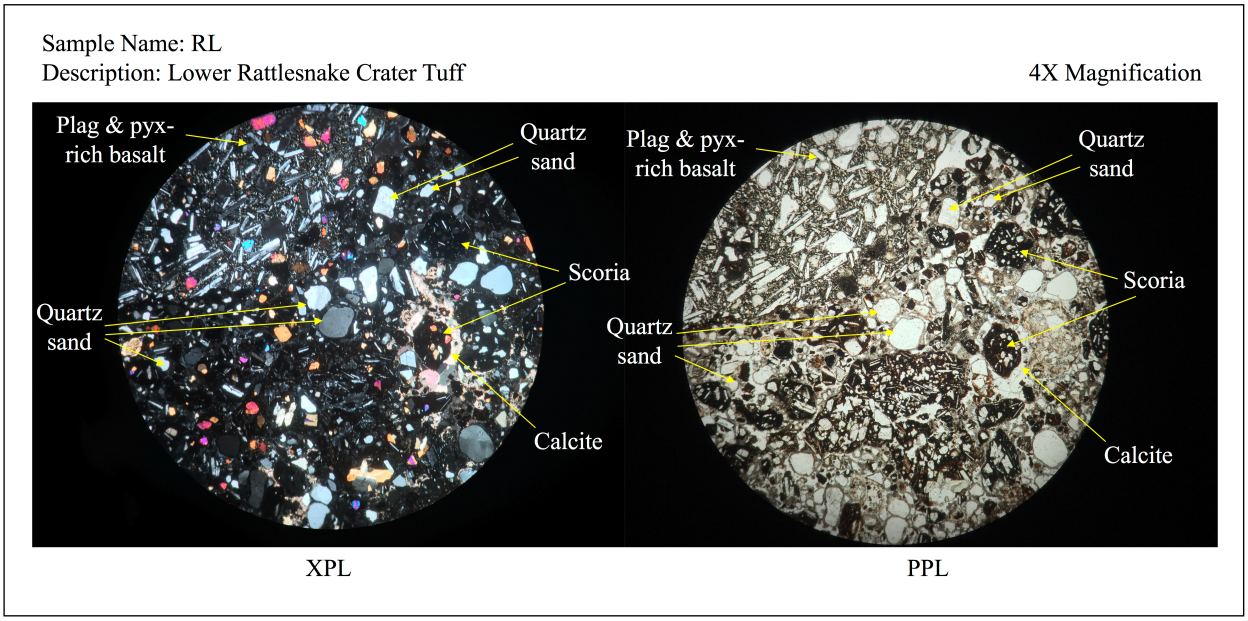

Figure B-4: Annotated photographs of thin section RL in XPL and PPL under 4x magnification.

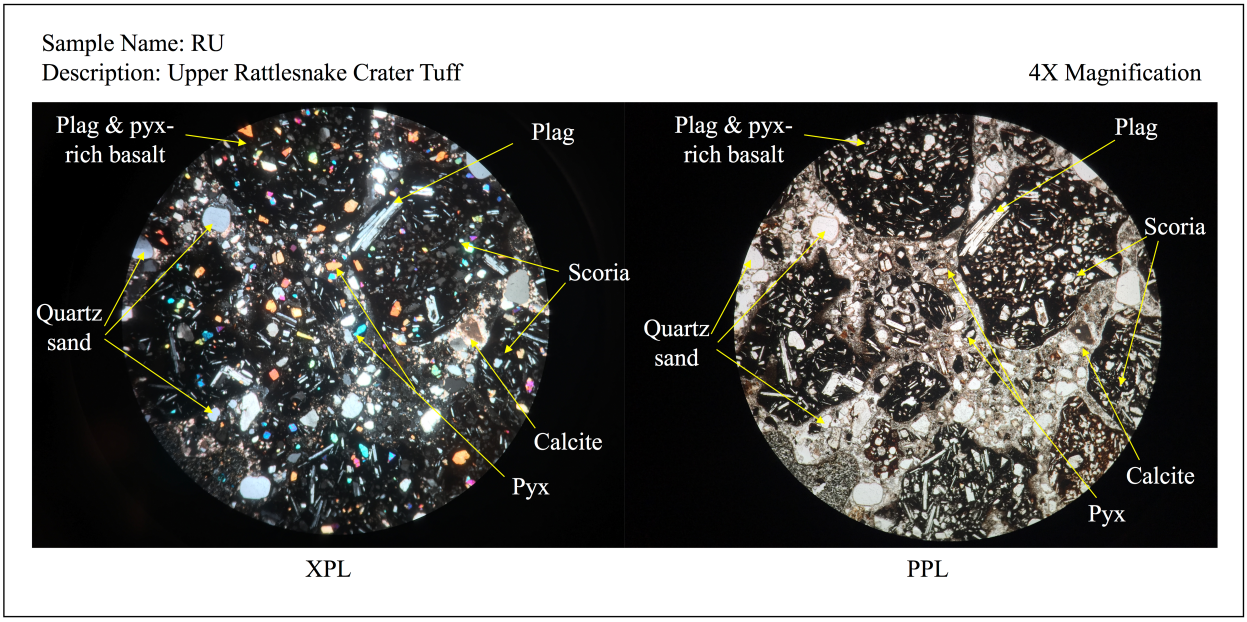

Figure B-5: Annotated photographs of thin section RU in XPL and PPL under 4x magnification.

APPENDIX C

MODELING DATA

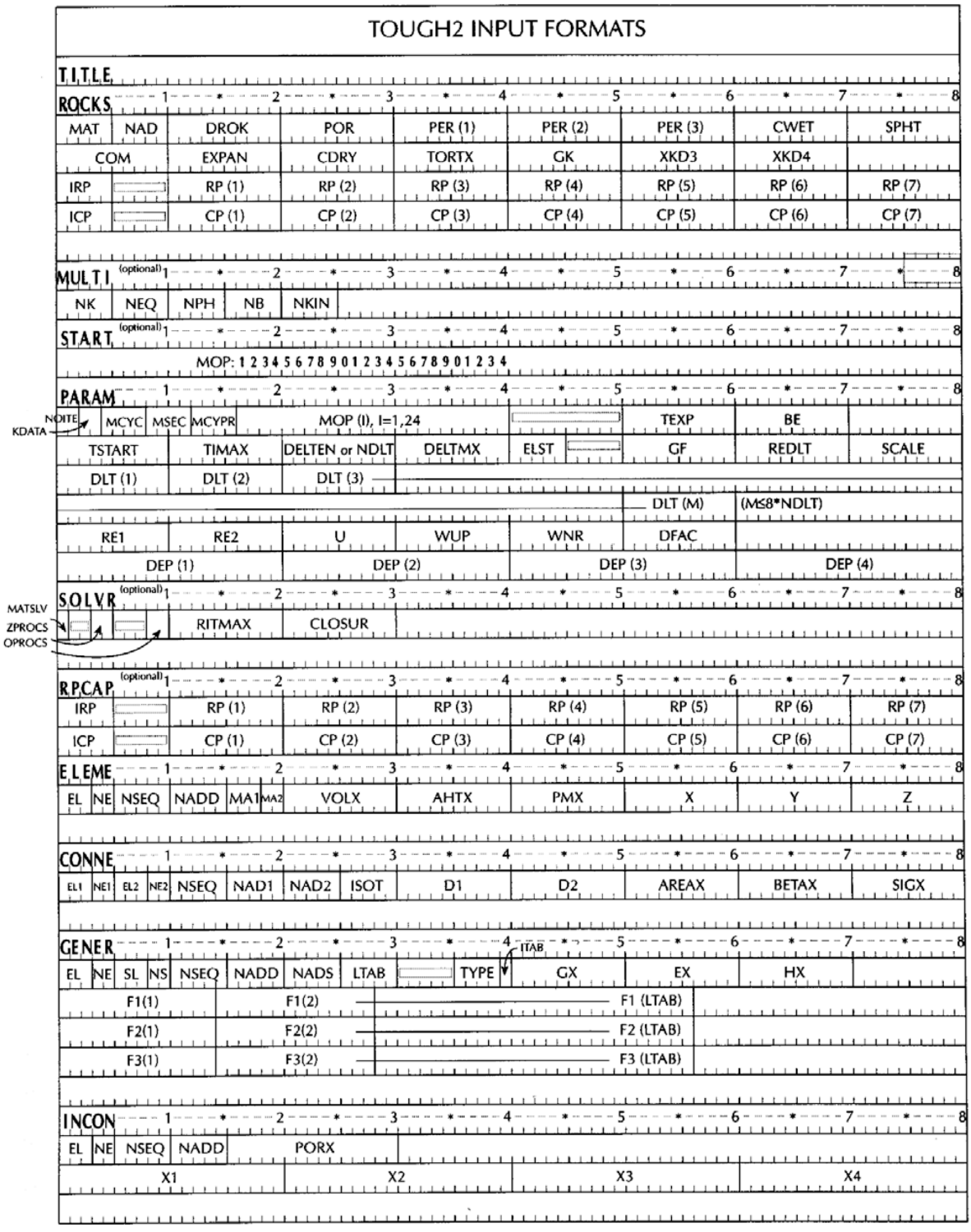

Figure C-1: TOUGH2 Input Formats. From Pruess et al. (2011).

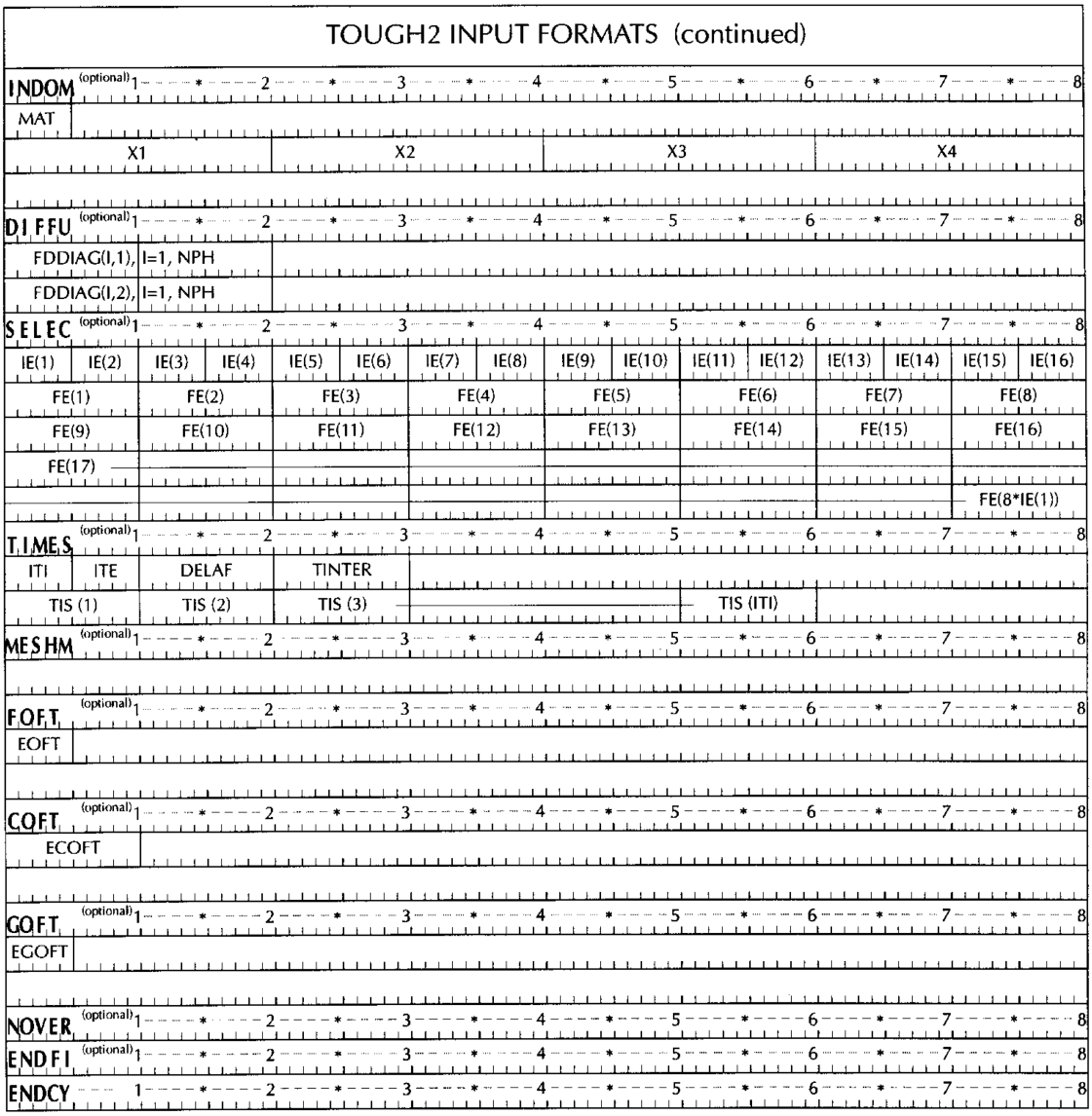

Figure C-1 (cont.)

```
ELEME
A11 1                10.2000E-020.2000E+02          0.1000E+020.5000E+00-.5000E-06
A21 1                10.3000E+030.0000E+00          0.1000E+020.5000E+00-.7500E+01
A31 1                10.3000E+030.0000E+00          0.1000E+020.5000E+00-.2250E+02
A41 1                10.3000E+030.0000E+00          0.1000E+020.5000E+00-.3750E+02
A51 1                10.3000E+030.0000E+00          0.1000E+020.5000E+00-.5250E+02
A61 1                10.3000E+030.0000E+00          0.1000E+020.5000E+00-.6750E+02
A71 1                20.2000E+030.0000E+00          0.1000E+020.5000E+00-.8000E+02
A81 1                20.2000E+030.0000E+00          0.1000E+020.5000E+00-.9000E+02
A91 1                20.2000E+030.0000E+00          0.1000E+020.5000E+00-.1000E+03
AA1 1                20.2000E+030.0000E+00          0.1000E+020.5000E+00-.1100E+03
AB1 1                20.2000E+030.0000E+00          0.1000E+020.5000E+00-.1200E+03
AC1 1                20.2000E+030.0000E+00          0.1000E+020.5000E+00-.1300E+03
AD1 1                20.2000E+030.0000E+00          0.1000E+020.5000E+00-.1400E+03
AE1 1                20.2000E+030.0000E+00          0.1000E+020.5000E+00-.1500E+03
AF1 1                20.2000E+030.0000E+00          0.1000E+020.5000E+00-.1600E+03
AG1 1                20.2000E+030.0000E+00          0.1000E+020.5000E+00-.1700E+03
AH1 1                20.2000E+030.0000E+00          0.1000E+020.5000E+00-.1800E+03
AI1 1                20.2000E+030.0000E+00          0.1000E+020.5000E+00-.1900E+03
AJ1 1                20.2000E+030.0000E+00          0.1000E+020.5000E+00-.2000E+03
AK1 1                20.2000E+030.0000E+00          0.1000E+020.5000E+00-.2100E+03
AL1 1                20.2000E+030.0000E+00          0.1000E+020.5000E+00-.2200E+03
AM1 1                20.2000E+030.0000E+00          0.1000E+020.5000E+00-.2300E+03
AN1 1                20.2000E+030.0000E+00          0.1000E+020.5000E+00-.2400E+03
AO1 1                20.2000E+030.0000E+00          0.1000E+020.5000E+00-.2500E+03
AP1 1                20.2000E+030.0000E+00          0.1000E+020.5000E+00-.2600E+03
AQ1 1                20.2000E+030.0000E+00          0.1000E+020.5000E+00-.2700E+03
AR1 1                20.2000E+030.0000E+00          0.1000E+020.5000E+00-.2800E+03
AS1 1                20.2000E+030.0000E+00          0.1000E+020.5000E+00-.2900E+03
AT1 1                20.2000E+030.0000E+00          0.1000E+020.5000E+00-.3000E+03
AU1 1                20.2000E+030.0000E+00          0.1000E+020.5000E+00-.3100E+03
AV1 1                20.2000E+030.0000E+00          0.1000E+020.5000E+00-.3200E+03
AW1 1                20.2000E+030.0000E+00          0.1000E+020.5000E+00-.3300E+03
AX1 1                20.2000E+030.0000E+00          0.1000E+020.5000E+00-.3400E+03
AY1 1                30.2000E+030.0000E+00          0.1000E+020.5000E+00-.3500E+03
AZ1 1                60.2000E+030.0000E+00          0.1000E+020.5000E+00-.3600E+03
B11 1                60.2000E+030.0000E+00          0.1000E+020.5000E+00-.3700E+03
B21 1                60.2000E+030.0000E+00          0.1000E+020.5000E+00-.3800E+03
B31 1                60.2000E+030.0000E+00          0.1000E+020.5000E+00-.3900E+03
B41 1                60.2000E+030.0000E+00          0.1000E+020.5000E+00-.4000E+03
B51 1                60.2000E+030.0000E+00          0.1000E+020.5000E+00-.4100E+03
B61 1                60.2000E+030.0000E+00          0.1000E+020.5000E+00-.4200E+03
B71 1                70.1000E+500.1000E+01          0.1000E+020.5000E+00-.4250E+03
```

Figure C-2: Sample of the mesh used in base case models. Figure shows information for the first column of the mesh as shown in the ELEME block of the input file.

```
CONNE
A11 1A11 2                    10.1000E+020.1000E+020.1000E-05
A11 1A21 1                    30.5000E-060.7500E+010.2000E+020.1000E+01
A21 1A21 2                    10.1000E+020.1000E+020.1500E+02
A21 1A31 1                    30.7500E+010.7500E+010.2000E+020.1000E+01
A31 1A31 2                    10.1000E+020.1000E+020.1500E+02
A31 1A41 1                    30.7500E+010.7500E+010.2000E+020.1000E+01
A41 1A41 2                    10.1000E+020.1000E+020.1500E+02
A41 1A51 1                    30.7500E+010.7500E+010.2000E+020.1000E+01
A51 1A51 2                    10.1000E+020.1000E+020.1500E+02
A51 1A61 1                    30.7500E+010.7500E+010.2000E+020.1000E+01
A61 1A61 2                    10.1000E+020.1000E+020.1500E+02
A61 1A71 1                    30.7500E+010.5000E+010.2000E+020.1000E+01
A71 1A71 2                    10.1000E+020.1000E+020.1000E+02
A71 1A81 1                    30.5000E+010.5000E+010.2000E+020.1000E+01
A81 1A81 2                    10.1000E+020.1000E+020.1000E+02
A81 1A91 1                    30.5000E+010.5000E+010.2000E+020.1000E+01
A91 1A91 2                    10.1000E+020.1000E+020.1000E+02
A91 1AA1 1                    30.5000E+010.5000E+010.2000E+020.1000E+01
AA1 1AA1 2                    10.1000E+020.1000E+020.1000E+02
AA1 1AB1 1                    30.5000E+010.5000E+010.2000E+020.1000E+01
AB1 1AB1 2                    10.1000E+020.1000E+020.1000E+02
AB1 1AC1 1                    30.5000E+010.5000E+010.2000E+020.1000E+01
AC1 1AC1 2                    10.1000E+020.1000E+020.1000E+02
AC1 1AD1 1                    30.5000E+010.5000E+010.2000E+020.1000E+01
AD1 1AD1 2                    10.1000E+020.1000E+020.1000E+02
AD1 1AE1 1                    30.5000E+010.5000E+010.2000E+020.1000E+01
AE1 1AE1 2                    10.1000E+020.1000E+020.1000E+02
AE1 1AF1 1                    30.5000E+010.5000E+010.2000E+020.1000E+01
AF1 1AF1 2                    10.1000E+020.1000E+020.1000E+02
AF1 1AG1 1                    30.5000E+010.5000E+010.2000E+020.1000E+01
AG1 1AG1 2                    10.1000E+020.1000E+020.1000E+02
AG1 1AH1 1                    30.5000E+010.5000E+010.2000E+020.1000E+01
AH1 1AH1 2                    10.1000E+020.1000E+020.1000E+02
AH1 1AI1 1                    30.5000E+010.5000E+010.2000E+020.1000E+01
AI1 1AI1 2                    10.1000E+020.1000E+020.1000E+02
AI1 1AJ1 1                    30.5000E+010.5000E+010.2000E+020.1000E+01
AJ1 1AJ1 2                    10.1000E+020.1000E+020.1000E+02
AJ1 1AK1 1                    30.5000E+010.5000E+010.2000E+020.1000E+01
AK1 1AK1 2                    10.1000E+020.1000E+020.1000E+02
AK1 1AL1 1                    30.5000E+010.5000E+010.2000E+020.1000E+01
AL1 1AL1 2                    10.1000E+020.1000E+020.1000E+02
AL1 1AM1 1                    30.5000E+010.5000E+010.2000E+020.1000E+01
AM1 1AM1 2                    10.1000E+020.1000E+020.1000E+02
```

Figure C-2 (cont.): Sample of the mesh input used in base case models. The portion of the CONNE block shown describes connections between grid blocks in the first two columns and rows of the mesh.

Table C-1: Relative permeability and capillary pressure parameters selected for each unit, based on the Van Genuchten-Mualem method.

Relative Permeability and Capillary Pressure Parameters							
Unit code	λ	S_{lr} (k_{rel})	S_{ls}	S_{gr}	S_{lr} (P_{cap})	$1/P_0$	P_{max}
KLIME	0.63	0.17	1.00	0.05	0.15	1.00E-05	5.00E+07
CSAND	0.63	0.21	1.00	0.05	0.19	1.00E-05	5.00E+07
WATBL	0.63	0.21	1.00	0.05	0.19	1.00E-05	5.00E+07
AQUIF	0.63	0.21	1.00	0.05	0.19	1.00E-05	5.00E+07
UPSUP	0.63	0.21	1.00	0.05	0.19	1.00E-05	5.00E+07
SUPAI	0.63	0.21	1.00	0.05	0.19	1.00E-05	5.00E+07
FRACK	0.63	0.17	1.00	0.05	0.15	1.00E-05	5.00E+07
FRACC	0.63	0.21	1.00	0.05	0.19	1.00E-05	5.00E+07

Heat Flow Calculation

$q = -K(\Delta T/\Delta z)$
q = heat rate (J/s)
K = thermal conductivity…… 2.1 W/m K
$\Delta T = T_{rock} - T_{magma}$…….. 1000°C
$\Delta z = z_{rock} - z_{magma} = S_{TBL}$

$S_{TBL} = \sqrt{(\kappa\tau)}$
$\kappa = K/(\rho C_p)$
κ = thermal diffusivity (m^2/s)
ρ = density of sandstone…….. 2500 kg/m^3
C_p = heat capacity of wet sandstone……920 J/kg K
τ = time scale…….. 3600- 14400 s (1-4 hrs)**

1. $\kappa = K/(\rho C_p)$
   $= 2.1/(2500 \times 920)$
   $= 9.13 \times 10^{-7}\ m^2/s$

2. $S_{TBL} = \sqrt{(\kappa\tau)}$
   $= \sqrt{((9.13 \times 10^{-7})(3600))}$ *(2a)*
   $= 5.70 \times 10^{-2}$ m

   $= \sqrt{((9.13 \times 10^{-7})(14400))}$ *(2b)*
   $= 1.15 \times 10^{-1}$ m

3. $q = -K(\Delta T/\Delta z)$
   $= -2.1(-1000/(5.70 \times 10^{-2}))$ *(3a)*
   $= 3.66 \times 10^{4}$ J/s m^2

   $= -2.1(-1000/(1.15 \times 10^{-1}))$ *(3b)*
   $= 1.83 \times 10^{4}$ J/s m^2

4. Across whole 20 m^2 of interface (i):
   $q \times i = (3.66 \times 10^4) \times 20$ *(4a)*
   $= 7.33 \times 10^5$ J/s

   $= (1.83 \times 10^4) \times 20$ *(4b)*
   $= 3.66 \times 10^5$ J/s

Average heat rate = **5.50×10^5 J/s**

** Parameter was tested over a range of values; "final" or base-case heat rate is an average of these values.

Figure C-3: Heat rate calculations for heat generation from a modeled magma source. This rate is an approximation and is considered open to variation.

Table C-2: Schedules of heat injection with depth over time for the small models (left-hand side) and large models (right-hand side). After each injection start time, heat rate is continuous (5.50×10^5 J/s) for the duration of the simulation.

Rapid Heat Injection Schedule- Small Model			
Injection depth (grid block top, m)	Injection width (m)	Vertical distance of magma travel (m)	Injection start time (s)
95	20	10	660
105	20	10	640
115	20	10	620
125	20	10	600
135	20	10	580
145	20	10	560
155	20	10	540
165	20	10	520
175	20	10	500
185	20	10	480
195	20	10	460
205	20	10	440
215	20	10	420
225	20	10	400
235	20	10	380
245	20	10	360
255	20	10	340
265	20	10	320
275	20	10	300
285	20	10	280
295	20	10	260
305	20	10	240
315	20	10	220
325	20	10	200
335	20	10	180
345	60	10	160
355	100	10	140
365	140	10	120
375	180	10	100
385	220	10	80
395	260	10	60
405	300	10	40
415	380	10	0
425	380	5	0

Rapid Heat Injection Schedule- Large Model			
Injection depth (grid block top, m)	Injection width (m)	Vertical distance of magma travel (m)	Injection start time (s)
95	20	10	1140
105	20	10	1120
115	20	10	1100
125	20	10	1080
135	20	10	1060
145	20	10	1040
155	20	10	1020
165	20	10	1000
175	20	10	980
185	20	10	960
195	20	10	940
205	20	10	920
215	20	10	900
225	20	10	880
235	20	10	860
245	20	10	840
255	20	10	820
265	20	10	800
275	20	10	780
285	20	10	760
295	20	10	740
305	20	10	720
315	20	10	700
325	20	10	680
335	20	10	660
345	60	10	640
355	100	10	620
365	140	10	600
375	180	10	580
385	220	10	560
395	260	10	540
405	300	10	520
415	340	10	500
425	380	10	480
440	380	15	450
455	420	15	420
470	420	15	390
485	420	15	360
500	460	15	330
515	460	15	300
530	460	15	270
545	500	15	240
560	500	15	210
575	540	15	180
590	540	15	150
605	580	15	120
620	580	15	90
635	580	15	60
650	620	15	30
665	620	15	0
680	620	15	0
695	620	15	0
710	620	7.5	0

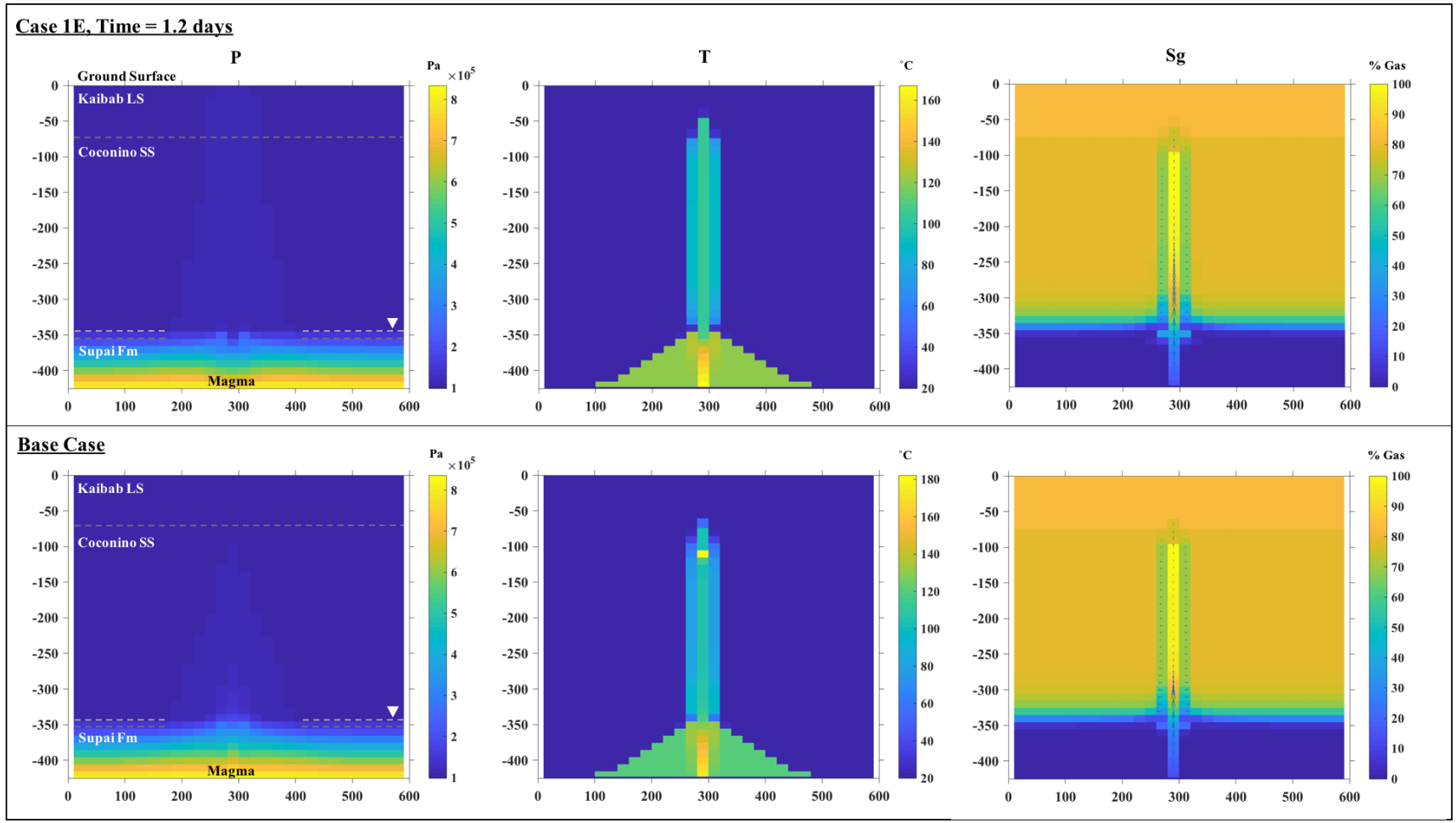

Figure C-4: Pressure, temperature, and gas saturation at ~1.2 days for a simulation of rapid heat injection into a model with a fracture zone of increased permeability and porosity (Case 1E). Base case shown at bottom at the same time step. Largest gas flow rate vector in fracture zone: $V_Z = 0.11$ kg/s, $V_X = 3.40 \times 10^{-5}$ kg/s (Case 1E).

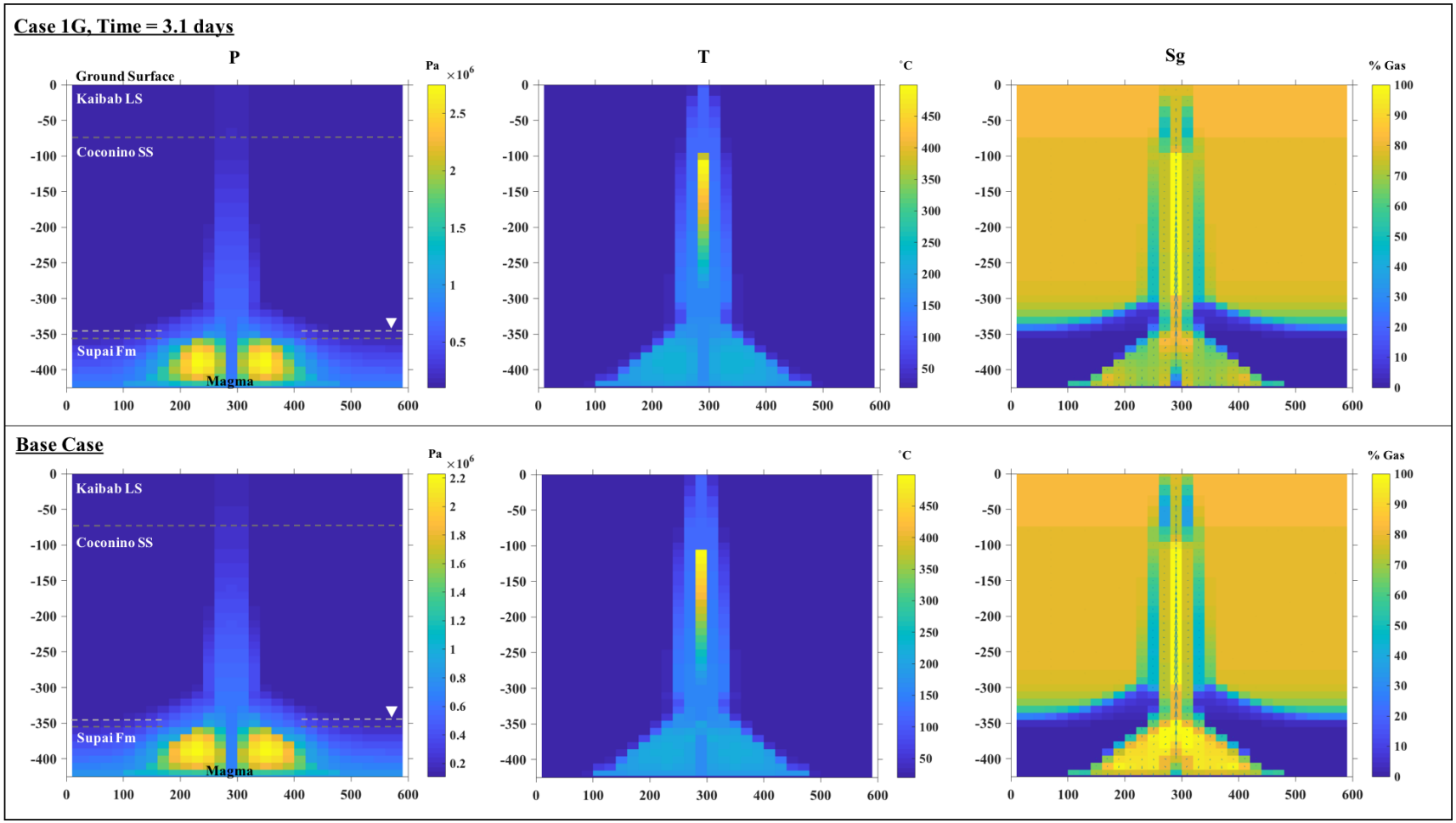

Figure C-5: Pressure, temperature, and gas saturation at ~3.1 days for a simulation of rapid heat injection into a model with high-porosity country rock (Case 1G). Base case shown at bottom at the same time step. Largest gas flow rate vector in fracture zone: $V_Z = 0.37$ kg/s, $V_X = 1.50 \times 10^{-5}$ kg/s (Case 1G).

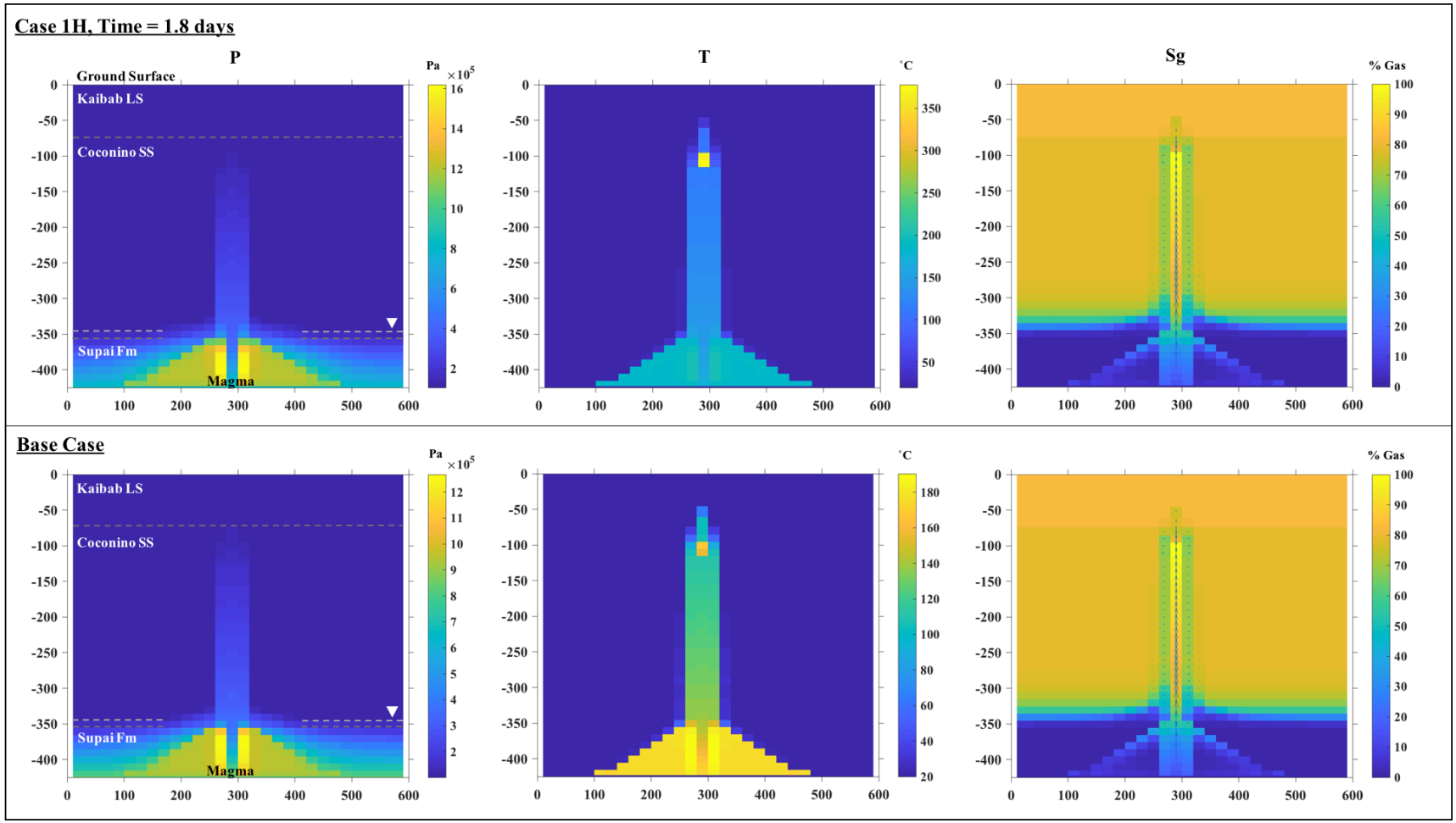

Figure C-6: Pressure, temperature, and gas saturation at ~1.8 days for a simulation of rapid heat injection into a model with low-porosity country rock (Case 1H). Base case shown at bottom at the same time step. Largest gas flow rate vector in fracture zone: $V_Z = 0.17$ kg/s, $V_X = 1.00 \times 10^{-6}$ kg/s (Case 1H).

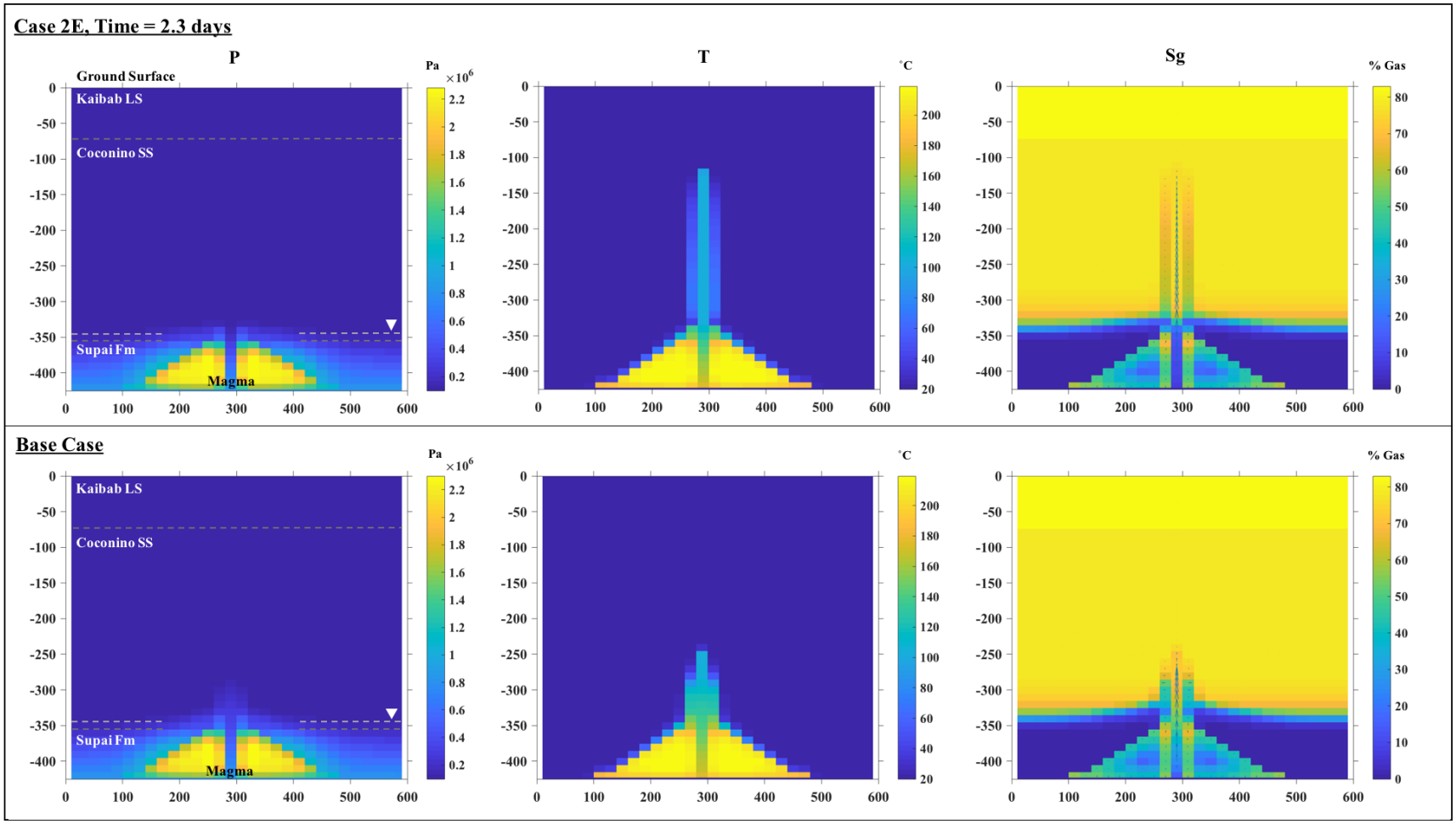

Figure C-7: Pressure, temperature, and gas saturation at ~2.3 days for a simulation of slow heat injection into a model with a fracture zone of increased porosity and permeability (Case 2E). Base case shown at bottom at the same time step. Largest gas flow rate vector in fracture zone: $V_Z = 0.23$ kg/s, $V_X = 1.40 \times 10^{-9}$ kg/s (Case 2E).

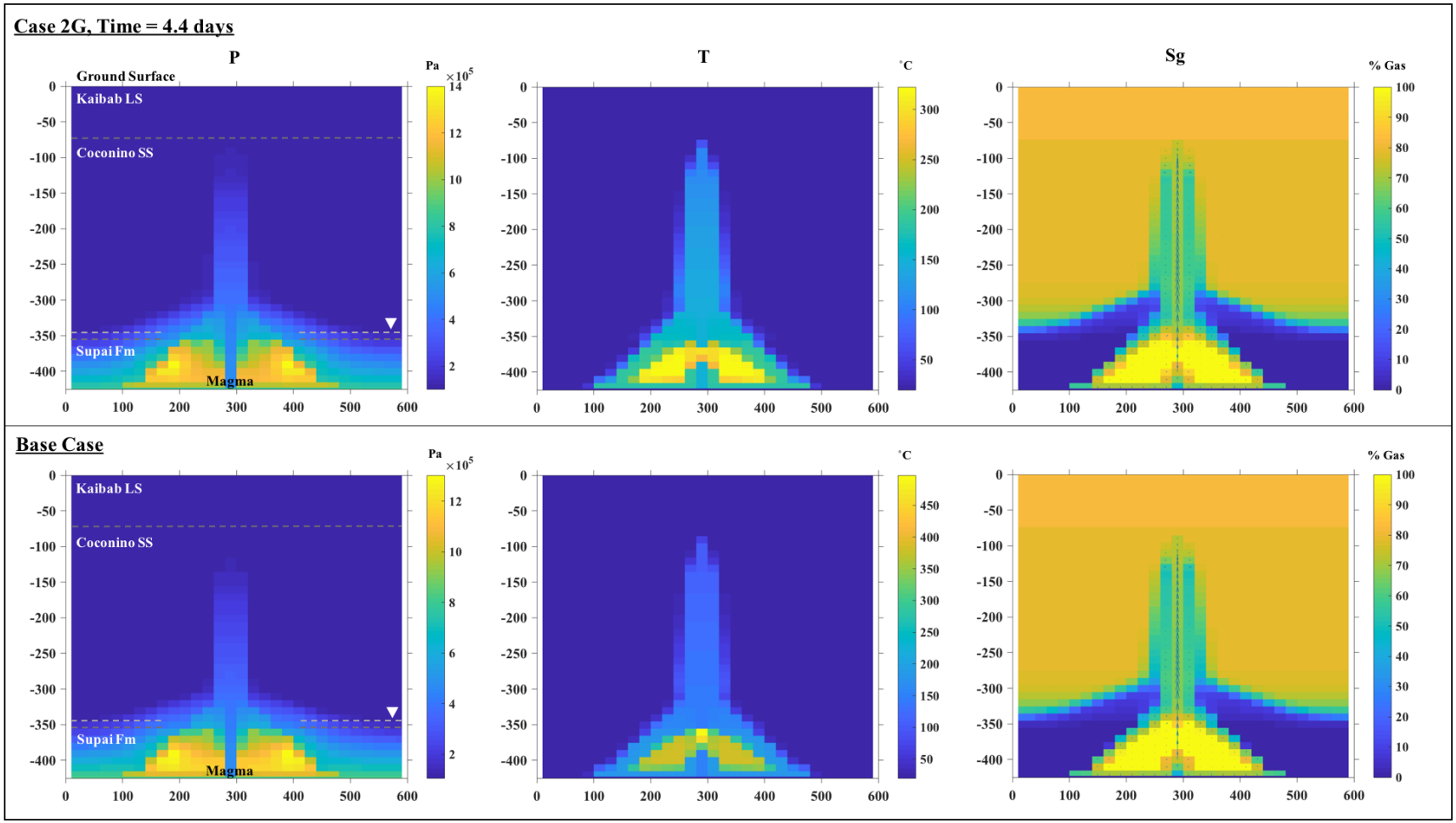

Figure C-8: Pressure, temperature, and gas saturation at ~4.4 days for a simulation of slow heat injection into a model with high-porosity country rock (Case 2G). Base case shown at bottom at the same time step. Largest gas flow rate vector in fracture zone: $V_Z = 0.17$ kg/s, $V_X = 3.65 \times 10^{-7}$ kg/s.

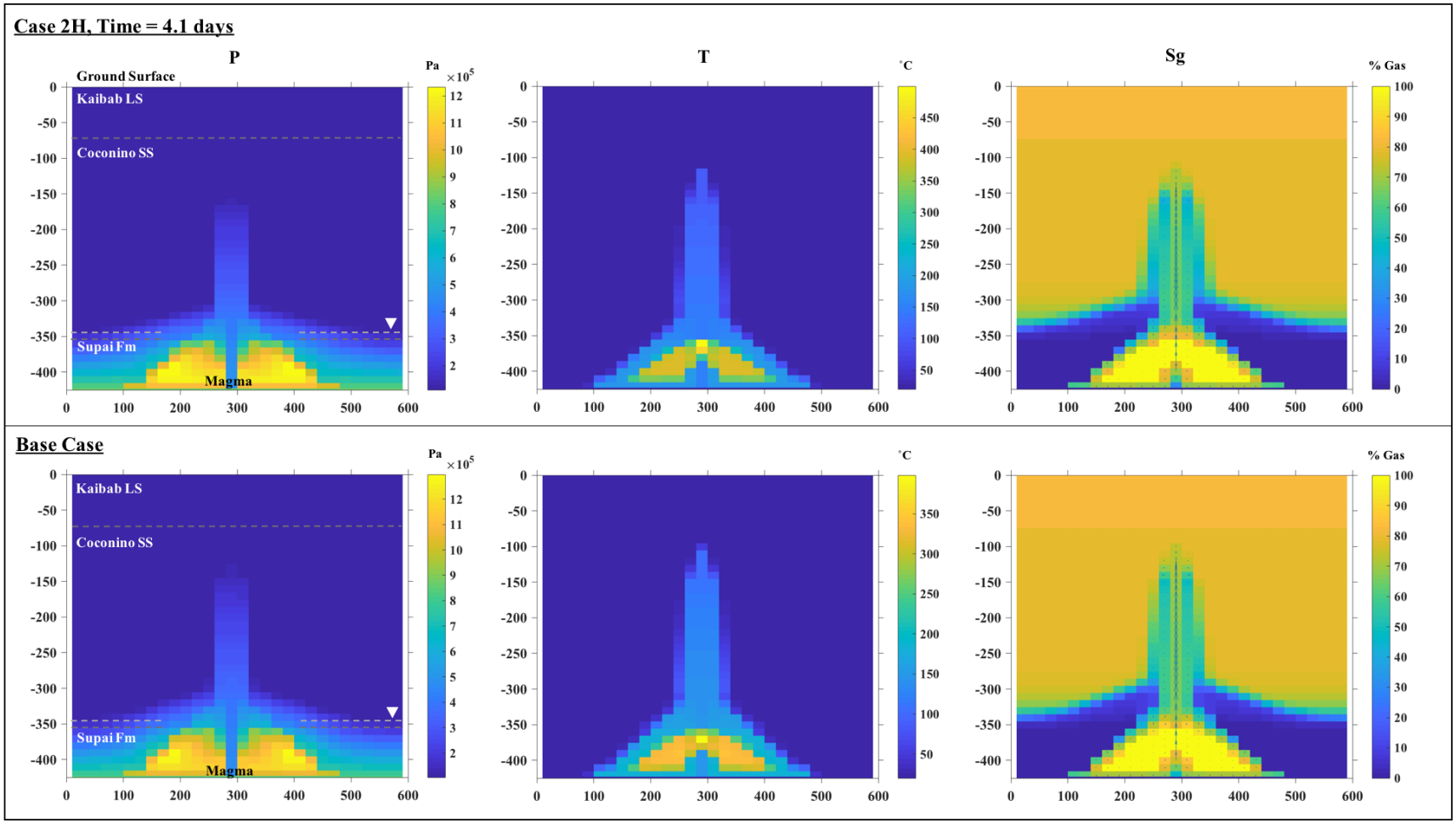

Figure C-9: Pressure, temperature, and gas saturation at ~4.1 days for a simulation of slow heat injection into a model with low-porosity country rock (Case 2H). Base case shown at bottom at the same time step. Largest gas flow rate vector in fracture zone: $V_Z = 0.15$ kg/s, $V_X = 1.85 \times 10^{-7}$ kg/s (Case 2H).

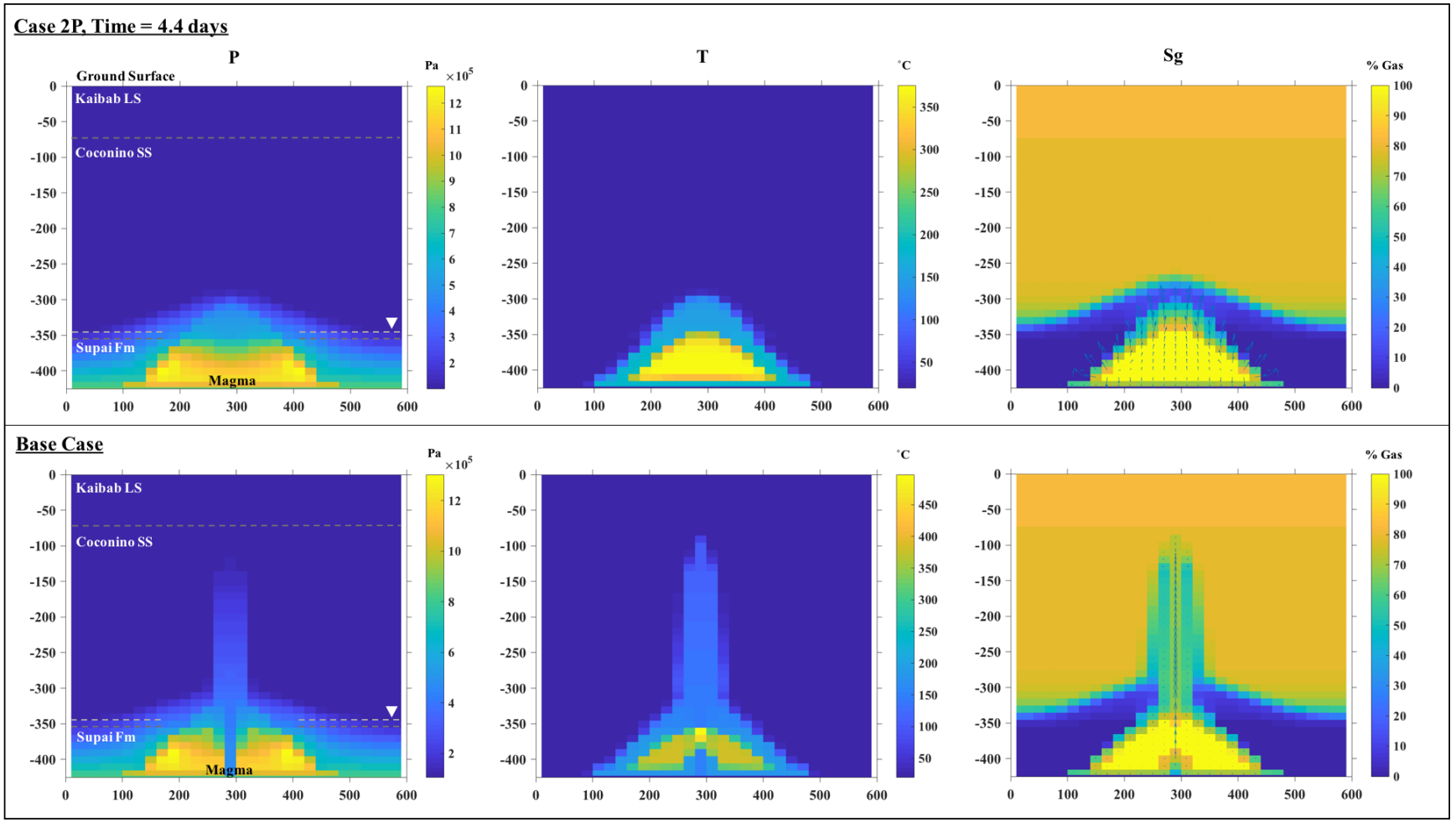

Figure C-10: Pressure, temperature, and gas saturation at ~4.4 days for a simulation of slow heat injection into a model with no fracture zone (Case 2P). Base case with a 20-m-wide fracture zone shown at bottom at the same time step. Largest gas flow rate vector in fracture zone: $V_Z = 7.28 \times 10^{-3}$ kg/s, $V_X = -3.92 \times 10^{-3}$ kg/s (Case 2P).